Calculation of Heat Flux from the Region Behind a Reflected Shock Wave into the Shock Tube Edge

S. V. Bulovich*, V. É. Vikolaĭnen, and R. L. Petrov

St. Petersburg State Technical University, St. Petersburg, 195251 Russia
* e-mail: bsv@stu.neva.ru
Received April 28, 2004

Abstract—We have numerically calculated the process of conjugated unsteady heat exchange during the formation of a boundary transient temperature layer as a result of the interaction of a shock wave with a flat edge surface of a shock tube. The results of calculations can be used in the analysis of the experimental data. The time variation of the heat flux and the temperature at the gas–solid interface is determined. The heat flux distribution profiles are obtained for two limiting variants of the boundary conditions on the outer surface of the shock tube. © 2004 MAIK "Nauka/Interperiodica".

Introduction. The known automodel solution [1] of the problem of shock wave refection from a flat edge surface of the shock tube is strictly valid only in the case of a thermally insulated wall. Allowance for the thermal conductivity of the wall material leads to the appearance of a boundary transient temperature layer both in the gas at the edge surface of the shock tube and in the wall material. This situation poses the problem of conjugated unsteady heat exchange, whereby the so-called boundary conditions of type IV [2] have to be satisfied at any time at the gas–surface interface.

In this study, we have obtained a solution to the problem of conjugated heat exchange for the time $t > t^* = 2\Delta/U$, where t^* is the characteristic time of interaction between the shock wave and the surface, Δ is the shock wave front width, and U is the absolute velocity of the shock wave propagation.

During the time t^*, the gas temperature near the wall increases from the initial value, corresponding to the state before the interaction between the shock wave and the surface, to a temperature behind the reflected shock wave. It should be noted that thermal equilibrium between the gas and the solid is violated beginning from the moment when the incident shock wave front reaches the wall surface, and the boundary temperature layer formation also starts at this moment. A comparison of the time of relaxation of the gasdynamic functions in the boundary layer to the time of interaction between the shock wave and the surface shows that these processes are characterized by different time scales. For this reason, we may assume that the gas temperature at the gas–solid interface exhibits a jumplike change and that the period of time t^* can be disregarded in the analysis of formation of the boundary temperature layer.

Formulation of the problem. Let us assume that the gas pressure near the solid wall varies insignificantly. Then, the state of gasdynamic functions in the boundary temperature layer can be described using the equations of balance of the mass and energy and the equation of state.

The system of equations describing the behavior of the gasdynamic functions in the boundary temperature can be written as

$$\frac{\partial \rho_g}{\partial t} + \frac{\partial (\rho_g u_g)}{\partial x} = 0,$$

$$\rho_g c_g \frac{\partial T_g}{\partial t} + \rho_g c_g u_g \frac{\partial T_g}{\partial x} - \frac{\partial}{\partial x}\left(\lambda_g \frac{\partial T_g}{\partial x}\right) = 0, \qquad (1)$$

$$\rho_g = \frac{p_g}{RT_g}, \quad \lambda_g = \lambda_g(T_g), \quad c_g = c_g(T_g), \quad p_g = \text{const},$$

where t is the time; x is the coordinate along the normal to the surface; ρ_g, u_g, T_g, p_g, c_g, and λ_g are the gas density, velocity, temperature, pressure, heat capacity, and thermal conductivity, respectively; and R is the gas constant.

The energy balance equation for the solid is as follows:

$$\frac{\partial}{\partial t}(\rho_s c_s T_s) - \frac{\partial}{\partial x}\left(\lambda_s \frac{\partial T_s}{\partial x}\right) = 0, \qquad (2)$$

$$c_s = c_s(T_s), \quad \lambda_s = \lambda_s(T_s), \quad \rho_s = \text{const},$$

where ρ_s, T_s, c_s, and λ_s are the solid material density, temperature, heat capacity, and thermal diffusivity, respectively.
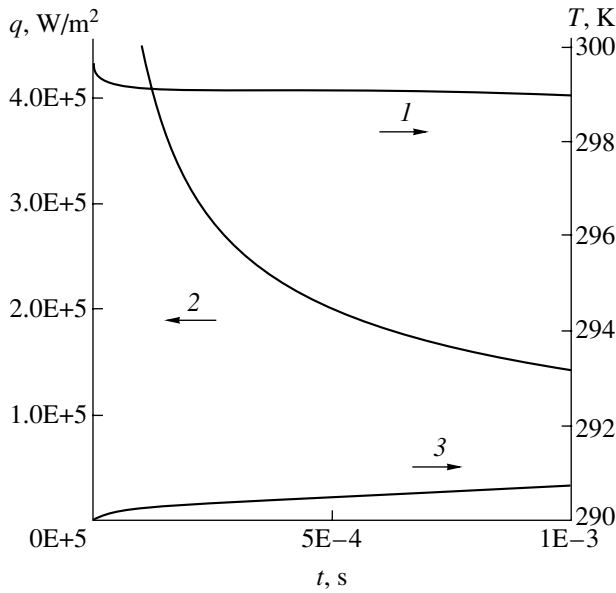
Fig. 1. Time variation of (*1*) the temperature and (*2*) the heat flux at the conjugated boundary and (*3*) the average temperature of bismuth.

Boundary conditions. At the outer surface of the boundary layer, the temperature corresponds to the initial state of the gas behind the reflected shock wave, which represents a boundary condition of type I. The thermal state on a nonconjugated boundary of the solid can be formally written in a form reflecting the structure of the boundary condition of type III:

$$\alpha T + \beta \frac{\partial T}{\partial x} = \gamma. \qquad (3)$$

By selecting the proper coefficients, it is possible to provide for the required boundary condition for the temperature, heat flux, or their combination. On a conjugated boundary, we set the temperature so as to provide the coincidence of heat fluxes in the gas and in the solid and, in addition, we set a homogeneous boundary condition for the gas velocity.

Initial condition. The values of the gasdynamic functions correspond to the state behind the reflected shock wave. The temperature in the solid coincides with that of the gas before arrival of the shock wave. The temperature of the wall surface provides for the coincidence of heat fluxes in the gas and in the solid.

Method of solution. The problem was solved by numerical methods. Discretization of the calculation region was performed by the method of control volumes. The values of the functions were determined at the centers of cells, and the values of convective and heat fluxes, at the boundaries of the control cells. The system of equations was integrated with respect to time using a two-layer scheme of the Krunk–Nicholson type. Complete matching of the values of functions in the upper temporal layer was achieved by means of
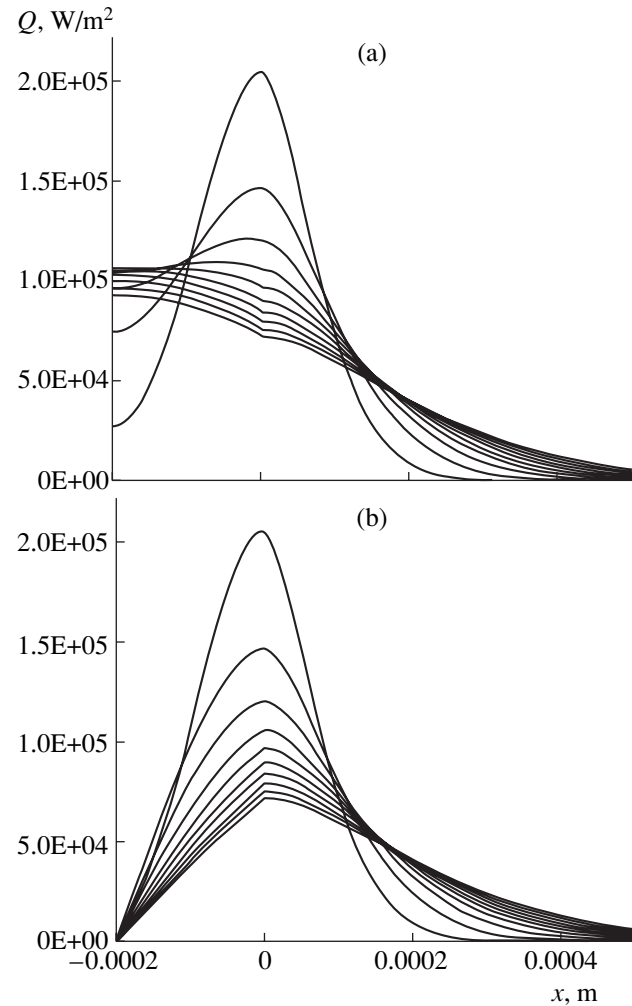

Fig. 2. Heat flux profiles and their evolution with time at the gas–solid interface for a bismuth layer on (a) copper substrate (variant 1) and (b) organic glass substrate (variant 2).

simple iterations, which allowed the values of temperature-dependent functions and the surface temperature to be refined. Thus, the energy balance equation for the gas and solid were solved under boundary conditions of type I, and the surface temperature was determined from the condition of equal heat fluxes and refined by iterations.

Results and discussion. Unsteady conjugated heat exchange in the system under consideration was calculated in two variants with different boundary conditions. The shock tube edges were comprised of two layers. The inner layer, with a thickness of 2.0×10^{-4} m, was made of bismuth ($c_s = 125$ J/(kg K), $\lambda_s = 9$ W/(m K), $\rho_s = 9800$ kg/m^3). The outer layer was made either of copper (variant 1: $c_s = 396$ J/(kg K), $\lambda_s = 389$ W/(m K), $\rho_s = 8930$ kg/m^3) or of an organic glass (variant 2: $c_s = 1425$ J/(kg K), $\lambda_s = 0.184$ W/(m K), $\rho_s = 1180$ kg/m^3). A comparison of the thermal diffusivities of copper or organic glass to that of bismuth shows that it is possible

to restrict calculations of the heat transfer to the bismuth layer with the boundary conditions of type I (for variant 1) and type II (variant 2). The initial temperature of the surface was $T_s = 290$ K, and the gas layer thickness was 5.0×10^{-4} m. Calculations were performed for air with the following parameters behind the reflected shock wave: $p_g = 1.5$ MPa, $T_g = 725$ K (for the initial atmospheric pressure, this corresponds to the Mach number of the incident shock wave $M_1 = 2$). The spatial discretization step was 1.0×10^{-6} m, and the temporal integration step was 1.0×10^{-7} s; the process was followed over a period of time up to 1.0×10^{-3} s.

Figure 1 shows the time variation of the temperature (curve *1*) and heat flux (curve *2*) on the surface of bismuth (curve *3* shows the average temperature of bismuth in the variant with thermoinsulated substrate). Figure 2 presents the heat flux profiles and shows their evolution with time for the two variants studied. The profiles were calculated with a time interval of 5.0×10^{-4} s.

A comparative analysis of the results of calculations for the two variants leads to the following conclusions. In the initial stage, when the bismuth layer is not heated throughout, the character of heat transfer in both variants is virtually identical (despite visible differences in the values of heat flux at the bismuth–substrate interface). The characteristic period of time during which the temperatures and heat fluxes on the conjugated boundary in the two variants are practically the same in the case under consideration is about 1.0×10^{-3} s (this value depends on the bismuth layer thickness).

Subsequent development of the process of heat transfer reflects the fact that the heat flux intensity through the gas–solid interface decreases as a result of an increase in the thickness of a boundary temperature layer in the gas. This phenomenon, whereby the boundary layer thickness increases in proportion to the square root of time, determines the character of all processes both in the gas and in the solid wall. The influence of the type of boundary conditions for the solid is manifested on a greater time scale. This influence consists in that the level of temperatures in the bismuth layer in variant 1 is determined by the boundary conditions of type I, while in variant 2 the temperature of bismuth may increase up to that of the gas. In the latter case, the wall influences the gas. Indeed, as the average temperature of the material increases, the heat flux through the gas–solid interface decreases at a higher rate than in variant I, and the solution (i.e., the state of the gas) asymptotically approaches that corresponding to the adiabatic wall.

REFERENCES

1. L. V. Ovsyannikov, *Lectures on Basic Gas Dynamics* (Nauka, Moscow, 1981) [in Russian].
2. A. V. Lykov, *Theory of Thermal Conduction* (Gostekhizdat, Moscow, 1952) [in Russian].

Translated by P. Pozdeev

The Kinetics of Variation of the Reflectance
of Nanostructured Aluminum Alloys under Laser Irradiation

P. Yu. Kikin, A. I. Pchelintsev, and E. E. Rusin*

Blagonravov Institute of Engineering Science (Nizhni Novgorod Branch), Russian Academy of Sciences,
Nizhni Novgorod, Russia
* e-mail: rusin@mech.unn.runnet.ru
Received May 12, 2004

Abstract—The reflectance of nanostructured aluminum alloys under the action of laser radiation at a nondestructive intensity level significantly decreases and exhibits a nonlinear character. © 2004 MAIK "Nauka/Interperiodica".

Nanostructured materials—in particular, aluminum-based alloys—obtained by methods of intense plastic deformation [1], are known to possess unique mechanical properties. Their main advantageous property is a high plasticity under certain conditions of straining. Articles made of such materials have good prospects in various commercial fields [1, 2].

Until now, no systematic investigations have been devoted to the use of laser technologies for the thermal and dimensional processing of nanostructured materials. However, there is a need for detailed study of the processes taking place both on the surface and in the heat-affected zone during laser action on such materials occurring in substantially nonequilibrium states.

In this context, we have studied a change in the reflectance of a nanostructured material under the action of a single low-intensity laser pulse. The material was a medium-strength aluminum–lithium alloy (grade 1420) with the following chemical composition (%): Li, 1.8–2.3; Mg, 4.5–6.0; Zn, 0.08–0.15 (Al to balance). The experiments were performed with a YAG:Nd^{3+} laser operating at a wavelength of $\lambda = 1.06$ μm and generating pulses with a duration of 5 ms and an intensity of 2×10^5 W/cm^2. These parameters of laser pulses ensured nondestructive action on the surface of polished samples.

Figure 1 shows oscillograms of the incident laser pulse and the reflected signal. In the first stage of interaction (~1.2 ms), the shapes of the incident and reflected pulses virtually coincide. In the second stage, the amplitude of the reflected signal significantly decreases, which is probably related to a change in the structure and composition of a thin surface layer of the material.

In order to explain the observed effects, we have performed metallographic investigation of the target material in the zone of laser action. A micrograph in Fig. 2 shows the structures of the laser-heated zone and the initial material. As can be seen, the subsurface layer in the laser-heated zone (top part of the micrograph) exhibits a change in the homogeneous microstructure as compared to that in the deeper layers (bottom part of the micrograph). In the laser-heated zone, the grain size is 5–10 μm, whereas that in the initial structure of the material subjected to intense plastic straining is 0.5–2 μm. The latter small grains are partly aggregated into coarse inclusions (up to 10 μm in size), with impurity phases concentrated on their boundaries [1] (manifested by dark spots in Fig. 2).

Thus, the laser pulse action even at a moderate intensity on a given nanostructured material leads to significant changes in the microstructure and morphology of the surface layer, which influence the reflectance of the sample surface. We believe that these changes are related to the energy stored in the course of the intense plastic straining and to considerably enhanced grain-boundary diffusion (as pointed out, e.g., in [1, 2]). We also believe that another important factor is the pres-
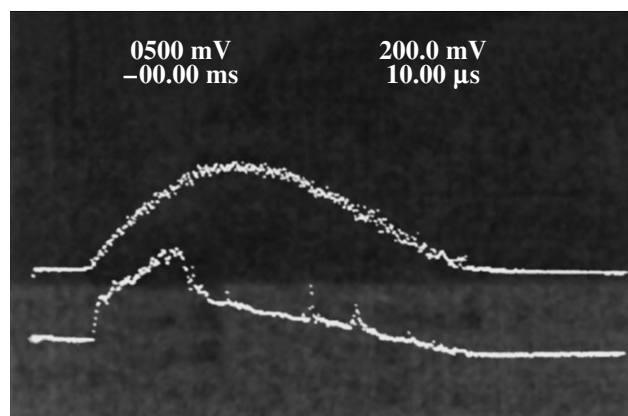

Fig. 1. Oscillograms of the incident laser pulse (upper curve) and the reflected signal (lower curve), showing the stages of operation in the (I) free lasing and (II) modulated *Q* modes.
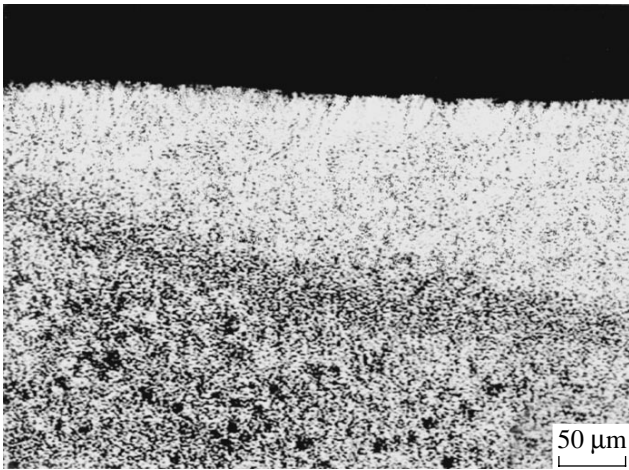
Fig. 2. A micrograph showing the heat-affected subsurface zone formed under the action of a single laser pulse.

ence of elements with a relatively low melting point and a high chemical activity. In the case under consideration, these are lithium, magnesium, and their compounds.

REFERENCES

1. R. Z. Valiev, I. V. Alexandrov, and R. K. Islamgaliev, in *Processing and Properties of Nanostructured Materials Prepared by Severe Plastic Deformation in Nanostructured Materials: Science and Technology*, Ed. by G. M. Chow and N. I. Noskova (Kluwer, Dordrecht, 1998).

2. *Grain-Boundary Diffusion and Properties of Nanostructured Materials*, Ed. by Yu. R. Kolobov and R. Z. Valiev (Nauka, Novosibirsk, 2001) [in Russian].

Translated by P. Pozdeev

Pulsed Pressing of Powdered Materials Studied Using the Kolsky Method

A. M. Bragov*, S. N. Rodionov, and E. E. Rusin

Research Institute of Mechanics, Nizhni Novgorod State University,
Nizhni Novgorod, Russia
* e-mail: bragov@mech.unn.ru
Received May 13, 2004

Abstract—A modification of the Kolsky method for high-rate pulsed compaction of powdered materials is proposed, which allows the loading parameters to be controlled and the rational processing regimes to be selected. Using the proposed method, high-quality homogeneous products have been obtained by loading powders at a pulse duration of 100–400 μs and an amplitude of up to 1500 MPa. © *2004 MAIK "Nauka/Interperiodica".*

A special position among various methods used for the compaction of powdered materials belongs to high-rate pulsed pressing [1, 2]. This process is characterized by high straining rates (reaching 10^2–10^4 s^{-1}), short loading times (on the order of milli- and microseconds), and high pressures. The interest in this method of compaction is related to the fact that the regime of pulsed compression is preferred for the pressing of low-plasticity and hardly deformable powders and composites.

The main factor hindering the development of high-rate pressing methods is insufficient knowledge of the complex physicochemical processes involved in various stages of such compaction. This is explained by difficulties in the measurement and determination of the parameters of loading and state of a powdered material in the course of pressing. In order to solve these problems, we suggest studying the process of pulsed compaction of powdered materials using the Kolsky method [3], which allows the process of high-rate compaction to be studied under controlled conditions.

In the proposed scheme (Fig. 1), the sample of a powdered material in a rigid container of small length L_0 is placed between two hard rods of equal diameters. The rods are made of a material with rather high elastic limit (on a level of 2000 MPa). The compression pulse is generated by the impact of striker *1* on the edge of rod *2*. The one-dimensional elastic wave of compression formed at a certain distance from the edge propagates along the rod at the velocity *C*. By measuring the elastic strain in both rods, it is possible to determine the stress and strain in the powder material.

According to the one-dimensional theory of elastic wave propagation, the average strain and stress in the sample are determined from the strain pulses measured

in rods *2* and *3* using the Kolsky relations [3],

$$\varepsilon = -\frac{2C}{L_0}\int_0^t \varepsilon_R dt, \qquad (1)$$

$$\sigma = EF\varepsilon_T/F_s, \qquad (2)$$

where ε_R and ε_T are the strain pulses reflected from and transmitted through the sample, respectively; F_s is the sample cross-section area; L_0 is the initial sample length; F is the cross-section area of the rods; C is the sound velocity in the rods; E is the Young modulus of the rod material; and t is the time.

Using relations (1) and (2) and the measured strains ε_R and ε_T, one can calculate the stress σ and strain ε in the sample as a function of time and construct the dynamic stress–strain diagram of compaction for the material studied. In addition, by measuring the pulses of tangential and radial strains, it is possible to determine the time variation of the pressure $P(t)$, the shear resistance $\tau(t)$, and the lateral thrust coefficient [4].

We have studied the pulsed compaction of powdered materials using an experimental setup according to the scheme in Fig. 1, comprising a loading device, two rods
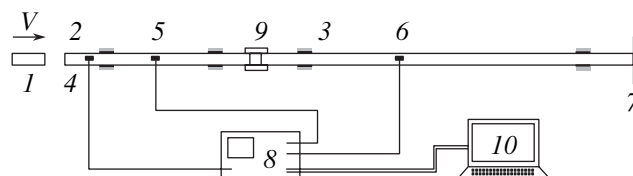

Fig. 1. Schematic diagram of the experimental setup for studying the process of pulsed compaction of powdered materials: (*1*) striker; (*2, 3*) rods; (*4*) start transducer; (*5, 6*) strain gauges; (*7*) shock absorber; (*8*) S9-8 digital oscillograph; (*9*) container with a sample powder; (*10*) computer.

(each with a diameter of 20 mm), and a set of measuring and synchronizing equipment [5, 6]. The loading device was a 20-mm-bore gas gun. A special container *9* with the sample powder was placed between the edges of the rods.

The experiments were performed with a powder of reduced iron with an average grain size of 15 μm. The process parameters were as follows: pressing pressure, up to 1300 MPa; pressing pulse duration, 100–300 μs. At a fixed pressure pulse amplitude, the maximum density of compacted material was observed for a pulse duration of 300 μs.

In order to increase the level of sample straining, we used a modification of the Kolsky method described previously [7]. According to this variant, the rods are chosen with a length ratio of 1:2, which allows two cycles of loading by pulses of the same sign (compression) to be applied to the sample in each experiment. Such a modified scheme provides for a higher density of compacted material.

Figure 2 shows the typical diagram of pulsed compaction of a sample of reduced iron powder. In the regime of pulsed compaction without plasticizer, the density of samples relative to iron was 88% after pressing and increased to 92% after sintering, so that the absolute value reached 7874 kgf/m^3. Metallographic investigations showed that the compacted material possesses a rather homogeneous fine-grained structure in both the longitudinal and transverse directions. The grain size was 1–5 μm.

The results of experiments with hardly deformable powders confirmed the good prospects for the use of the proposed method. For example, the relative density of compacts obtained from a powdered mixture comprising synthetic diamond, iron, nickel, and copper reached 95%.

In conclusion, we have proposed an original modification of the Kolsky method, which makes it possible to perform pulsed compaction of powders under controlled loading conditions, to select optimum 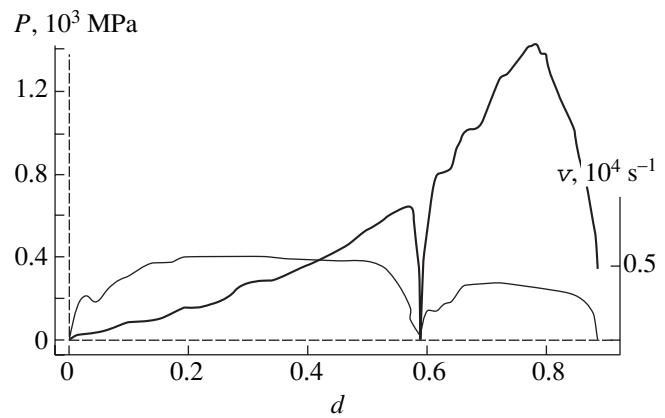pressing regimes, and to obtain high-quality homogeneous compacts by loading powders at a pulse duration of 100–400 μs and an amplitude of up to 1500 MPa.

Fig. 2. Typical diagrams of the pressure P and the straining rate v versus strain d for the process of pulsed compaction of a powder of reduced iron.

REFERENCES

1. K. N. Bogoyavlenskiĭ, P. A. Kuznetsov, K. K. Mertens, *et al.*, *High-Speed Methods of Pressing Powder Materials* (Mashinostroenie, Leningrad, 1984) [in Russian].

2. A. A. Deribas, P. A. Simonov, V. N. Filimonenko, *et al.*, Fiz. Goreniya Vzryva, No. 6, 45 (2000).

3. H. Kolsky, *Stress Waves in Solids* (Clarendon, Oxford 1953).

4. A. M. Bragov, G. Grushevsky, and A. K. Lomunov, DYMAT J. **1**, 253 (1994).

5. A. M. Bragov, A. K. Lomunov, and E. E. Rusin, in *Applied Problems of Strength and Plasticity. Statics and Dynamics of Strained Systems: All-Union Inter-Institute Collection of Scientific Works* (Gorky State Univ., Gorky, 1980), Vol. 16, pp. 138–144.

6. A. M. Bragov and A. K. Lomunov, Int. J. Impact Eng. **16**, 321 (1995).

7. A. M. Bragov, A. K. Lomunov, and I. V. Sergeichev, Prikl. Mekh. Tekh. Fiz. **42** (6), 199 (2001).

Translated by P. Pozdeev

Dimensional Features of the Luminescence of Europium(III) Chloride Nanoparticles in a Porous Glass Matrix

A. A. Petushkov, S. M. Shilov, and V. N. Pak*

Herzen State Pedagogical University, St. Petersburg, Russia
* e-mail: pak@vp7609.spb.edu
Received May 18, 2004

Abstract—Europium(III) chloride particles have been encapsulated in a porous glass by impregnating it with an aqueous salt solution followed by the removal of water from the pore space. The results of a comparative analysis of the luminescence spectra of the obtained samples to the spectra of massive salt and the observed concentration dependence of the emission parameters and the character of luminescence quenching in the course of water vapor adsorption agree with the notions about the nanodimensional state of salt particles in the matrix. © 2004 MAIK "Nauka/Interperiodica".

Porous glasses, in which the pore radius can be reliably controlled in the range $r = 2$–100 nm [1, 2], can be used as matrices for the synthesis and stabilization of nanoparticles of a large number of compounds [2–5]. The optical transparency of porous glasses in a broad range of wavelengths makes especially interesting the particle-size-dependent optical properties of the obtained nanocomposites. A simple and convenient means of deep fragmentation and stabilization of the cluster forms of various salts and complex compounds on the surface of silica gel is offered by a method based on impregnation of a porous glass with solutions of a given active component with variable concentration followed by removal of the solvent [4, 5].

In this study, the possibilities of this approach are demonstrated by the encapsulation of europium(III) chloride nanoparticles in a porous glass carrier and the investigation of the dimensional features in the luminescence of such composites.

The carrier was a fine disperse glass with a particle size of 0.05–0.07 mm, a predominant pore size of 4.5 nm, and a specific surface of $S = 80$ m^2/g. The porous glass was modified by impregnation for one day in an aqueous salt solution with a variable concentration within 0.01–1.0 mol/l, followed by dehydration through heating at 120°C. The content of europium(III) in the porous glass matrix was determined by dissolution in boiling water with subsequent photocolorimetric analysis in the form of an arsenazo complex [6]. The amount of adsorbed water was controlled in the range of relative vapor pressures $p/p_0 = 0.1$–0.95 using desiccators with sulfuric acid solutions. The luminescence spectra were measured using powdered samples (dry or containing adsorbed water) in hermetically sealed quartz tubes with a diameter of 5 mm. The emission

spectra in the visible spectral range and the lifetime of the excited state were measured at room temperature using a setup based on a universal computer-controlled spectral complex (KSVU-1) with a photomultiplier detector (FEU-100) [7]. The excitation source was a pulsed nitrogen laser (LGI-21) operating at a wavelength of $\lambda = 337$ nm and a pulse duration of $\tau = 10$ ns. The emission was measured at an angle of 90° relative to the laser beam direction.

Figure 1 shows the luminescence spectra of the samples of europium(III) chloride in a porous glass matrix (EuCl$_3$/PG) with various concentrations of encapsulated salt, $Q = 1.5$–150 μmol/g, upon drying at 120°C. In all cases, the dominating band in the spectrum is that
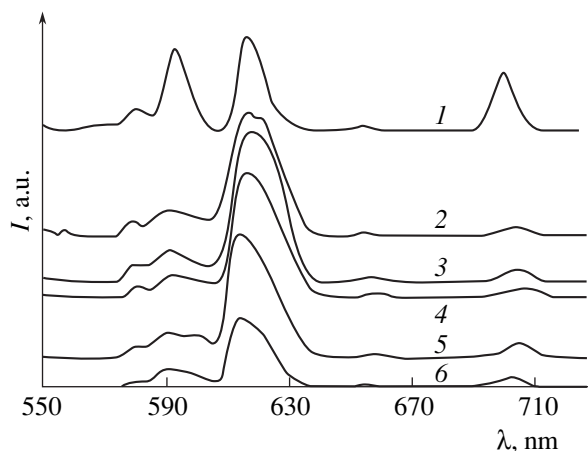

Fig. 1. The luminescence spectra of (*1*) polycrystalline europium chloride and (*2–6*) EuCl$_3$/PG with various concentrations of encapsulated salt $Q = 1.5$, 15, 60, 120, and 150 μmol/g, respectively.

corresponding to the hypersensitive $^5D_0 \longrightarrow {}^7F_2$ transition (λ_{max} = 613–618 nm) of trivalent europium. The other transitions, $^5D_0 \longrightarrow {}^7F_{0.1.3.4}$, are manifested by four weak bands with the maxima at 578, 590, 650, and 700 nm, respectively. Figure 1 also shows a characteristic difference between the optical emission spectra of the europium salt in the encapsulated and massive forms. In the latter case, the intensity of the band due to the hypersensitive ($^5D_0 \longrightarrow {}^7F_2$) transition is close to that of the magnetic dipole transition ($^5D_0 \longrightarrow {}^7F_1$), which is characteristic (according to the commonly accepted notions [8, 9]) of a relatively high symmetry of the coordination environment of Eu^{3+} cation. In the spectra of intercalated salt, the ratio of intensities of these bands changes sharply in favor of the hypersensitive transition; this is accompanied by the characteristic broadening of the band toward longer wavelengths, which also reflects a decrease in symmetry of the surrounding of Eu^{3+} cation [8–10].

Thus, we have established that small salt particles acquire, under the action of the carrier surface, specific optical properties different from those of the polycrystalline analog (precursor). The dimensional features also account for the increased brightness of the emission from nanoparticles encapsulated in the porous glass. Indeed, even a very small content of the optically active intercalate (Q = 1.5 μmol/g or ~0.02 mass %) provides for a significantly higher luminescence intensity as compared to that from the polycrystalline salt (Fig. 1). The nanodimensional state of the salt in the porous glass matrix was even more clearly manifested in the results of measurements of the lifetime of the excited $^5D_0$ state: the obtained value reaches τ^* = 230 μs, which is much greater than the value (80–90 μs) observed in massive europium chloride.

The character of growth and distribution of the salt articles on the surface of through pores in the glass matrix can be judged by changes in the integral intensity I of the emission band due to the $^5D_0 \longrightarrow {}^7F_2$ transition and in the lifetime of the excited state in the series of $EuCl_3$/PG samples with variable salt content (Fig. 2). As can be seen in Fig. 2, an increase in the content of intercalate (Q) is accompanied by the growth in intensity I and by a considerable increase in the lifetime τ^*. Both values reach maxima at Q = 30 μmol/g and then exhibit a decrease. Apparently, the narrow initial ascending regions in the curves reflect an increase in the number of homogeneously distributed isolated emission centers. This is accompanied by the increasing trend of aggregation and, at $Q > 30$ μmol/g, the concentration quenching of luminescence begins to prevail.

Using the known value of the specific surface of the carrier (S = 80 m^2/g) and the relation $n = QN_A/S$ (where N_A is the Avogadro number), it is possible to estimate the "topographic" density n of the intercalate distributed on the silica gel surface. For Q = 30 μmol/g, the estimate corresponds to one formula unit (quasi-mole-
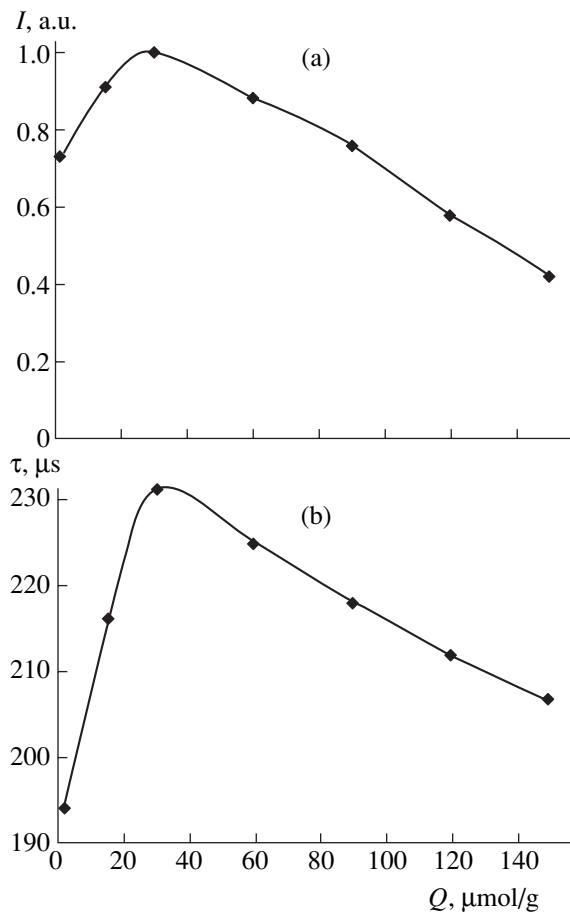

Fig. 2. Plots of (a) the intensity I of the emission band due to the hypersensitive transition and (b) the lifetime τ^* of the excited state versus $EuCl_3$ content Q in the porous glass matrix.

cule) of $EuCl_3$ per 500 Å^2 pore surface area. Therefore, the observed concentration quenching is already manifested in the region of extremely low salt coverages of the carrier surface. We may suggest that dimensions of the salt clusters formed in this system are on the order of several molecular units.

Additional information concerning the dimensions of salt particles formed in the porous glass carrier is provided by data on the luminescence quenching by adsorbed water vapor. Figure 3 shows the curves of the intensity I of the band due to the hypersensitive transition and the lifetime τ^* of the excited state plotted versus the relative humidity (p/p_0) for three $EuCl_3$/PG samples with an intercalate content of 1.5, 15, and 150 μmol/g. As can be clearly seen, the main quenching takes place in the initial stage of adsorption, which is evidence of the active incorporation of water molecules into the coordination sphere of Eu^{3+} cations, leading to the nonradiative degradation of the energy of the excited state as a result of the interaction with high-frequency oscillations ν_{OH}. It should be noted that almost compete quenching of the emission observed for Q =
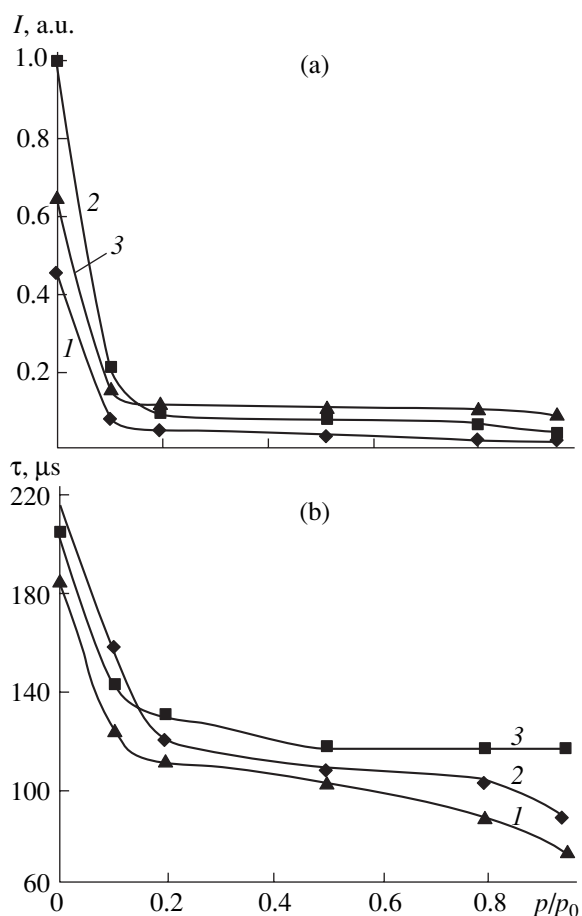
Fig. 3. Plots of (a) the intensity I of the emission band due to the hypersensitive transition and (b) the lifetime τ^* of the excited state plotted versus the relative humidity (p/p_0) for three $EuCl_3$/PG samples with an intercalate content of (*1*) 1.5, (*2*) 15, and (*3*) 150 μmol/g.

increase in the content of intercalated salt (up to $Q = 150$ μmol/g) probably leads to the formation of three-dimensional nanoparticles. In such a case, a certain fraction of Eu^{3+} cations is screened from adsorbed water and can provide for a significant residual luminescence, which is observed even in the region of capillary condensation of water in the porous glass (Fig. 3).

REFERENCES

1. G. P. Roskova and T. S. Tsekhomskaya, Fiz. Khim. Stekla **7**, 513 (1981).

2. D. Enke, F. Janowski, and W. Schwieger, Micropor. Mesopor. Mater. **60**, 19 (2003).

3. D. Sunil, H. D. Gafney, M. H. Rafailovich, *et al.*, J. Non-Cryst. Solids **319**, 154 (2003).

4. R. L. Verezhinskaya, T. M. Burkat, and V. N. Pak, Fiz. Khim. Stekla **25**, 688 (1999).

5. V. N. Pak and S. V. Sukhanov, Zh. Prikl. Khim. **76**, 1241 (2003).

6. *Modern Electroanalytical Methods: Proceedings of the International Symposium on Modern Electrochemical Methods of Analysis, Paris, 1957,* Ed. by G. Charlot (Amsterdam, New York, 1958), Part 2.

7. D. A. Andreeva and M. V. Puzyk, Opt. Spektrosk. **95**, 764 (2003) [Opt. Spectrosc. **95**, 714 (2003)].

8. M. I. Gaĭduk, V. F. Zolin, and L. S. Gaĭgerova, *Luminescence Spectra of Europium* (Nauka, Moscow, 1974) [in Russian].

9. R. R. Goncalves, Y. Messaddeq, M. Atik, and S. J. L. Ribeiro, Mater. Res. **2**, 11 (1999).

10. M. Ferrari, R. Campostrini, G. Carturan, and M. Montagna, Philos. Mag. B **65**, 251 (1992).

Translated by P. Pozdeev

1.5 and 15 μmol/g can be realized only provided that the cluster dimensions are very small, so that all cations are accessible for water molecules. A significant

SIMS Analysis of Ultrathin
Implanted Arsenic Layers in Silicon

D. S. Kibalov, O. M. Orlov, S. G. Simakin, and V. K. Smirnov

Institute of Microelectronics and Informatics, Russian Academy of Sciences, Yaroslavl, Russia
e-mail: IBTec@rambler.ru
Received May 25, 2004

Abstract—A new regime of secondary ion mass spectrometry (SIMS) is proposed, which allows a depth resolution of $\lambda = 1.4$ nm to be achieved. The profiles of arsenic implanted into silicon, measured using this regime on a Cameca IMS-4f microprobe, were close to the true distributions. SIMS profiling of the samples of silicon implanted with 30-keV As^+ ions to a total dose of $(1.25–3.13) \times 10^{13}$ cm^{-2} through a 20-nm-thick thermal oxide layer showed the presence of a sharp peak of arsenic accumulated at the oxide/silicon interface, which is explained by the diffusion of arsenic to this interface as a result of annealing. © *2004 MAIK "Nauka/Interperiodica".*

The technology of modern submicron field-effect transistors requires the formation of shallow and ultrashallow (buried at a depth below 50 nm) doped regions in silicon [1]. The depth profiling of such regions performed by secondary ion mass spectrometry (SIMS) in the stage of development of the doping technology has to be performed with a depth resolution of about 1 nm. The main aim of this study was to obtain information on the distribution of arsenic implanted into silicon and to elucidate factors responsible for the transformation of this distribution after renewal of the oxide layer and annealing of the sample.

The required depth resolution of SIMS profiling was achieved through optimization of the conditions of measurements performed on a Cameca IMS-4f microprobe equipped with a magnetic sector SIMS device. By analogy with our recent investigation [2], we tried SIMS profiling in an original regime using both negative molecular primary ions and negative molecular secondary ions. Experimental data presented in Fig. 1 show that the proposed regime provides for a significant gain in the depth resolution λ, defined as the layer thickness on the exponential part of the profile over which the impurity concentration decreases by a factor of e. Using the new regime, it was possible to obtain the As dopant profile featuring a change in the concentration by two orders of magnitude over a layer thickness within 10 nm. As can be seen from Fig. 1, a peak due to the signal of secondary $AsSi^-$ ions occurs in the region of stationary values of the signal of Si_2^- matrix ions. The depth corresponding to the onset of stationary sputtering was about 1 nm.

The initial (100)-oriented single crystal silicon plate (KDB-12 grade) with a 20-nm-thick thermal oxide layer was implanted by 30-keV As^+ ions to a total dose

of 3.13×10^{13} cm^{-2}. The SIMS profile of As in this silicon sample is shown in Fig. 2 (curve *1*). A distinctive feature of the proposed regime of analysis is an extremely low yield of $AsSi^-$ secondary ions from the SiO_2 matrix, so that the implanted As is detected almost exclusively in silicon. The next sample for SIMS profiling was a silicon plate, which differed from the previous sample in that the initial 20-nm-thick thermal oxide was removed and a new 15-nm-thick oxide layer was formed by 55-min oxidation at $T = 850°C$, followed by annealing in a dry nitrogen atmosphere ($T = 850°C$, 4 h). Figure 2 (curve *2*) shows the SIMS profile of As in this sample with a 6.6-nm displacement in depth to account for the oxide renewal procedure (this is the value by which the silicon surface decreases relative to the initial level after the formation of the new 15-nm-thick oxide layer).

As can be seen from Fig. 2, the additional treatments lead to a significant modification of the As profile. In the interval of concentrations from 3.0×10^{18} to 6.0×10^{19} cm^{-3}, the distribution of As in profile *2* is manifested by a narrow peak in the vicinity of the SiO_2–Si interface. The slope of this peak is characterized by $\lambda = 1.4$ nm. The levels of depth resolution close to this value are usually achieved in the profiles of heterostructures or the samples with δ-doped layers [3]. This result implies that As implanted to a total concentration above 3×10^{18} cm^{-3} is concentrated within a thin layer with a very sharp boundary.

The integral over profile *1* in Fig. 2 shows that the dose of arsenic implanted into the initial structure is 2.09×10^{13} cm^{-2}. For profile *2*, this value was found to be 2.06×10^{13} cm^{-2}. Therefore, renewal of the oxide layer and the subsequent annealing only lead to a redistribution of arsenic in the vicinity of the SiO_2–Si interface,

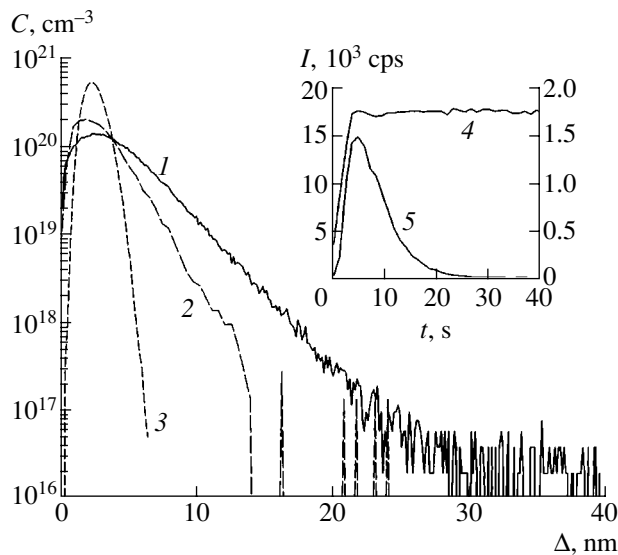**Fig. 1.** Depth–concentration (Δ–C) profiles of As implanted into silicon at an energy of 500 eV to a total dose of 1×10^{14} cm^{-2} (standard sample): (*1*) traditional SIMS profiling using primary O_2^+ ions and secondary As$^+$ ions (mass resolution, $M/\Delta M = 4200$; oxygen pressure, 2×10^{-5} Torr; $\lambda = 2.6$ nm); (*2*) negative-ion SIMS regime using primary NO_2^- ions and secondary AsSi$^-$ ions ($M/\Delta M = 2500$; without oxygen admission; $\lambda = 1.6$ nm); (*3*) simulation using TRIM program package. Primary-ion energy, 2 keV; incidence angle, 59°; ion current scale converted into concentration scale via the implantation dose; sputtering time scale converted into depth scale via the crater depth measured on a Talystep profilometer. The inset shows the time variation of the secondary ion count in regime *2* for (*4*) matrix Si_2^- ions (left scale) and (*5*) AsSi$^-$ ions (right scale).

Fig. 2. Depth–concentration profiles of As implanted into silicon for the samples with thermal oxide layers on the surface. Ion current scale converted into concentration scale via the relative sensitivity coefficient measured for a test sample of silicon implanted with 20-keV As$^+$ ions to a total dose of 5.0×10^{15} cm^{-2}.

rather than change the total content of arsenic in silicon. The shape of the profile with the As peak was reliably reproduced in a series of samples. The samples subjected to an additional short-term heating (900°C, 15 min) either before or after the main annealing (850°C, 4 h) exhibited no significant changes in comparison to profile *2* in Fig. 2. Thus, the annealing for several hours at $T = 850$°C is the main factor determining the observed As distribution.

In order to elucidate the role of oxide renewal on the distribution of As in silicon, this stage was excluded from the sample preparation procedure. Figure 2 (curve *3*) shows the distribution of As in the initial silicon plate implanted with arsenic and annealed for 3 h at 850°C. As can be seen, the As profile with a narrow peak in the region of the SiO$_2$–Si interface, analogous to that described above, is again observed. This result indicates that oxide renewal in the structure studied is not necessary for the formation of a narrow peak in the As profile.

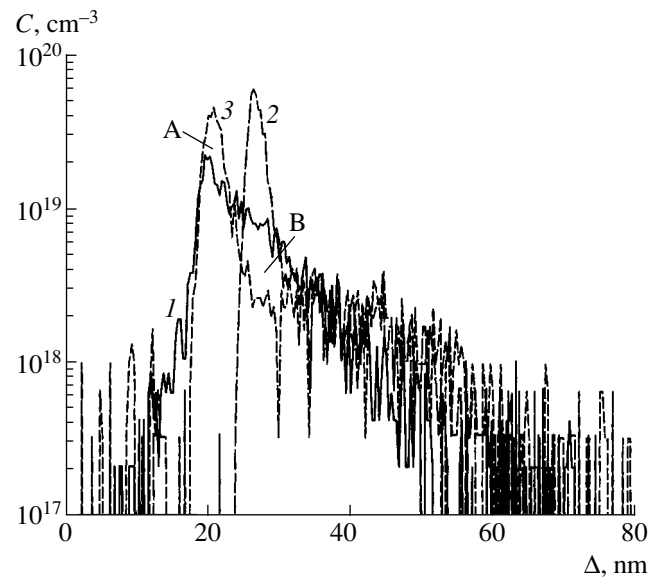The comparison of profiles in Fig. 2 allows the following assumption to be made for explaining the for-

mation of the aforementioned As peak. We believe that this peak is due to the transfer of a part of arsenic (implanted to a total concentration in excess of $(2–3) \times 10^{18}$ cm^{-3}) toward the SiO$_2$–Si interface. This is suggested by the fact that (see Fig. 2) the dose of As in region A (5.3×10^{12} cm^{-2}) between profiles *3* and *1* is close to the dose in region B (4.0×10^{12} cm^{-2}) between profiles *1* and *3*. Additional evidence in favor of the above assumption is provided by the well-known fact of the diffusion of the interstitial silicon atoms (generated by ion implantation) toward the SiO$_2$–Si interface. This diffusion flow of silicon, in turn, induces the accumulation of As atoms near the SiO$_2$–Si interface [4]. At the same time, the distribution of As in depths above 40 nm exhibits broadening upon annealing, which is related to the As diffusion in the depth of the silicon. It should be noted that a decrease in the total dose of implanted As (to 1.25×10^{13} cm^{-2}) and in the duration of annealing at 850°C (to 2 h) only leads to a decrease in the maximum concentration at the peak to 5×10^{18} cm^{-3} rather than to a change in the aforementioned concentration level. Thus, in the SiO$_2$–Si structure implanted with 30-keV As$^+$ ions to a total dose of $(1.25–3.13) \times 10^{13}$ cm^{-2}, the annealing leads to the redistribution of As by diffusion in the depth of the silicon at concentrations below $(2–3) \times 10^{18}$ cm^{-3}, whereas above this level, As tends to diffuse toward the SiO$_2$–Si interface and accumulate there with the formation of a narrow peak in the dopant profile.

In order to precisely determine the thickness of the As layer formed in the region of the SiO$_2$–Si interface, it

is necessary to restore the true distribution of the dopant using a convolution with the resolution function [5]. Such a resolution function corresponding to the conditions of depth profiling can be determined only using a special sample containing a δ layer of the given impurity. However, to the first approximation, the thickness of the As layer formed in the region of the SiO_2–Si interface can be evaluated using the profile of the standard sample presented in Fig. 1. Assuming that the results of modeling using the TRIM program package give the true As profile, we can estimate the degree of broadening of profile *3* with depth as a result of the ion beam mixing. A comparison of profiles *2* and *3* shows that the level of concentrations equal to 1/10 of the value at the peak of profile *2* is displaced by 2.5 nm relative to the true depth; by the same token, the level of 1/100 is displaced by 5.4 nm and the level of 1/1000, by 8.4 nm. Adopting this trend to profile *2* in Fig. 2, we obtain the following estimates of the true depth of the As layer relative to the SiO_2–Si: on the level of concentration corresponding to the base of the As peak (3×10^{18} cm^{-3}), the depth is 3 nm; on a level of 1×10^{18} cm^{-3}, the depth is 16 nm; and on a level of 1×10^{17} cm^{-3}, the depth is 31 nm.

In conclusion, it should be noted that the task of this study could not be completely solved on the IMS-3f instrument in the traditional regime of SIMS profiling using low-energy probing O_2^+ ions, because of insufficient depth resolution. Only due to the new regime proposed for the analysis of As in silicon, which ensured a depth resolution as fine as $\lambda = 1.4$ nm at a detection limit of 1×10^{17} cm^{-3}, was it possible to obtain almost true As profiles in the SiO_2–Si structure and to establish the factors responsible for the complicated shape of the observed implant distribution.

REFERENCES

1. S. Thompson, P. Packan, and M. Bohr, Intel Technol. J., No. Q3, 1 (1998).
2. S. G. Simakin and V. K. Smirnov, Appl. Surf. Sci. **203–204**, 314 (2003).
3. K. Wittmaack, J. Vac. Sci. Technol. B **16**, 2776 (1998).
4. G. A. Sai-Halasz, K. T. Short, and J. S. Williams, IEEE Electron Device Lett. **6**, 285 (1985).
5. M. G. Dowsett, G. Rowlands, P. N. Allen, *et al.*, Surf. Interface Anal. **21**, 310 (1994).

Translated by P. Pozdeev

Ion Energy, Charge, and Mass Distributions
in Nanosecond Surface Discharge Plasma

S. V. Barakhvostov and I. L. Muzyukin

Institute of Electrophysics, Ural Division, Russian Academy of Sciences, Yekaterinburg, 620219 Russia
e-mail: lfd@iep.uran.ru
Received May 28, 2004

Abstract—We have studied the composition of plasma formed during nanosecond high-voltage discharge at the surface of various insulators in vacuum. The flows of ions with velocities on the order of 10^2 km/s have been revealed. The energy distribution of ions in the plasma extends from several hundred electronvolts to a few kilo-electronvolts. © *2004 MAIK "Nauka/Interperiodica"*.

Introduction. The knowledge of processes determining the energy and charge distributions of particles in the plasma of high-voltage vacuum discharge is very important for the development of new sources of high-energy multiply charged ions. Surface breakdown is one of the most effective methods of generating plasma with a high content of multiply charged ions. At the same time, the presence of a high-velocity component of the ion flow in this discharge allows it to be used as a source of accelerated ions without special expensive large-size ion accelerators.

As is known, the possibility of obtaining multiply charged ions in plasma formed in the final stage of electric-arc development between insulators in vacuum is determined by the magnitude of the arc current, which can reach a level of $I \sim 10^4$–10^5 A at a microsecond pulse duration [1]. In the stage of propagation of a nanosecond surface discharge with particle velocities reaching $v \sim 10^6$ m/s, conditions at the propagating front may favor a high degree of ionization in the plasma even at significantly lower values of the current ($I < 100$ A). The results of our previous photochronographic investigations of the physical processes involved in nanosecond high-voltage vacuum discharge between an anode and the surface of an insulator showed that the discharge propagates at a velocity of $\approx 5 \times 10^6$ m/s. Therefore, we may also expect the presence of multiply charged ions in the plasma formed under such conditions.

Experimental. The experiments were performed in a vacuum of 10^{-6} Torr. The discharge gap was formed between a central anode and a system of coaxial electrodes. The vacuum gap width near the cathode was 0.5 mm. We have studied high-voltage discharge between the anode and the surface of a high-density poly(ethylene) (HDPE) or poly(tetrafluoroethylene) (PTFE). The discharge was initiated by a high-voltage pulse with an amplitude of 150 kV, a duration of 3 ns, and a leading front width of ≈ 200 ps. The results of pro-

cessing of the signals measured at the ion collector in the case of discharge at the PTFE surface showed that the maximum ion velocity was 3×10^5 m/s, at an average velocity of 1.5×10^5 m/s.

The energy, mass, and charge distributions in the plasma flow were determined using the Thomson method of parabolas. The intensity of emission in various regions of the spectrogram was digitized and accumulated over tens of measurements. Each spectrogram was obtained by accumulating the signals from up to 50 discharges. This accumulation allowed components of the ion spectrum not manifested in a single measurement to be revealed. The calculated parabolas were superimposed onto the accumulated experimental spectrograms and the relative intensities were determined for each region of the calculated curve. As a result, we obtained distributions of the ion-flow intensity with respect to the ion charge, mass, and energy. The spectrometer was calibrated with respect to the signal of hydrogen ions for discharge at the HDPE surface.

Results and discussion. Our investigation of the ion energy and charge distributions revealed high-energy multiply charged particles. Tables 1 and 2 present data on the compositions and average energies for the ions of various fractions formed during discharge at the surface of HDPE and PTFE. As can be seen, the charge distributions are characterized by a predominance of

Table 1. Ion mass, charge, and energy distributions in nanosecond discharge plasma at the HDPE surface

Ion type and charge	Content, %	Average energy, eV
H^{+1}	60	7239
C^{+4}	26	1558
C^{+3}	6.6	1622
C^{+1}	6.9	1061

Fig. 1. The energy spectra of ions formed in discharge plasma at the HDPE surface.
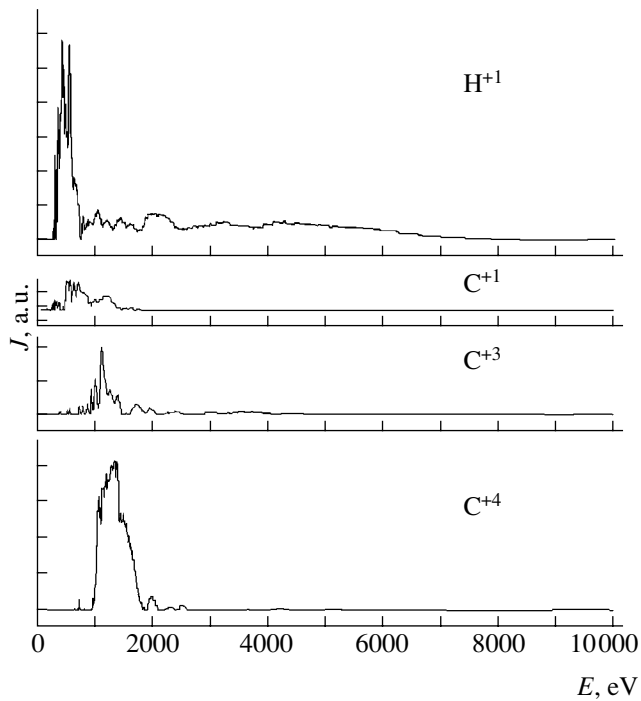

Fig. 2. The energy spectra of ions formed in discharge plasma at the PTFE surface.

multiply charged (+4 … +6) ions over the particles with smaller charge (+1 … +3).

Figures 1 and 2 show the energy distributions of each ion fraction for HDPE and PTFE, respectively. In the case of discharge at the HDPE surface, there is a group of hydrogen ions accelerated up to energies within 20–30 keV, with the main peak at 15 keV. One characteristic feature is the presence of numerous intense peaks, each having an approximately a dome shape with a thickness of several hundred electronvolts. The total width of each spectrum is 2–3 keV.

The presence of numerous peaks on the averaged background may be evidence of the existence of several principal regimes of ion acceleration. A considerable spread in the energy of light hydrogen ions may indicate that ions are accelerated by electric fields in the plasma. The most probable mechanism is via ion acceleration in the regions of kinetic instabilities developed

in the plasma, where nonstationary high-frequency electric fields are present [2]. The phenomenon of violation of the percentage ion content in the case of polyethylene requires further investigation.

Conclusions. The results of our experiments showed that nanosecond high-voltage discharge at the insulator surface offers an effective source of high-energy multiply charged ions. In view of the simple system design and availability of nanosecond high-voltage pulse generators, this type of discharge is very attractive for the development of new ion sources. A considerable spread in the energy of light hydrogen ions may be indicative of the mechanism of ion acceleration by electric fields in the plasma.

Table 2. Ion mass, charge, and energy distributions in nanosecond discharge plasma at the PTFE surface

Ion type and charge	Content, %	Average energy, eV
C^{+6}	37.8	3240
C^{+5}	24.7	3057
C^{+4}	17.7	2900
F^{+5}	15.5	3779
F^{+4}	4.2	4727

REFERENCES

1. I. G. Brown, *The Physics and Technology of Ion Sources* (Wiley, New York, 1989).
2. A. B. Mikhailovskii, *Theory of Plasma Instabilities* (Atomizdat, Moscow, 1971; Consultants Bureau, New York, 1974).

Translated by P. Pozdeev

Electrode Self-Cleaning in a Barrier Ozonizer Operating in a Turbulent Gas Flow Regime

I. M. Kirko and V. A. Kuznetsov*

Magnitogorsk State University, Magnitogorsk, Russia
* *e-mail: kuznetsov@masu.ru*
Received May 31, 2004

Abstract—The effect of self-cleaning of the discharge gaps in electric barrier ozonizers featuring a turbulent gas flow is related to the fact that the hydrodynamic forces (separating foreign solid and liquid particles from the electrode surface) predominate over electric forcers (attracting such particles to the electrodes). In this respect, ozonizers operating in a turbulent gas flow regime are advantageous over devices operating with a laminar flow. © *2004 MAIK "Nauka/Interperiodica".*

Introduction. A disadvantage of ozonizers used in the systems of water purification is the need for periodic halts of the system operation for the disassembly and prophylactic cleaning of the working electrodes. This is necessary because a thin film of nitrous bases and dust tends to deposit on the glass barriers. Contamination of the barrier surface sharply increases the surface resistance, thus detrimentally influencing the discharge conditions. Good surface resistance of the insulating barriers is necessary for retaining the optimum state of the barrier (corona) discharge in the air gaps of the ozonizer [1]. For example, in developing the project of a small ozonizing plant in Nytva (Perm oblast) for the production of no more than 1 kg ozone per hour, two ozonizers were envisaged: one device was in operation while the other was cleaned according to a special technology.

We have studied laboratory ozonizers of the Microzon type with a laminar air flow and checked the state of their electrodes after operation for 20–30 h. In the course of normal operation (in the beginning of test), all the interelectrode space is uniformly filled with a violet homogeneous glow and the device produced a weak low-frequency (~100 Hz) sound reflecting the electrostatic oscillations of the electrodes.

At the end of test, the glass barriers in the ozonizers exhibited filamentary surface discharges in the form of lighting streaks obviously possessing the character of electric arc (emitting bright white light). The character of the acoustic noise changed as well: in the presence of filamentary discharges, the sound became higher; within a few minutes after that, there was a sharp breakdown and the ozonizer failed. Examination showed that the filamentary discharge converted into spark, the glass barrier cracked in several sites, and an electric arc generated at the points of breakdown led to failure of the device.

By timely washing and drying electrodes of the ozonizer so as to avoid breakdowns, it is possible to maintain stable operation of the device. However, this procedure requires disassembly of the system and is very laborious. It was found that the situation drastically changes if the flow of air pumped through the ozonizer is turbulent. In this case, the Reynolds number reaches a level of Re = 3000–4000, which is well above the critical value characterizing the passage from laminar to turbulent regime.

This study was aimed at explaining the observed phenomenon of discharge gap self-cleaning in ozonizers operating with turbulent flow of the ozonized gas. The working hypothesis was as follows: self-cleaning of the ozonizer electrodes in a turbulent gas flow is due to the fact that the hydrodynamic forces (separating foreign solid and liquid particles from the electrode surface) predominate over electric forcers attracting such particles to the electrodes. In this context, we have calculated and compared the electric and hydrodynamic forces acting upon solid and liquid particles occurring in the discharge gap at the surface of ozonizer electrodes.

Calculation of electric forces. For the sake of simplicity, we assume that a particle occurring in the discharge gap at the surface of glass barrier has a spherical shape with the radius a and bears a charge q (Fig. 1). This charged particle is attracted to the glass surface due to electric interaction with the mirror image in the insulator possessing the charge q/ε, where ε is the permittivity of the glass barrier.

The force of electrostatic attraction according to the Coulomb law is

$$F_{\mathrm{el}} = \frac{q^2}{16\pi\varepsilon^2\varepsilon_0 a^2}. \tag{1}$$

Taking into account that the potential difference between electrodes in the ozonizer may increase only to the value of air breakdown $V_r = 1.8 \times 10^6$ V/cm, we may assume that the particle potential at the glass barrier surface may also increase only from 0 to V_r. The average value can be taken approximately equal to $0.5V_r$. Since the electric capacitance of the spherical particle is $C = 4\pi\varepsilon_0 a$, the average charge can be evaluated as $q = 2\pi\varepsilon_0 a V_r$. Substituting this value into formula (1), we obtain an expression for calculating the electric force attracting a particle to the glass barrier surface:

$$F_{el} \approx \frac{\pi\varepsilon_0 V_r^2}{4\varepsilon^2}. \tag{2}$$

Calculation of hydrodynamic forces. The electric force of attraction counteracts to a hydrodynamic force $\mathbf{F}_{din}$ arising due to a large pressure gradient at the channel wall. Now, we will calculate a projection of this force onto the Oz axis. The relative thickness of a boundary layer in the case of a turbulent air flow in the discharge gap can be approximately evaluated [2] as $\delta \approx \Delta/\sqrt{\mathrm{Re}}$, where Δ is the gap width.

The longitudinal velocity component of gas particles in the boundary layer can be approximately determined [2] as

$$V(z) \approx V_0\left(1 - e^{-\frac{z}{\delta}}\right), \tag{3}$$

where z is the distance from a point on the particle surface to the glass barrier surface. According to the Bernoulli law, the flow velocity at an arbitrary point obeys the relation

$$p(z) + \frac{\rho V^2(z)}{2} = \text{const}, \tag{4}$$

where ρ is the density of air. For any point on the surface of a particle occurring at the electrode,

$$p(z) = p_0 + \frac{\rho V_0^2}{2} - \frac{\rho V^2(z)}{2}, \tag{5}$$

where p_0 is the static pressure in the main part of the flow and V_0 is the longitudinal velocity component in this part of the flow. Using Eqs. (3) and (5), we can express the pressure difference as

$$\Delta p(z) = p(z) - p_0 = \frac{\rho V_0^2}{2} - \frac{\rho V^2(z)}{2}$$
$$= \frac{\rho V_0^2}{2}\left(1 - e^{-\frac{z}{\delta}}\right)^2 = \frac{\rho V_0^2}{2}\left(2e^{-\frac{z}{\delta}} - e^{-\frac{2z}{\delta}}\right). \tag{6}$$

In order to retain a single independent variable φ, we express z as

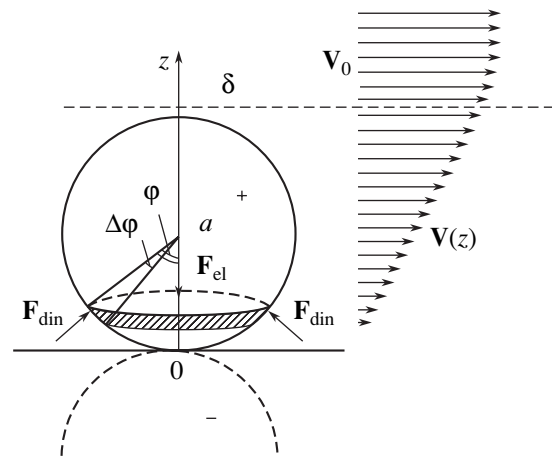$$z = a(1 - \cos\varphi). \tag{7}$$

Fig. 1. Schematic diagram illustrating the calculation of hydrodynamic and electric forces acting on a charged particle in a discharge gap of an electric barrier ozonizer (see the text for explanations).

For determining the force arising as a result of this pressure difference and driving the article to separate from the wall, we have to integrate the projection of this pressure drop onto the Oz axis over the spherical surface of the particle. The force acting on a spherical belt (Fig. 1) with the area

$$\Delta S = 2\pi a^2 \sin\varphi\Delta\varphi \tag{8}$$

can be expressed as

$$\Delta F = \Delta p \cos\varphi\Delta S$$
$$= \pi a^2 \rho V_0^2\left(2e^{-\frac{z}{\delta}} - e^{-\frac{2z}{\delta}}\right)\cos\varphi\sin\varphi\Delta\varphi. \tag{9}$$

Integrating this force over the sphere and taking into account formula (7), we obtain

$$F = \pi a^2 \rho V_0^2 \int_0^\pi \left(2e^{-\frac{a}{\delta}(1-\cos\varphi)} - e^{-\frac{2a}{\delta}(1-\cos\varphi)}\right)$$
$$\times \cos\varphi\sin\varphi d\varphi. \tag{10}$$

By changing the variable and integrating by parts, we obtain

$$F = \frac{\pi a \delta \rho V_0^2}{2}$$
$$\times \left[3 - \frac{7\delta}{2a} + 4e^{-\frac{2a}{\delta}}\left(1 + \frac{\delta}{a}\right) - e^{-\frac{4a}{\delta}}\left(1 + \frac{\delta}{2a}\right)\right]. \tag{11}$$

Introducing the convenient characteristic quantities, including the dynamic drag in the middle of the flow ($p_0 = \rho V_0^2/2$), the particle cross section ($S_0 = \pi a^2$), and
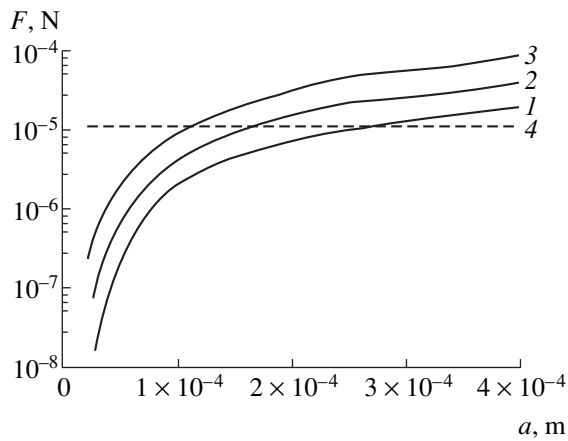
F, N

Fig. 2. A comparison of (*1–3*) hydrodynamic and (*4*) electric forces acting on charged particles of various radii at different flow velocities (m/s): (*1*) 12; (*2*) 20; (*3*) 30.

the relative diameter of the particle $D_{rel} = 2a/\delta$, we can express the hydrodynamic force as a dimensionless function of the relative diameter:

$$\Phi(D_{rel}) = \frac{2}{D_{rel}}\left[2 - \frac{7}{D_{rel}} + 4e^{-D_{rel}}\left(1 + \frac{2}{D_{rel}}\right)\right.$$
$$\left. - e^{-2D_{rel}}\left(1 + \frac{1}{D_{rel}}\right)\right]. \tag{12}$$

Finally, we obtain the dimensional dependence of the hydrodynamic force on the relative diameter:

$$F(D_{rel}) = p_0 S_0 \Phi(D_{rel}). \tag{13}$$

Discussion. Figure 2 shows a comparison of the results of calculations using Eqs. (2) and (13) for the electric and dynamic forces, respectively, acting on a particle at various flow velocities. The numerical experiments were performed for a discharge-gap width of

3 mm. As can be seen, the aerodynamic force is actually competitive with the force of electrostatic attraction. As the Reynolds number increases, the aerodynamic force becomes predominate for particles of a smaller radius. Taking into account that the calculation was performed for the maximum electric field strength, it is natural to expect that particles of a somewhat smaller size will be also separated from the barrier surface and eliminated from the discharge gap by a turbulent flow.

The results of the model calculations are confirmed in practice by the fact that the ozonizer of the Aerozon type employing turbulent flow of the ozonized gas has been operating in our laboratory for five years without prophylactic cleaning, and the electrodes in this device exhibit no contamination.

It should also be noted that contamination of the electrodes of ozonizers employing laminar gas flow leads to a decrease in the ozone yield and, hence, in the device efficiency [1]. Ozonizers operating in turbulent regime are free of this disadvantage. A decrease in the time of gas exposure to the discharge can be compensated for by multiple passages through the gap.

Conclusion. Ozonizers with a turbulent regime of gas flow through the discharge gap are preferred to the ozonizers employing laminar flow regime.

REFERENCES

1. V. G. Samoĭlovich, V. I. Gibalov, and K. V. Kozlov, *Physical Chemistry of Barrier Discharge* (Moscow State University, Moscow, 1989) [in Russian].

2. L. G. Loĭtsyanskiĭ, *Laminar Boundary Layer* (Fizmatgiz, Moscow, 1962) [in Russian].

3. I. M. Kirko and V. A. Kuznetsov, in *Proceedings of the 8th All-Russia Conference on Theoretical and Applied Mechanics, Perm, 2001* (Yekaterinburg, 2001), p. 322.

Translated by P. Pozdeev

Equilibrium Configurations of the Charged Surface of a Conducting Liquid at a Finite Interelectrode Distance

N. M. Zubarev and O. V. Zubareva

Institute of Electrophysics, Ural Division, Russian Academy of Sciences, Yekaterinburg, Russia
e-mail: nick@ami.uran.ru

Abstract—The problem of determining equilibrium configurations of the free surface of a conducting liquid is considered with allowance for a finite interelectrode distance. An analogy is established between this electrostatic problem and that of finding the profile of a progressive capillary wave on the free surface of a liquid layer of a finite depth, which was solved by Kinnersley. This analogy allowed exact solutions to be obtained for the geometry of liquid electrodes, which expand the existing notions about the possible stationary states of the system. © 2004 MAIK "Nauka/Interperiodica".

As is known [1], flat surface of a conducting liquid exposed to a sufficiently strong electric field becomes unstable. This instability is induced by the Coulomb forces, whereas capillary forces play a stabilizing role. In order to understand the main laws governing the behavior of such systems, it is necessary to establish both the conditions under which the mutual compensation of these forces is possible and the conditions under which this is basically impossible. This, in turn, makes necessary an analysis of the possible equilibrium configurations of the charged surface of liquid electrodes.

Previously [2, 3], exact solutions were obtained for the equilibrium configuration of the surface of a conducting liquid in a homogeneous electric field. In application to an analysis of the possible configurations of liquid electrodes, this situation corresponds to the formal limit of infinite interelectrode distances. The analysis in [2, 3] was based on the established analogy with the problem of the description of progressive capillary waves on the free surface of a deep ideal liquid, which was solved by Crapper in 1957. The form of equations for the two-dimensional potential of the electric field and the stream function in these problems coincide to within the notation.

This paper will demonstrate that, by expanding the aforementioned analogy to the case of a finite distance between electrodes (and, for capillary waves, to the case of a liquid layer of a finite depth), it is possible to construct exact solutions to the classical electrostatic problem for the case of a finite geometry. The corresponding solutions for progressive capillary waves were found in 1976 by Kinnersley [4]; in 1999, these solutions were obtained using a more rational method by Crowdy [5].

Now we will write a set of equations determining the equilibrium shape of the free surface of a conducting liquid for a given interelectrode distance d and a potential difference U. Let the vector of the electric field strength be directed along the y axis of a Cartesian coordinate system. In the unperturbed state, the liquid boundary is a flat horizontal surface $y = -d$, and the position of the upper (flat solid) electrode corresponds to $y = 0$. Restricting our consideration to the case of planar symmetry, we can describe the shape of a perturbed surface of the liquid electrode by the function $\eta(x)$. For incompressible liquids, the periodic solutions must obey the condition $d = -\lambda^{-1} \int_0^\lambda \eta(x)dx$, where λ is the period. The electric field potential Φ is described by the Laplace equation

$$\Phi_{xx} + \Phi_{yy} = 0,$$

which has to be solved together with the boundary conditions

$$\Phi = 0, \quad y = 0,$$

$$\Phi = U, \quad y = \eta(x).$$

The equilibrium relief of the liquid boundary is determined by the condition of the balance of forces acting upon this surface:

$$\frac{\Phi_x^2 + \Phi_y^2}{8\pi} + \frac{\alpha \eta_{xx}}{(1 + \eta_x^2)^{3/2}} = p, \quad y = \eta(x),$$

where the first term on the left-hand side describes the electrostatic pressure and the second term, the surface pressure (α is the coefficient of surface tension and p describes the difference between the external and internal pressures).
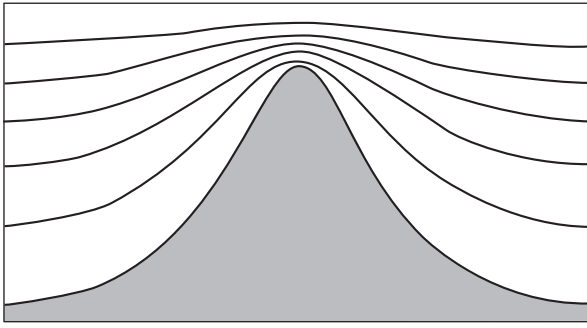
One period of a stationary profile of the free surface of a conducting liquid for $k = 0.2$ and $u = 1.8$. The curves show the equipotential surfaces $\varphi = 0.3, 0.6, 0.9, 1.2$, and 1.5.

Comparing the above equations to those [4] determining the shape of a capillary wave in the system of coordinates moving at a phase velocity c with this wave, we establish that these equations coincide to within the substitutions

$$p \longrightarrow \rho c^2/2, \quad \Phi \longrightarrow \sqrt{4\pi\rho}\,\Psi, \quad \eta \longrightarrow -\eta,$$
$$y \longrightarrow -y.$$

Here, Ψ is a stream function harmonically conjugated with the velocity potential and ρ is the liquid density. Using the known symmetric solutions of these equations (which correspond to case Ib in the notation of Kinnersley [4]), we obtain the following explicit parametric expressions describing the electric field strength distribution in the interelectrode gap:

$$x = \frac{\alpha}{2pk'^2}\Bigg[2E(\psi, k) - k'^2\psi$$

$$- 2k^2 \mathrm{sn}(\psi, k)\mathrm{cd}(\psi, k) + \frac{2kk'^2 \mathrm{sd}(\psi, k)\mathrm{nd}(\psi, k)}{\mathrm{dn}(\varphi, k') - k\mathrm{cd}(\psi, k)} \Bigg], \tag{1}$$

$$y = \frac{\alpha}{2pk'^2}\Bigg[(1 + k^2)\varphi - 2E(\varphi, k')$$

$$+ \frac{2k'^2 \mathrm{sn}(\varphi, k')\mathrm{cn}(\varphi, k')}{\mathrm{dn}(\varphi, k') - k\mathrm{cd}(\psi, k)} \Bigg]. \tag{2}$$

Here, sn, cn, dn, sd, cd, nd are the Jacobi elliptic functions; E is the incomplete elliptic integral of the second kind; k is the modulus of the elliptic integral; $k' = \sqrt{1 - k^2}$ is the complementary modulus; $\varphi = \sqrt{p/(2\pi\alpha^2)}\,\Phi$ is the dimensionless electric field potential, and ψ is the corresponding harmonically conjugated function. On the liquid surface, the potential φ

acquires the value $u = \sqrt{p/(2\pi\alpha^2)}\,U$, so that the condition $\varphi = u$ determines the unknown equilibrium surface in the parametric form (ψ plays the role of a parameter).

It should be noted that the equilibrium configurations of a charged liquid were previously studied only in a weakly nonlinear limit, where the wavelength was much greater than the amplitude of the surface deformation (see, e.g., [6–8] and references therein). Using Eqs. (1) and (2), it is possible to analyze (without allowance for the gravity field) the possible substantially nonlinear surface configurations for which the wavelengths and amplitudes are comparable (see figure). An important distinction of such an analysis from that of Kinnersley is the basically different parametrization of the solutions. In the hydrodynamic problem, the main control parameter was the phase velocity; in our case, an analog of this velocity has no physical meaning. In the electrostatic problem, the control parameters are the potential difference U and the interelectrode distance d. The latter quantity does not explicitly enter into the expressions for solutions of Eqs. (1) and (2) and can be calculated using the formula,

$$d = -\lambda^{-1} \int_0^{4K(k)} (x_\psi y)\big|_{\varphi = u}\,d\psi. \tag{3}$$

Convenient parameters characterizing the solutions are offered by the wavelength

$$\lambda = \frac{2\alpha}{pk'^2}[2E(k) - k'^2 K(k)], \tag{4}$$

where $K(k)$ and $E(k)$ are the elliptic integral of the first and second kind, respectively, and by the amplitude of the surface perturbation

$$A = \frac{1}{2}(y_{\max} - y_{\min})\big|_{\varphi = u} = \frac{\alpha k}{pk'^2}\mathrm{sc}(u, k'). \tag{5}$$

Excluding the moduli k, k' and the pressure difference p from relations (3)–(5), we obtain the dependence of the stationary wave amplitude A on the wavelength and the system parameters (the potential difference U and the interelectrode distance d). Analysis of this dependence, which is beyond the framework of this short communication, will allow us to study qualitatively the obtained solutions with respect to their stability and to formulate criteria for the growth of perturbations on the charged surface of liquid electrodes.

REFERENCES

1. Ya. I. Frenkel', Zh. Éksp. Teor. Fiz. **6**, 347 (1936).

2. N. M. Zubarev, Pis'ma Zh. Tekh. Fiz. **25** (22), 79 (1999) [Tech. Phys. Lett. **25**, 920 (1999)].

3. N. M. Zubarev, Zh. Éksp. Teor. Fiz. **116**, 1990 (1999) [JETP **89**, 1078 (1999)].

4. W. Kinnersley, J. Fluid Mech. **77**, 229 (1976).

5. D. G. Crowdy, J. Nonlinear Sci. **9**, 615 (1999).

6. L. P. Gor'kov and D. M. Chernikova, Dokl. Akad. Nauk SSSR **228**, 829 (1976) [Sov. Phys. Dokl. **21**, 328 (1976)].

7. V. B. Shikin and Yu. P. Monarkha, *Two-Dimensional Charged Systems in Helium* (Nauka, Moscow, 1989) [in Russian].

8. V. Shikin and P. Leiderer, Fiz. Nizk. Temp. **23**, 624 (1997).

Translated by P. Pozdeev

An Analog of the Normal Current Density Effect in Barrier Discharge

D. A. Malik, K. E. Orlov*, and A. S. Smirnov
St. Petersburg State Technical University, St. Petersburg, 195251 Russia
* e-mail: orlov@phtf.stu.neva.ru
Received June 10, 2004

Abstract—We have experimentally studied the regimes of homogeneous barrier discharge operation in air at reduced pressure and observed behavior analogous to the normal current density effect in a dc discharge. © 2004 MAIK "Nauka/Interperiodica".

Barrier discharge is known as an effective means of generating nonequilibrium plasma at high pressures of a working gas. Although the first experiments with barrier discharge were performed more than a century ago [1], the most extensive investigations have been undertaken in the past two decades. This discharge is now widely used for the synthesis of ozone, modification of surfaces, deposition of coatings, destruction of nitrogen oxides, and excitation of excimer lamps and plasma displays [2].

Barrier discharge may exist in various forms [2–4]. Depending on the composition and pressure of the working gas, the thickness and material of the dielectric, and the interelectrode distance, the barrier discharge may take the form of a group of filaments (filamentary mode), spatially organized spots (spot mode), or spatially homogeneous plasma (diffuse mode). In the latter case, a homogeneous breakdown takes place over the entire volume of the discharge gap, and a nonequilibrium plasma uniformly fills the entire gap. The current flow through the plasma leads to a gradual decrease in the voltage drop across the gap as a result of the charging of the dielectric surface. When the electric field strength in the gap is insufficient to maintain the necessary level of ionization, the plasma exhibits decay. Upon switching the polarity of the voltage applied to the electrodes, a new breakdown takes place, and the current flows in the reverse direction.

In recent years, the diffuse form of barrier discharge has been frequently referred to in the literature as atmospheric pressure glow and considered as a promising and relatively simple method of obtaining homogeneous nonequilibrium plasmas at high pressures. As a rule, homogeneous atmospheric pressure glow is most readily obtained in pure helium or in mixtures where helium is the dominating component [5]. Homogeneous forms of barrier discharge are also readily obtained at reduced pressures. Recently [6], it was demonstrated that the transitions between spark and homogeneous forms of barrier discharge could be

determined by the regime of matching of a high-frequency oscillator to discharge. Although the number of publications on the subject is continuously increasing, the possible scenarios of the breakage of a homogeneous barrier discharge are not yet established and explained.

This paper presents the results of an experimental investigation of the electric parameters of barrier discharge in air at reduced pressures. The experiments used the experimental setup schematically depicted in Fig. 1. The discharge was initiated between two aluminum electrodes, both with a diameter of 30 mm. The electrodes were coated by insulating films of aluminum
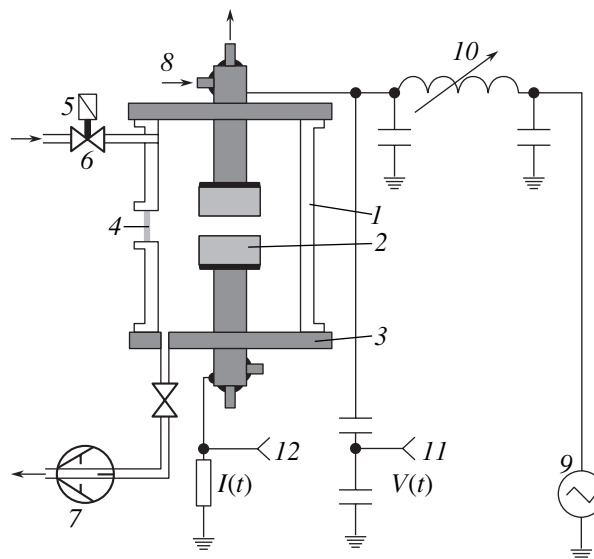

Fig. 1. Schematic diagram of the experimental setup: (*1*) plexiglas discharge chamber; (*2*) aluminum electrodes; (*3*) brass base; (*4*) quartz window; (*5*) gas inlet; (*6*) gas valve; (*7*) pumping; (*8*) water cooling; (*9*) high-frequency voltage oscillator; (*10*) resonance matching system; (*11*) voltage divider; (*12*) current shunt.

oxide. The oxide layer thickness was varied from 40 to 200 μm and the interelectrode distance, from 2 to 6 mm. The voltage with a frequency of 50–200 kHz was applied to the electrodes via tunable resonance matching system. The power amplifier (100 W) was operating in a switching mode. The voltages between electrodes and the discharge current were measured using a capacitive divider and a shunt. The signal shapes were observed with a 50-MHz digital oscillograph, digitized, and stored in a computer for digital processing. The electric power deposited in the discharge was calculated as a product of the instantaneous values of current and voltage averaged over many periods.

Figure 2 shows the typical plots of the power deposited in the discharge versus voltage between electrodes. As can be seen, the characteristics exhibit two regions with different slopes. At a minimum applied voltage, the plasma occupies only a part of the electrode surface. As the voltage is increased, the glow region expands and the power grows, which corresponds to the left-hand branch of the characteristics in Fig. 2. The bending point corresponds to the situation in which plasma occupies the entire electrode surface. A subsequent increase in the applied voltage is accompanied by a much slower increase in the deposited power. The discharge gradually spreads to the side surfaces of the electrodes. We may suggest that the increase in power on the right-hand branch of the characteristic is partly due to an increase in the effective area of discharge. If this assumption is valid, the right-hand branch of the characteristic for systems with a large ratio of the linear size of electrodes to the interelectrode distance will be even less sloped or even horizontal.

This behavior resembles the effect of the normal current density in a dc glow discharge. However, because of the basically nonstationary character of current passage through the plasma of a barrier discharge, it would be expedient to introduce the normal power density corresponding to the bending point of the characteristics depicted in Fig. 2. The value of the normal power density increases with the frequency of the applied voltage, which approximately corresponds to a constant power deposited with a single pulse of discharge current. As the working gas pressure grows, the normal power density increases. However, under otherwise fixed parameters (dielectric layer thickness, voltage frequency, interelectrode distance), there exists a threshold pressure above which the glow discharge exhibits a transition to a filamentary form.
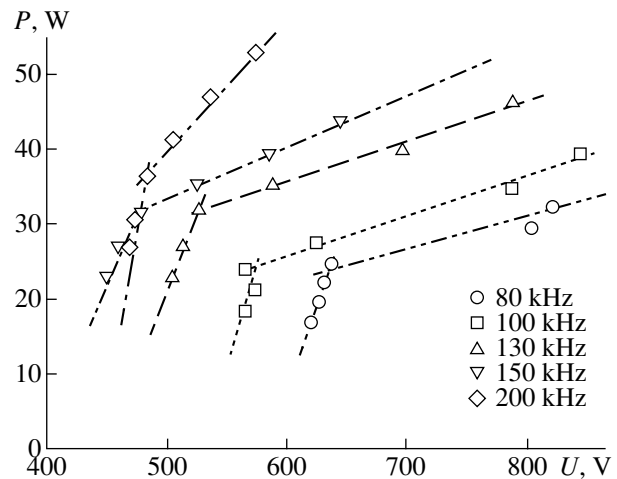

Fig. 2. Plots of the power deposited in discharge at various frequencies versus voltage between electrodes for discharge in air at 20 Torr between electrodes spaced by 4.4 mm and coated with 140-μm-thick insulating film.

We believe that observation of the phenomenon of normal power density has become possible due to certain features of the matching system. The role of the resonance matching system is equivalent to a ballast resistor in a dc discharge circuit and, similar to the case of dc discharge, this resonance matching makes it possible to observe the regimes of barrier discharge with a partly filled electrode surface and the normal power density effect.

REFERENCES

1. W. Siemens, Poggendorff's Ann. Phys. Chem. **102**, 66 (1857).
2. U. Kogelschatz, Plasma Chem. Plasma Process. **23**, 1 (2003).
3. U. Kogelschatz, IEEE Trans. Plasma Sci. **30**, 1400 (2002).
4. G. J. Pietsch, Contrib. Plasma Phys. **41**, 620 (2001).
5. F. Massines, A. Rabeli, P. Decomps, *et al.*, J. Appl. Phys. **83**, 2950 (1998).
6. Z. Chen, IEEE Trans. Plasma Sci. **30**, 1922 (2002).

Translated by P. Pozdeev

The Effect of Optical Activity on the Coherent Interaction of Screening Solitons in a Cubic Photorefractive Crystal

V. V. Shepelevich[a],*, A. A. Golub[a], R. Kowarschik[b], A. Kiessling[b], and V. Matusevich[b]

[a] Mozyr State Pedagogical University, Mozyr, Gomel oblast, Belarus
[b] Fridrich Schiller University, D-07743 Jena, Germany
* e-mail: vasshep@inbox.ru
Received April 9, 2004

Abstract—The coherent interaction of solitonlike beams in a cubic photorefractive crystal of sillenite type has been studied by method of numerical modeling. The effect of optical activity on the attraction and repulsion of light beams is considered for various orientations of the external electric field. © *2004 MAIK "Nauka/Interperiodica".*

The interaction of spatial solitons in photorefractive crystals attracted attention because this phenomenon can be used as a means of optical-beam switching [1, 2]. The problem of interacting solitons has been extensively studied [3–8]. The first experiment in which parallel Gaussian light beams of the same polarization exhibited coherent interaction in a $Bi_{12}TiO_{20}$ (BTO) crystal under the action of an applied electric field was performed and interpreted by Garsia-Quirino *et al.* [4]. However, despite the fact that BTO crystal is optically active, the effect of this activity on the interaction of light beams in that experiment was not studied because the rotatory power for the light wavelength used ($\lambda = 0.6328$ μm) was as small as 6.3°/mm and could be ignored for the 9-mm-thick BTO crystal studied.

The first experimental observation of the coherent interaction between one-dimensional bright photorefractive screening solitons in a barium strontium niobate crystal was reported by Meng *et al.* [6]. Clear physical interpretation of the nature of soliton attraction and repulsion in cases of both coherent and noncoherent interaction was presented in [5, 6]. In recent years, there have been a number of investigations of the effect of optical activity on the propagation of solitonlike beams in photorefractive crystals of the sillenite type (see, e.g., [9–14]). However, to our knowledge, the effect of optical activity on the interaction of solitonlike beams in photorefractive sillenites was not studied.

This Letter presents the results of a theoretical investigation and computer simulation of the coherent interaction between two beams propagating in a BTO crystal featuring a quasi-soliton regime with allowance for the optical activity of the medium. Based on these data, we will consider the effect of optical activity on the attraction and repulsion of light beams.

The computer simulation was performed using a one-dimensional Gaussian laser beam model and assuming that the crystal features a drift nonlinearity

regime favoring the formation of screening solitons [15]. Propagation of the light beams was described using an equation for the vector envelope $\mathbf{A}(x, z)$ of the complex amplitude of the laser radiation field in a paraxial approximation [9, 11, 14]:

$$
i\frac{\partial \mathbf{A}}{\partial z} + \frac{1}{2k_0 n_0}\frac{\partial^2 \mathbf{A}}{\partial x^2}
$$
$$
-\frac{k_0 n_0^3}{2}\frac{I_\infty + I_d}{I_d + I(x, z)}(\mathbf{A}\hat{r}\mathbf{E}_0) + i\rho[\mathbf{e}_z, \mathbf{A}] = 0. \tag{1}
$$

Here, k_0 is the length of the wave vector of the monochromatic light beam, n_0 is the unperturbed refractive index of the crystal, $\hat{r}$ is the electrooptical tensor of the third rank for the class 23 crystal, $I(x, z)$ is the light beam intensity, I_d is the dark intensity (in the general case, including the background radiation intensity), and ρ is the rotatory power of the crystal. The z axis of the Cartesian coordinate system coincides with the direction of light beam propagation, and the x axis is parallel to the external electric field $\mathbf{E}_0$ applied to the crystal.

Let us represent vector $\mathbf{A}$ in the following form [16]:

$$
\mathbf{A} = A_x\mathbf{e}_x + A_y\mathbf{e}_y = (2\eta_0 I_d/n_0)^{1/2}(u\mathbf{e}_x + v\mathbf{e}_y),
$$

where $\mathbf{e}_x$ and $\mathbf{e}_y$ are the unit vectors of the coordinate system; A_x and A_y are the projections of vector $\mathbf{A}$ onto the x and y axes, respectively; u and v are the dimensionless polarization components of the normalized light beam envelope vector; and $\eta_0 = (\mu_0/\varepsilon_0)^{1/2}$. Passing to the dimensionless variables $s = x/x_0$ and $\xi = z/(kx_0)$ (where x_0 is an arbitrary spatial width [16]) and introducing the dimensionless parameters $\beta =$

$(n_0^4 k_0^2 x_0^2 r_{41} E_0)/2$ and $\delta = n_0 k_0 x_0^2 \rho$ (where r_{41} is the electrooptical tensor component), we obtain the following system of differential equations for the polarization components u and v:

$$i\frac{\partial u}{\partial \xi} + \frac{1}{2}\frac{\partial^2 u}{\partial s^2} - \beta(1+\gamma)\frac{\mu_1 u + \mu_2 v}{1 + |u|^2 + |v|^2} - \delta v = 0,$$

$$i\frac{\partial v}{\partial \xi} + \frac{1}{2}\frac{\partial^2 v}{\partial s^2} - \beta(1+\gamma)\frac{\mu_2 u + \mu_3 v}{1 + |u|^2 + |v|^2} + \delta u = 0,$$

(2)

where $\gamma = I_\infty/I_d$,

$$\mu_1 = 3\sin\theta\cos^2\theta,$$

$$\mu_2 = \cos\theta(1 - 3\sin^2\theta),$$ (3)

$$\mu_3 = \sin\theta(1 - 3\cos^2\theta),$$

and θ is the angle between the crystallographic direction $[1\bar{1}0]$ and the electric field vector. When deriving Eqs. (2), we used the expression for the light field intensity $I(x, z) = (n_0/2\eta_0)(|A_x|^2 + |A_y|^2) = I_d(|u|^2 + |v|^2)$ [9].

The system of normalized equations (2), which differs from the system studied previously [9, 10] by an arbitrary orientation of the external electric field in the $(\bar{1}\bar{1}0)$ plane relative to the crystallographic coordinate system, was used for the numerical modeling of the interaction between light beams in cubic photorefractive crystals.

Let two one-dimensional coherent parallel Gaussian beams of a He–Ne laser propagate in a cubic, $(\bar{1}\bar{1}0)$-cut optically active photorefractive BTO crystal of symmetry class 23. First, we will consider the case in which the light beams interact in the BTO crystal under conditions close to those studied in the aforementioned first experiment [4] on the interaction of solitons in this crystal. The set of crystal parameters was selected as follows: $n_0 = 2.25$; $r_{41} = 6.175 \times 10^{-12}$ m/V; $\rho = 6.3°$/mm; crystal thickness $d = 18$ mm. The applied electric field strength was $E_0 = 9$ kV/cm. The input beams had Gaussian profiles with a halfwidth of $x_0 = 19.5$ μm, $\gamma = 0$, and $I_{max}/I_d = 1$. The beams were linearly polarized along the y axis and spaced by 39 μm. The angle between the electric field vector and the $[1\bar{1}0]$ direction was $\theta = 90°$.

Let the phase difference Δ between the interacting light beams be zero (Fig. 1a). Comparing the normalized intensity of the combined beam in the middle of the crystal ($z = 9$ mm) calculated without (curve 1) and with (curve 2) allowance for the optical activity of the crystal, we may conclude that the effect of this activity in a BTO crystal of medium thickness (below 1 cm) for
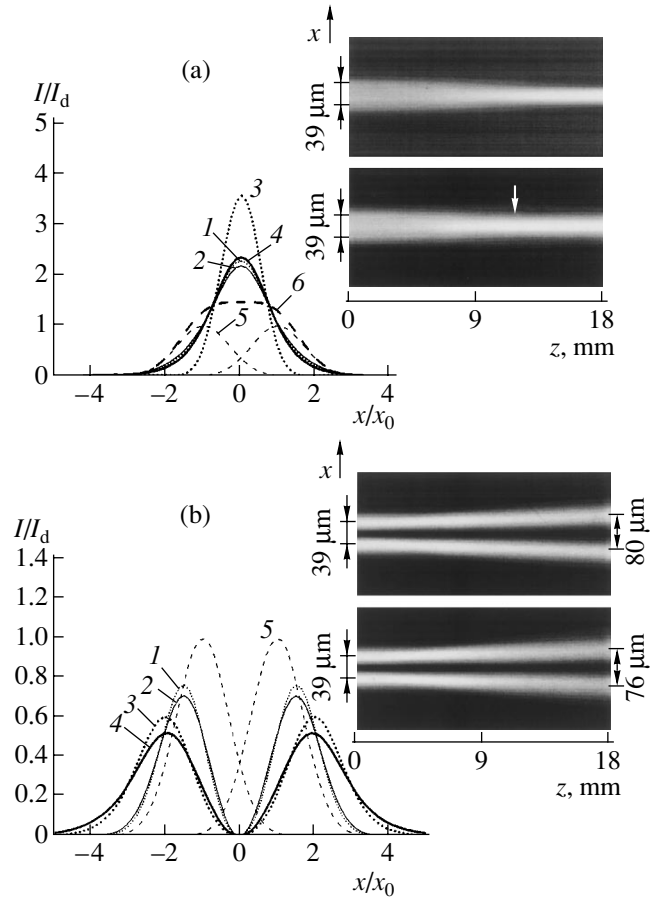

Fig. 1. The results of a computer simulation of the interaction of two Gaussian light beams in a BTO crystal under experimental conditions studied in [4], showing the intensity profiles of the light beams at various distances z from the front face of the crystal and various values of the rotatory power ρ: (a) phase difference between interacting beams $\Delta = 0$; (1) $z = 9$ mm, $\rho = 0$; (2) $z = 9$ mm, $\rho = 6.3°$/mm; (3) $z = 18$ mm, $\rho = 0$; (4) $z = 18$ mm, $\rho = 6.3°$/mm; (5) $z = 0$, individual initial beams; (6) $z = 0$, coherently superimposed beams; (b) phase difference between interacting beams $\Delta = \pi$; (1) $z = 9$ mm, $\rho = 0$; (2) $z = 9$ mm, $\rho = 6.3°$/mm; (3) $z = 18$ mm, $\rho = 0$; (4) $z = 18$ mm, $\rho = 6.3°$/mm; (5) $z = 0$, individual initial beams. The insets show the tone diagrams of the intensity distribution for the light beams interacting (top) in the crystal without optical activity and (bottom) in the optically active crystal with $\rho = 6.3°$/mm (the arrow in the bottom diagram in the inset in Fig. 1a indicates the intensity maximum of the combined beam).

moderate values of the electric field strength (about 10 kV/cm) is small and that the neglect of this effect in interpretation of the experimental data in [4] was quite justified. On the other hand, comparing the results of numerical calculations of the light intensity (Fig. 1a) at the output of our crystal ($z = 18$ mm) without (curve 3) and with (curve 4) allowance for the optical activity shows that the optically active crystal significantly decreases self-focusing of the combined beam in the course of attraction of the component beams. Thus, the effect of the optical activity of the BTO crystal with a thickness exceeding 15 mm is substantial.
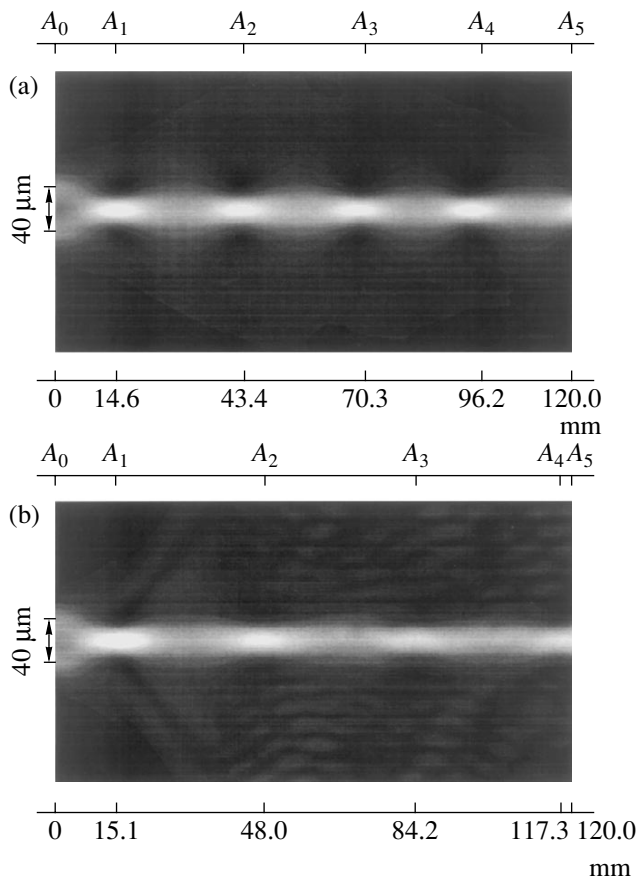
Fig. 2. Computer-simulated distributions of the intensity of two Gaussian light beams with $\Delta = 0$ interacting in a regime of quasi-soliton propagation in a thick BTO crystal (a) without optical activity and (b) with a rotatory power of $\rho = 6.3°/mm$. The maximum relative intensity at various points: (a) $I/I_d = 3.3$ (A_1), 3 (A_2), 3 (A_3), 3 (A_4), 2.5 (A_5); (b) $I/I_d = 3$ (A_1), 2.3 (A_2), 2 (A_3), 2 (A_4).

A comparison of the tone diagrams in the inset in Fig. 1a shows that the optically active crystal significantly increases the halfwidth and decreases the maximum intensity of the combined beam at the points of maximum narrowing (see the bottom diagram). It should be noted that the maximum narrowing in the crystal without optical activity (see the top diagram) is observed for $z > 18$ mm ($z = 19.6$ mm), while the minimum beam halfwidth in the optically active crystal is observed at $z = 13.6$ mm.

In the case in which the phase difference between the interacting light beams is $\Delta = \pi$ (Fig. 1b), the interference of beams in the zone of their superposition is destructive and there appears a region of zero intensity (near $x = 0$), which gradually increases as a result of the diffraction blurring of the beams. This leads to deformation of the wave front of the beams and explains their repulsion in the course of propagation. The nonlinear properties of the crystal are manifested by an increase of the refractive index in the regions of the maximum intensity of the light field in comparison to the other regions. In the regions of maximum intensity, the beams exhibit self-focusing and, hence, their mutual repulsion decreases. The optical activity decreases self-focusing as a result of the rotation of the polarization plane of the light beams, since their initial polarization was optimum. For this reason, the maxima of curves *1* and *3* in Fig. 1b are situated above the maxima of curves *2* and *4*. Accordingly, the repulsing beams on the bottom diagram (see the inset in Fig. 1b) corresponding to the optically active crystal are more blurred than on the top diagram (in the absence of optical activity). In addition, note that the optically active medium slightly decreases the mutual repulsion of the light beams, which is manifested by lower separation of their intensity maxima (curves *2* and *4*), in comparison to the case where the optical activity is ignored (curves *1* and *3*).

Although the geometry of beam interaction, the parameters of the light beams, and their spacing are the same as in the experiment performed in [4], these conditions are not optimum from the standpoint of illustrative physical interpretation and effective self-focusing. Indeed, the interaction of beams under these conditions does not allow us to observe clearly the process of attraction, since the beams are already combined at the crystal input (see the tone diagrams in the inset in Fig. 1a) because their spatial separation is small. Moreover, the selected crystal thickness does not allow us to study the periodic character of spatial pulsation (focusing and defocusing) in such a combined beam in the case of attraction of its components (see Fig. 1a) because the crystal regions under consideration contain only one intensity maximum of the combined beam (indicated by the arrow in the bottom diagram in the inset in Fig. 1a) or the intensity maximum is not at all reached within the crystal (top diagram in the inset in Fig. 1a).

In order to provide for a more clear representation of the picture of quasi-soliton interaction, let us consider two parallel light beams with a halfwidth of $x_0 = 15$ μm, linearly polarized along the x axis and propagating in the BTO crystal at a distance of 40 μm from each other. The external electric field has a strength of $E_0 \cong 14$ kV/cm and is oriented at an angle of $\theta = 35.3°$. The choice of the electric field direction is based on the results obtained in [14], where it was shown that this orientation is optimum for the effective self-focusing. All other characteristics of the beams and BTO crystal remain the same.

Since the Gaussian beam shape differs from that of the true soliton beam, we may only speak of solitonlike beam propagation, even without taking into account the optical activity of the medium. The curve of the existence of a soliton beam with $x_0 = 15$ μm [6] suggests an external field strength of $E_0 \cong 15.2$ kV/cm, but we select $E_0 \cong 14$ kV/cm because this field strength ensures almost constant intensity of separate Gaussian beam along the z axis.

Let us consider the physical explanation of the phenomenon of spatially periodic pulsation of the intensity of a combined beam obtained as a result of the interaction of two Gaussian beams in a crystal of sufficient thickness (Fig. 2). When the phase difference between the entering light beams is absent, $\Delta = 0$, their coherent interaction leads to the formation of a combined beam with a large maximum intensity ($I_{max}/I_d = 2$). This shifts the combined beam on the curve of existence [6] and leads to a decrease in the width of the resulting soliton-like beam. For this beam, the applied electric field strength is insufficient to compensate for the diffraction divergence and the beam begins to blur. When the beam travels a certain distance, its beam width increases, and the field strength becomes again sufficient to provide for self-focusing. This process is repeated to give the pattern depicted in Fig. 2a.

Theoretical calculations showed that, in the case in which the optical activity of the photorefractive crystal is taken into account, the distance between intensity maxima in the combined beam increases, while the value of intensity in these maxima decreases (Fig. 2b). In order to provide for a solitonlike regime of propagation of a Gaussian beam in a photorefractive optically active BTO crystal, it is necessary to apply a field with a strength of 19 kV/cm.

In conclusion, we have qualitatively and quantitatively evaluated the influence of optical activity on the interaction of light beams in cubic photorefractive crystals.

REFERENCES

1. G. A. Swartzlander, Jr., Opt. Lett. **17**, 493 (1992).
2. N. Akhmediev and A. Ankiewics, Opt. Commun. **100**, 183 (1993).
3. S. R. Singh and D. N. Christodoulides, Opt. Commun. **118**, 569 (1995).
4. G. S. Garsia-Quirino, M. D. Iturbe-Castillo, V. A. Vysloukh, *et al.*, Opt. Lett. **22**, 154 (1997).
5. M. Shih and M. Segev, Opt. Lett. **21**, 1538 (1996).
6. H. Meng, G. Salamo, M. Shih, and M. Segev, Opt. Lett. **22**, 448 (1997).
7. A. V. Mamaev, M. Saffman, and A. A. Zozulya, J. Opt. Soc. Am. B **15**, 2079 (1998).
8. W. Krolikowski, C. Denz, A. Stepken, *et al.*, Quantum Semiclassic. Opt. **10**, 823 (1998).
9. S. R. Singh and D. N. Christodoulides, J. Opt. Soc. Am. B **13**, 719 (1996).
10. W. Krolikowski, N. Akhmediev, R. D. Andersen, and B. Luther-Davies, Opt. Commun. **132**, 179 (1996).
11. E. Fazio, V. Babin, M. Bertolotti, and V. Vlad, Phys. Rev. E **66**, 016605 (2002).
12. E. Fazio, W. Ramadan, M. Bertolotti, *et al.*, Phys. Rev. E **67**, 026611 (2003).
13. E. Fazio, W. Ramadan, A. Belardini, *et al.*, J. Opt. A: Pure Appl. Opt. **5**, S119 (2002).
14. V. V. Shepelevich, R. Kovarshik, A. Kisling, *et al.*, Kvantovaya Élektron. (Moscow) **33**, 446 (2003).
15. M. P. Petrov, S. I. Stepanov, and A. V. Khomenko, *Photorefractive Crystals in Coherent Optics* (Nauka, St. Petersburg, 1992) [in Russian].
16. D. N. Christodoulides and M. I. Carvalho, J. Opt. Soc. Am. B **12**, 1628 (1995).

Translated by P. Pozdeev

Inverse Skin Effect

N. I. Kuskova

Institute of Pulsed Processes and Technologies, National Academy of Sciences of Ukraine, Nikolaev, Ukraine
Received April 20, 2004

Abstract—Analytical expressions describing the distribution of the magnetic field and the current density in a cylindrical conductor are obtained in the case of rapid oscillatory variation of the external field. When the field decreases, the system features the inverse skin effect, whereby the current density is maximum in the central part of the conductor. © 2004 MAIK "Nauka/Interperiodica".

As is known [1], rapid periodic variations of the external electromagnetic field $\sim e^{i\omega t}$ at a frequency ω applied to a relatively thin cylindrical conductor result in the so-called skin effect, whereby the current flows only in a thin near-surface (skin) layer of the conductor with the effective thickness

$$\delta = \sqrt{\frac{2}{\mu\sigma\omega}}, \tag{1}$$

where μ is the magnetic permeability and σ is the electric conductivity.

It was demonstrated [1–3] that, when the current varies according to an exponential law ($\sim e^{\beta t}$), the current density distribution changes depending on whether the current increases or decreases. However, the fields and the currents in electric circuits most frequently have the character of oscillations. Therefore, it would be of interest to find analytical solutions of the equation of magnetic field diffusion in the case when a nonstationary boundary condition on the surface of a cylindrical conductor with a radius a has the form of a sinusoidal function.

The diffusion of a magnetic field into a cylindrical conductor of infinite length can be described by the diffusion equation

$$\frac{\partial}{\partial r}\left[\frac{1}{r}\frac{\partial}{\partial r}(rB_\varphi)\right] = \mu\sigma\frac{\partial B_\varphi}{\partial t}, \tag{2}$$

where B_φ is the magnetic induction.

Separating variables and using the relation $B_\varphi(r, t) = B(r)b(t)$, we obtain two equations:

$$\mu\sigma\frac{\dot{b}}{b} = \lambda^2, \tag{3}$$

$$\frac{1}{B}\frac{\partial}{\partial r}\left[\frac{1}{r}\frac{\partial}{\partial r}(rB_\varphi)\right] = \lambda^2, \tag{4}$$

where λ and the eigenvalues determined from the boundary condition $B(a, t) = B_0\sin\omega t$.

The eigenfunction for the system of equations (3) and (4) are as follows:

$$
\begin{aligned}
&B(r, t) \\
&= C\sum_{n=0}^{\infty}\left[\frac{1}{2^{2n+1}n!(n+1)!}(\lambda r)^{2n+1}\right]\exp\left(\frac{\lambda^2 t}{\mu\sigma}\right),
\end{aligned}
\tag{5}
$$

where the constant C is determined from the condition $B(a, \pi/2\omega) = B_0$:

$$C = \frac{B_0}{\displaystyle\sum_{n=0}^{\infty}\frac{(\lambda a)^{2n+1}}{2^{2n+1}n!(n+1)!}}\exp\left(-\frac{\pi}{2}\frac{\lambda^2}{\mu\sigma\omega}\right). \tag{6}$$

In order to determine the eigenvalue λ, let us expand the temporal components of the eigenfunctions and $\sin\omega t$ into series. Putting the common multiplier in front of the brackets, we obtain the equation

$$\sum_{k=1}^{\infty}\frac{(\omega t)^{2k+1}}{(2k+1)!}\left[\left(\frac{\lambda^2}{\mu\sigma\omega}\right)^{2k+1}\exp\left(-\frac{\pi\lambda_2^2}{2\mu\sigma\omega}\right)-(-1)^k\right] = 0. \tag{7}$$

Since the sum of the power series is zero when all coefficients are zero, the equation can be written in the following form:

$$\left(\frac{\lambda^2}{\mu\sigma\omega}\right)^{2k+1}\exp\left(-\frac{\pi\lambda^2}{2\mu\sigma\omega}\right) = (-1)^k. \tag{8}$$

Taking the root of the $(2k+1)$th power and multiplying Eq. (8) by $\pi/2$, we obtain

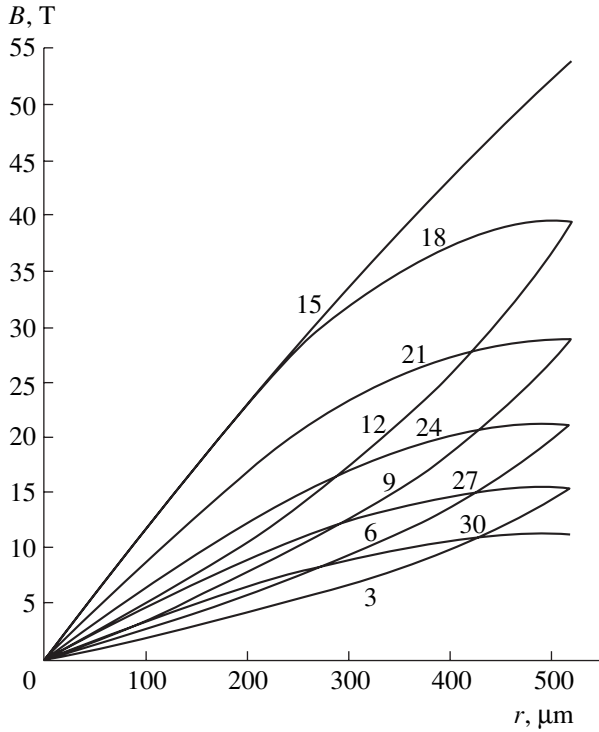$$x\exp\left(-\frac{x}{2k+1}\right) = (-1)^k\frac{\pi}{2}, \tag{9}$$

Fig. 1. Radial profiles of the magnetic induction in a cylindrical conductor at various moments (time in nanoseconds is indicated at the curves).
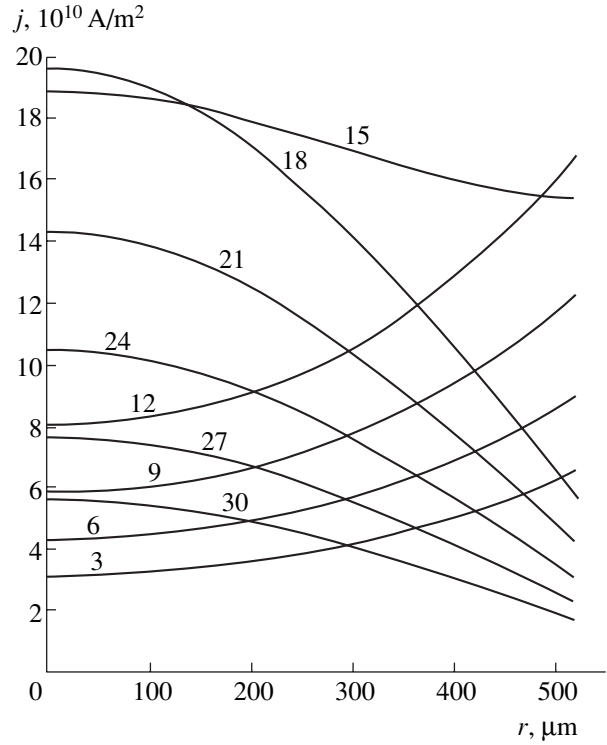

Fig. 2. Radial profiles of the current density in a cylindrical conductor (time in nanoseconds is indicated at the curves).

where $x = \pi\lambda^2/(2\mu\sigma\omega)$. For $k \longrightarrow \infty$, we have $\exp\left(-\dfrac{x}{2k+1}\right) \longrightarrow 1$ and $x \longrightarrow \pm\dfrac{\pi}{2}$. The eigenvalues determined by Eq. (9) are $\lambda_k^2 \approx \pm l_k^2 \mu\sigma\omega$, where $l_0 \approx 0.7$, $l_1 \approx 0.8$, $l_2 \approx 0.9$, ... $l_k \approx 1$. Since the sequence of l rapidly converges to unity, we may adopt $\lambda_1 \approx \pm\sqrt{\mu\sigma\omega}$ and $\lambda_2 \approx i\sqrt{\mu\sigma\omega}$, or $\lambda_1 = \delta^{-1}$ and $\lambda_2 = i\delta^{-1}$, where

$$\delta = \sqrt{\frac{1}{\mu\sigma\omega}}. \qquad (10)$$

Note that the obtained expression for the skin layer thickness (10) differs from the well-known formula (1) by the factor $\sqrt{2}$.

Taking into account that the radial part of function (5) is odd, we have to select the positive eigenvalue λ_1.

Since $(\lambda_2 r)^{2n+1} = (i)^{2n+1}\left(\dfrac{r}{\delta}\right)^{2n+1} = i(-1)^n\left(\dfrac{r}{\delta}\right)^{2n+1}$,

the general form of the approximate solution for the increasing field at the conductor surface ($\omega t < \pi/2$) is

$$B_1(r, t)$$

$$\approx C_1 \sum_{n=0}^{\infty}\left[\frac{1}{2^{2n+1}n!(n+1)!}\left(\frac{r}{\delta}\right)^{2n+1}\right]\exp\left(\omega t - \frac{\pi}{2}\right), \qquad (11)$$

and for the decreasing field ($\omega t < \pi/2$),

$$B_2(r, t) \approx C_2 J_1\left(\frac{r}{\delta}\right)\exp\left(\frac{\pi}{2} - \omega t\right), \qquad (12)$$

$$C_1 = \frac{B_0}{\displaystyle\sum_{n=0}^{\infty}\frac{1}{2^{2n+1}n!(n+1)!}\left(\frac{a}{\delta}\right)^{2n+1}}, \quad C_2 = \frac{B_0}{J_1\left(\dfrac{a}{\delta}\right)},$$

where $J_1(r/\delta)$ is the Bessel function of the first kind.

For $\omega t = \pi/2$, the functions $B_1(r, t)$ and $B_2(r, t)$ can be matched using the relation

$$B\left(r, \frac{\pi}{2\omega}\right) = \frac{1}{2}\left[B_1\left(r, \frac{\pi}{2\omega}\right) + B_2\left(r, \frac{\pi}{2\omega}\right)\right]. \qquad (13)$$

Thus, the radial distribution of the current density $j_{1,2} = \dfrac{1}{\mu r}\dfrac{\partial(rB_{1,2})}{\partial r}$ is described by the following relations:

$$j_1(r, t) \approx \frac{C_1}{\mu\delta}\sum_{n=0}^{\infty}\left[\frac{1}{2^{2n}(n!)^2}\left(\frac{r}{\delta}\right)^{2n}\right]\exp\left(\omega t - \frac{\pi}{2}\right), \quad (14)$$

$$j_2(r, t) \approx \frac{C_2}{\mu\delta}J_0\left(\frac{r}{\delta}\right)\exp\left(\frac{\pi}{2} - \omega t\right), \qquad (15)$$

$$j\left(r, \frac{\pi}{2\omega}\right) = \frac{1}{2}\left[j_i\left(r, \frac{\pi}{2\omega}\right) + j_2\left(r, \frac{\pi}{2\omega}\right)\right]. \quad (16)$$

Let the conductor have the radius $a_0 = 0.52$ mm and an initial conductivity of 10^5 S/m. For the frequency $\omega = 10^8$ Hz and the field amplitude $B_0 = 54$ T, the radial distributions of the magnetic induction and the current density at various moments in time are depicted in Figs. 1 and 2. The curves of magnetic induction are convex when the field increases and concave when it decreases. The current density distribution at the time $t = 12$ ns is inhomogeneous ($\delta \approx 2.8 \times 10^{-4}$ m $< a$) and then exhibits redistribution. If the external field varies so that $dB/dt \longrightarrow 0$, the current density distribution tends to homogeneous ($t = 15$ ns). When the field decreases, the current density is maximum at the center and drops in the surface layer.

A comparison of the results of approximate calculation to the numerical solution [3] showed quite good convergence. The differences are related to the fact that the numerical solution [3] was obtained for the com-

plete set of the equations of magnetohydrodynamics (with allowance for the heating and expansion of the conductor). It should be emphasized that the analytical solutions obtained previously did not describe the inverse skin effect, according to which the current in the case of $\delta \ll a$ and decreasing field passes predominantly through the central part of the cylindrical conductor.

REFERENCES

1. L. D. Landau and E. M. Lifshitz, *Course of Theoretical Physics,* Vol. 8: *Electrodynamics of Continuous Media* (Nauka, Moscow, 1982; Pergamon Press, New York, 1984).
2. N. I. Kuskova and S. I. Tkachenko, Pis'ma Zh. Tekh. Fiz. **22** (10), 30 (1996) [Tech. Phys. Lett. **22**, 401 (1996)].
3. N. I. Kuskova and S. I. Tkachenko, Pis'ma Zh. Tekh. Fiz. **28** (14), 59 (2002) [Tech. Phys. Lett. **28**, 604 (2002)].

Translated by P. Pozdeev

On the Possibility of Measuring the Anapole Moment of Potassium Atom

V. F. Ezhov, M. G. Kozlov, G. B. Krygin, V. A. Ryzhov, and V. L. Ryabov

St. Petersburg Institute of Nuclear Physics, Russian Academy of Sciences,
Gatchina, Leningrad oblast, Russia
e-mail: http://www.pnpi.spb.ru/

Abstract—We suggest measuring the nuclear-spin-dependent *P*-odd amplitude in the transitions between hyperfine structure sublevels in the ground state of potassium isotopes. Since the main contribution to this amplitude is due to the anapole moment of the nucleus, such measurements of the *P*-odd spin-dependent effects may provide new information about weak interactions. It is established that the measurement of such effects with a statistical error within 1% can be performed for approximately 1 h. © 2004 MAIK *"Nauka/Interperiodica"*.

In recent years, considerable progress has been achieved in the study of weak interactions by methods of nuclear physics [1–3] used to measure the *P*-odd *E*1 amplitude in the optical transitions of heavy atoms. A part of this amplitude that is independent of the nuclear spin and bears information about the weak charge of atomic nuclei is well studied. The measurement of this part was among the most important evidence of the existence of neutral currents. At the same time, the *P*-odd effects dependent on the nuclear spin remain virtually uninvestigated. The main contribution to the *P*-odd spin-dependent amplitude is due to the anapole moment of the nucleus. Therefore, the measurements of such effects provide new information about weak interactions in the hadronic sector. The first measurements of the spin-dependent amplitude were performed for Cs [1], where the obtained value of the anapole moment constant has proved to exceed theoretical predictions.

Flambaum and Murray [4] use the experimental data obtained in [1] for determining the *P*-odd potential constants for proton and neutron. The results significantly deviated from the corresponding values obtained from nuclear physics experiments [5]. In this context, new measurements of the *P*-odd potential constants for other atoms would be of considerable importance.

Unfortunately, practical realization of such measurements using optical transitions presents an extremely complicated problem. This is related, first, to the fact that the spin-dependent *P*-odd effect is about 100 times as small as the spin-independent one. Moreover, the hyperfine structure of the optical line is usually incompletely resolved, and the spin-dependent *P*-odd effect is manifested only by a weak distortion of the *P*-odd signal profile. Therefore, in order to extract the spin-dependent part of the weak interaction ampli-

tude from the measured signal, it is necessary to reliably determine the profile of the *P*-off spin-independent signal, which is by no means a simple task.

In the proposed experiment, we intend to measure the spin-dependent *P*-odd amplitude in the transitions between hyperfine components in the ground state of ^{41}K isotope [6, 7]. This variant offers three principal advantages over the optical experiments performed previously:

(i) The absence of the contribution to the amplitude due to the spin-independent part of the *P*-odd interaction makes the *P*-odd signal determined completely by the nuclear-spin-dependent part of the weak interaction Hamiltonian.

(ii) A record small value is achieved for the rate of spin relaxation of the polarization of atoms into cells for the transitions between hyperfine sublevels of the ground state. This provides conditions for reaching an extremely high statistical sensitivity with respect to the *P*-odd signal.

(iii) The transition frequency for the ^{41}K isotope in a strong constant magnetic field can be reduced to 60 MHz. This allows a cell with a characteristic size on the order of 3 cm to be arranged in the electric field antinode (and, accordingly, in the magnetic field node) so as to suppress the *P*-even amplitude of the magnetic dipole transition by several orders of magnitude. Moreover, it is possible to provide for an additional suppression of the background *M*1 transition in a strong magnetic field. Indeed, when the magnetic field strength varies in the range 400–4000 G, the magnetic transition amplitude changes by an order of magnitude, while the frequency and the *P*-odd amplitude remain virtually unchanged. This circumstance allows us to control the
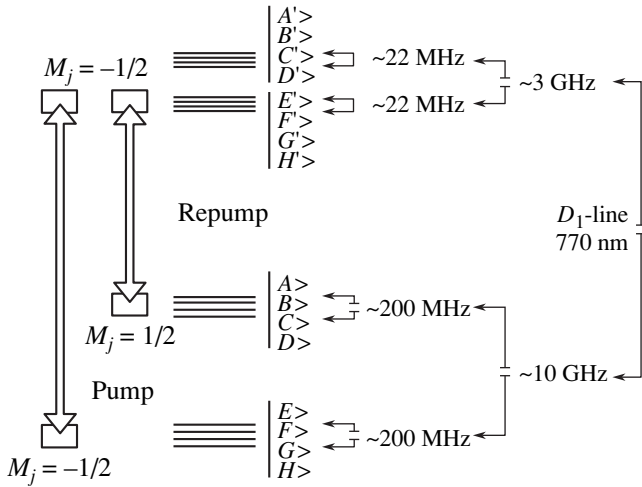
Fig. 1. Schematic diagram of optical pumping at $B_0 \sim 4000$ G.

main spurious effect related to the $M1$ transition amplitude.[1]

An additional advantage is the possibility of performing measurements for the two other potassium isotopes with nonzero nuclear spins (^{39}K, $I = 3.2$ and ^{40}K, $I = 4$). Using the results of measurements for the three isotopes (two of which are odd-proton and one of which is odd-odd), it is possible to extract information about the P-odd potential constants for proton (g_p) and neutron (g_n).

The main idea of the proposed experiment consists in measuring the interference between allowed ($M1$) and the P-odd-interaction-induced ($E1$) matrix elements in the transitions between sublevels of the hyperfine structure of the ground state of potassium atom. This experimental scheme was originally suggested for hydrogen atoms and is described in detail in [8, 9].

Let us consider the time schedule of the experiment for a three-pulse variant. Each series of measurements of the P-odd effect begins with a pulse of right-hand-polarized light propagating in the cell in the direction of the magnetic field B_0, which prepares an ensemble of potassium ions in a single quantum state $|E\rangle$ (Fig. 1). Then, the system is subjected to the action of a high-frequency (RF) magnetic field with a conditional phase of $0°$, $\boldsymbol{\beta}_1 = \beta_1\cos(\omega t)\mathbf{x}$, and a duration ($\tau_\beta$) sufficient to rotate the magnetic moment vector of the system (initially oriented by the circularly polarized light in the z-axis direction) to the xy plane. This action leads to leveling of the populations of states $|E\rangle$ and $|F\rangle$. Finally, the system is subjected to the action of an RF electric field with the phase φ, $\boldsymbol{\varepsilon}_2 = \varepsilon_2\cos(\omega t + \varphi)\mathbf{y}$ and the duration τ_ε.

Then, the RF magnetic field pulse with the duration τ_β is applied again with a conditional phase of θ, $\boldsymbol{\beta}_1 =$

---

[1] The idea of tuning the equipment in a weak field and measuring the effect in a strong field was suggested by D. Budker.

$\beta_1\cos(\omega t + \theta)\mathbf{x}$. The amplitude of the probability of finding atoms in the state $|F\rangle$ is

$$a = a_{M1} + a_{E1} + a_{M2} = \mu\beta_1\tau_\beta + d\varepsilon_2\tau_\varepsilon e^{-i\varphi} + \mu\beta_1\tau_\beta e^{-i\theta},$$

where

$$\mu \cong \mu_B \frac{\sqrt{3}\Delta E_{\text{hfs}}}{4\mu_B B_0}$$

is the amplitude of the $M1$ transition $|E\rangle \longrightarrow |F\rangle$; μ_I is the contribution due to the nuclear magnetic moment; ΔE_{hfs} is the hyperfine structure constant; $d \cong 2 \times 10^{-14} ea_0$ is the nuclear-spin-dependent P-odd-interaction-induced $E1$ transition amplitude calculated in [6]; μ_B is the Bohr magneton; e is the electron charge; and a_0 is the first Bohr orbit radius.

The population of the final state $|F\rangle$ is probed by means of optical excitation using a probing light pulse, followed by detection of the fluorescence signal whose intensity is proportional to the probability of the RF transition from the initial state $|E\rangle$,

$$S(\varphi, \theta) \propto 4(\mu\beta_1\tau_\beta)^2\cos^2(\theta/2)$$
$$+ 4(\mu\beta_1\tau_\beta)(d\varepsilon_2\tau_\varepsilon)\cos(\varphi - \theta/2)\cos(\theta/2),$$

provided that $d\varepsilon_2\tau_\varepsilon \ll \mu\beta_1\tau_\beta$. This estimate was obtained with neglect of the relaxation between sublevels of the hyperfine structure. Thus, the signal S contains the interference term proportional to the value d that is to be determined.

By changing the relative phases of the RF magnetic and electric fields (φ and θ) in the applied pulses, it is possible to separate the P-odd amplitude. For example, if the second series of measurements (following the first with a zero phase) is performed with the electric field phase changed by π, only the interference signal will be retained upon subtraction of the signals measured in these series. Such series of measurements with different relative phases of the RF fields can be periodically repeated and the signal digitized by an analog-to-digital converter and accumulated in a computer memory. As a result, the observed asymmetry of the signal is described by the expression

$$A(\varphi, \theta) = [S(\varphi, \theta) - S(\varphi + \pi, \theta)]/[S(\varphi, \theta) + S(\varphi + \pi, \theta)]$$
$$= [d\varepsilon_2\tau_\varepsilon\cos(\varphi - \theta/2)]/[\mu\beta_1\tau_\beta\cos\theta/2].$$

As can be seen from this formula, the observed value of the asymmetry depends on the selection of the phase shifts φ and θ. The time required for accumulating statistics sufficient for determining the nuclear-spin-dependent P-odd effect with an error within 1% was 1 h [7] for the following parameters: (1) optical pump-
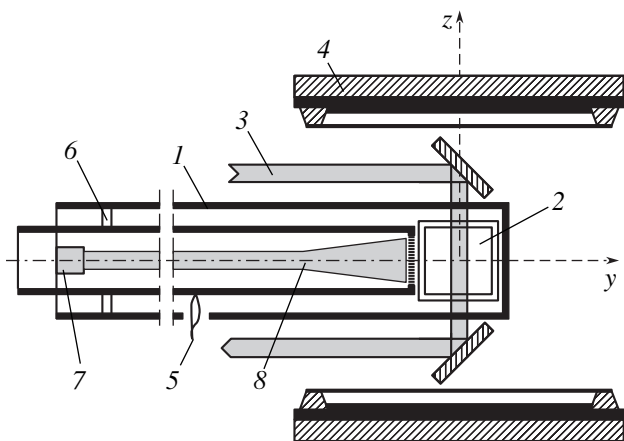
Fig. 2. Schematic diagram of the experimental setup: (*1*) λ/4 coaxial resonator; (*2*) cell with potassium vapor; (*3*) pumping and probing laser beams; (*4*) magnet pole tips; (*5*) fluorescence detector; (*6*) resonance frequency adjustment plunger; (*7*) resonator excitation inductor; (*8*) light guide. An additional set of RF rings (not depicted) applying the RF field β_1 (perpendicular to the figure plane) are arranged at the cell.

ing efficiency, 100%; (2) fluorescence detection efficiency, ~10%; (3) measurement cycle duration, ~0.1 s (for the cell with a characteristic spin relaxation time of ~1 s); (4) RF electric field amplitude, $\varepsilon_2 \sim 1$ kV/cm; (5) constant magnetic field, $B_0 \approx 4000$ G; (6) RF magnetic field amplitude, $\beta_1 \sim 10^{-2}$ G.

Figure 2 shows a schematic diagram of the experimental setup meeting all the above requirements. A cell with potassium vapor is placed in the antinode of an RF electric field in a hybrid single-mode resonator. This resonator consists of a λ/4 coaxial line and a plane-parallel capacitor at the line end. There are several obvious advantages in using such a resonator instead of a resonance circuit with lumped *LC* elements. First, the *Q* value of the proposed resonator in the frequency range of interest reaches 1000, which provides for the necessary electric field amplitude in the capacitor at a relatively small dissipated RF power (about 6 W). Second, use of the resonator eliminates the problem of parasitic capacitance, which can be comparable to the main capacitance and randomly vary in an *LC* circuit. Finally, the resonator ensures screening of the cell from external RF fields, which might introduce uncontrolled changes in the phase shifts, amplitudes, and spatial distributions of the probing RF fields applied to the cell.

The resonator end loaded with a capacitor containing the experimental cell is exposed to a constant magnetic field B_0 generated by an electromagnet and oriented parallel to the capacitor plates in the resonator (i.e., parallel to the *z* axis in Fig. 2). The RF magnetic field β_1 exciting the *M*1 transition is generated by two opposite induction coils (Fig. 2) positioned over holes in the resonator (*x* axis). The coils, coupled by a coaxial line, are elements of a low-*Q* resonance circuit with lumped elements. This ensures the equiphase character of the fields generated by the coils. This circuit and the resonator are tuned to the same frequency and excited from the same master oscillator. The low *Q* value of the circuit accounts for a small variation of the phase of the β_1 field generated by the inductance coils when the oscillator frequency deviated from the resonance value. Both induction coils are arranged in metal magnetic screens.

REFERENCES

1. C. S. Wood, S. C. Bennett, D. Cho, *et al.*, Science **275**, 1759 (1997).
2. N. H. Edwards, S. J. Phipp, P. G. E. Baird, and S. Nakayama, Phys. Rev. Lett. **74**, 2654 (1995).
3. P. A. Vetter, D. M. Meekhof, P. K. Majumder, *et al.*, Phys. Rev. Lett. **74**, 2658 (1995).
4. V. V. Flambaum and D. W. Murray, Phys. Rev. C **56**, 1641 (1997).
5. W. C. Haxton, Science **275**, 1753 (1997).
6. V. G. Gorshkov, V. F. Ezhov, M. G. Kozlov, and A. I. Mikhaĭlov, Yad. Fiz. **48**, 1363 (1988) [Sov. J. Nucl. Phys. **48**, 867 (1988)].
7. E. B. Aleksandrov, M. V. Balabas, D. Budker, *et al.*, Preprint No. 2275 (St. Petersburg Nuclear Physics Institute, 1998).
8. R. T. Robiscoe and W. L. Williams, Nucl. Instrum. Methods **197**, 567 (1982).
9. V. F. Ezhov, E. I. Zavatskiĭ, V. A. Knyaz'kov, *et al.*, Preprint No. 2356 (St. Petersburg Nuclear Physics Institute, 2000).

Translated by P. Pozdeev

Peculiarities in the Morphology of Ge Island Array on Si(100) at a Subcritical Thickness of the Deposited Ge Layer

V. G. Dubrovskiĭ[a], A. A. Tonkikh[a], G. E. Cirlin[b], V. M. Ustinov[a], and P. Werner[c]

[a] *Institute of Analytical Instrument Building, Russian Academy of Sciences, St. Petersburg, Russia*
[b] *Ioffe Physicotechnical Institute, Russian Academy of Sciences, St. Petersburg, 194021 Russia*
[c] *Max Planck Institut für Mikrostrukturphysik, Halle, Germany*
Received May 12, 2004

Abstract—Experiments revealed the formation of Ge islands on a Si(100) surface at an effective thickness of the deposited germanium layer below the critical value for the transition from two- to three-dimensional growth. The number density of Ge islands in the array was 3×10^8 cm^{-2}. The results are interpreted within the framework of a kinetic model of the island formation in heteroepitaxial systems with lattice mismatch. © 2004 MAIK "Nauka/Interperiodica".

Introduction. In recent years, peculiarities of the formation of elastically strained nanoislands during heteroepitaxy in the systems with lattice mismatch have received increasing attention. This is related to the prospects for using such island structures in modern micro- and optoelectronic devices. The system of Si/Ge materials is one of the most interesting from the standpoint of obtaining optoelectronic devices that can be directly integrated into silicon IC technology. The mechanisms of formation and the possible types of Ge islands on the surface of silicon have been studied in sufficient detail [1].

Previously, we have performed a series of experimental and theoretical investigations devoted to elucidating the mechanism of island formation in heteroepitaxial systems with lattice mismatch [2–5]. The results of experiments for the two systems, Ge/Si [3] and InAs/GaAs [4], agree well with the results of calculations performed within the framework of the kinetic theory of island formation in these systems [2]. In particular, experiments revealed the formation of InAs islands on GaAs at an effective thickness of the InAs deposit of about 1.5–1.6 monolayer (ML), which is below the critical value for the transition from two- to three-dimensional growth [5].

This Letter is devoted to peculiarities of the formation and morphology of Ge islands on the surface of silicon at a subcritical thickness of the deposited germanium layer.

Experimental. The experiments were performed on a molecular beam epitaxy (MBE) system of the SIVA 45 type (Riber, France). We have prepared two samples on identical Si(100) substrates. In sample A, a Ge layer with an effective thickness of 0.75 nm was deposited above a 100-nm-thick buffer silicon layer at a substrate temperature of 600°C. Sample B differed from sample A only by a lower effective thickness of the deposited

Ge layer, which amounted to 0.55 nm. In the course of germanium deposition, the state of the sample surface was monitored by reflection high-energy electron diffraction (RHEED). After deposition, the samples were immediately cooled down to room temperature, extracted from the MBE system, and studied in air by atomic force microscopy (AFM) in a contactless mode using a setup from Digital Instruments Inc. (USA).

Results and discussion. The experimental value of the critical thickness h_c at which the Ge/Si system at $T = 600$°C features the transition from two- to three-dimensional growth is about 0.66 nm or 4.55 ML (1 ML of Ge atoms has a height of $d_0 = 0.145$ nm) [1]. In sample A, the effective thickness of the Ge deposit exceeds h_c, and the formation of islands proceeded according to the classical Stranski–Krastanov mechanism, which was confirmed by the characteristic changes in the RHEED pattern. Figure 1 shows an AFM image of the surface of sample A. In this case, the sample surface displays the so-called dome phase [1]. The dimensions of the Ge islands in sample A were as follows: average lateral size, 73.5 nm, and average height, 10.0 nm. The number density of islands was $N = 5 \times 10^9$ cm^{-2}.

In sample B, the effective thickness of the Ge deposit was below h_c. An AFM image of the surface of sample B is presented in Fig. 2. As can be seen, there are islands on the sample surface despite the subcritical thickness of the deposit. In this case, the dimensions of the Ge islands were as follows: average lateral size, 34.5 nm, and average height, 2.9 nm. Note that the number density of islands in sample B, $N = 3.1 \times 10^8$ cm^{-2}, was significantly lower than that in sample A.

These results can be explained within the framework of a kinetic model of the island formation in heteroepitaxial systems [2–6]. Equilibrium thickness of
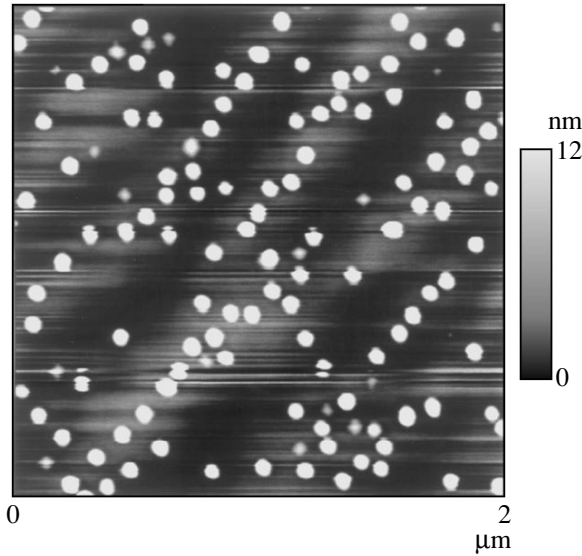
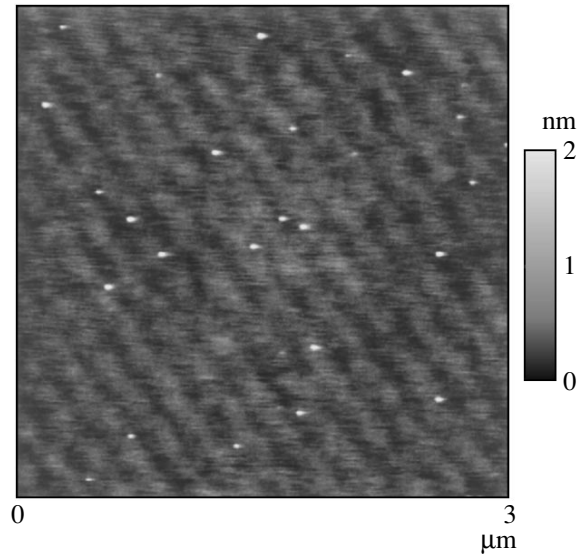**Fig. 1.** AFM image of the surface of sample A (scanned area, 2×2 μm).

Fig. 2. AFM image of the surface of sample B (scanned area, 3×3 μm).

the wetting layer h_{eq} is determined by the balance of elastic and contact (wetting) forces [7] (here and below, the layer thickness is expressed in ML units):

$$h_{eq} \cong k_0 \ln\left(\frac{\Psi_0}{d_0 \lambda \varepsilon_0^2}\right), \qquad (1)$$

where Ψ_0 is the contact energy density at the Ge–Si interface, λ is the elastic modulus of germanium, ε_0 is the lattice mismatch, k_0 is the effective range (expressed in ML units) of the potential of attraction between adatoms and substrate, which exponentially decays with the distance from the substrate. In the Ge/Si system, $\lambda = 1.27 \times 10^{12}$ dyn/cm²; $\varepsilon_0 = 0.042$; $d_0 = 0.145$ nm; and $\Psi_0 = 450$ erg/cm² [6]. For $k_0 = 1.11$, these data yield the equilibrium thickness $h_{eq} \approx 2.91$ ML. In the case of $h < h_{eq}$, the contact layer is stable, and for $h > h_{eq}$ it is metastable. The formation of islands is possible only in a metastable contact layer. The measure of "metastability" is offered by the quantity $\zeta = h/h_{eq} - 1$.

Now we will proceed with a generalization of our model [2] to the case of subcritical deposits. Since the rate of island nucleation depends very strongly on ζ, the main part of the island size distribution corresponds to $H_* \approx h_*$ and $\Phi_* \approx \zeta_*$, where H is the effective thickness of the deposit at the time t, $\Phi = H/h_{eq} - 1$ is the ideal metastability in the absence of island formation, and the asterisk denotes the values at the point of maximum metastability. The flow of substance to the substrate surface, V (expressed in ML /s) during MBE is usually constant at $t < t_0$ and zero at $t > t_0$, where t_0 is the time when the source is switched off. In this case, the time variation of Φ is described by the expression $\Phi(t) = t/t_\infty$ for $t < t_0$ and $\Phi(t) = t_0/t_\infty$ for $t > t_0$, where $t_\infty = h_{eq}/V$ is

the time of deposition of the equilibrium contact layer, $t = 0$ corresponds to $h = h_{eq}$, and $\Phi = \zeta = 0$.

Assuming that (i) all islands are initially characterized by the same ratio of the height to the lateral size, (ii) all islands have the shape of square pyramids with the base $L \times L$ and a contact angle θ, and (iii) adatoms from the contact layer enter into islands through a boundary with the perimeter $4L$, we may introduce the effective island "size" as $\rho = i^{2/3} = (L/\alpha l_0)^2$. Here, l_0 is the average distance between adatoms on the substrate surface, $\alpha = (6d_0 \cot a\, n\theta/l_0)^{1/3}$ is the geometric factor, and i is the number of atoms per nucleus. In terms of the variable ρ, the island growth rate is independent of the island size. For this reason, we may ascertain [2] that the distribution function of islands with respect to size ρ has the form $g(\rho, t) = g_s(\zeta(x))$. Here, $g_s(\zeta)$ is a stationary distribution (independent of ρ), and $x(\rho, t) = z(t) - \rho$. The function $z(t)$ is determined by the equation $dz/dt = \zeta/\tau$ (where τ is the characteristic time of island growth) with the initial condition $z(t = t_*) = 0$. By its physical meaning, $z(t)$ corresponds to the most representative size of islands nucleated at the maximum contact layer thickness.

According to the Zel'dovich formula, the stationary distribution $g_s(\zeta)$ is proportional to $\exp[-F(\zeta)]$, where $F(\zeta)$ is the activation barrier for nucleation (expressed in thermal units). The model of the free energy of nucleation developed in [2] leads to the expression [4] $F(\zeta) = T_e/T\zeta^2$, where T is the surface temperature and T_e is the quasi-equilibrium temperature determining the height of the nucleation activation barrier at a given substrate temperature and contact layer thickness. The quantity T_e is determined by the energy constants of the

heteroepitaxial system and by the island shape in the initial nucleation stage:

$$T_e = \frac{4}{27}\frac{[\sigma(\theta)/\cos\theta - \sigma(0)]^3(6\cot an\theta)^2}{k_B[(1 - Z(\theta))\lambda\varepsilon_0^2(h_{eq}/k_0)]^2}, \quad (2)$$

and where $\sigma(0)$ and $\sigma(\theta)$ are the surface energies of the deposit for the (100) base and side faces of the pyramid, respectively, and $Z(\theta)$ is the relative relaxation of elastic stresses in the island [8]. Assuming for the Ge/Si system the values $\sigma(0) \approx \sigma(\theta) = 800$ erg/cm^2 and taking the contact angle for the nucleated islands equal to $\theta = 20°$ ($Z \approx 0.6$), we obtain an estimate of $T_e \approx 6700$ K.

The extremely strong dependence of the stationary distribution on the parameter ζ allows us to use the following approximation in the region of maximum metastability [2]:

$$g(x) = g_s(\Phi_*)\exp\left[-\frac{\Gamma}{\Phi_*}(\Phi_* - \zeta(x))\right], \quad (3)$$

where $\Gamma = 2F(\Phi_*) \gg 1$ is the large parameter of the classical nucleation theory. Using the equation of mass balance on the surface in the form $\Phi = \zeta + G$ (G is the volume of islands per unit surface area divided by $d_0 h_{eq}$), we obtain

$$\Phi_* - \zeta(x) = G(x) - [\Phi(x) - \Phi_*]. \quad (4)$$

In the region of maximum metastability, the function $\Phi(x)$ can be presented in the following form:

$$\Phi(x) = \begin{cases} \Phi_* + (\Phi_*/\Gamma)cx, & x \le z_0, \\ \Phi_* + (\Phi_*/\Gamma)cz_0, & x > z_0, \end{cases} \quad (5)$$

where $z_0 = (\Gamma/c)(\Phi_0/\Phi_* - 1)$, $\Phi_0 = H_0/h_{eq} - 1$, $c = \Gamma/\Phi_*^2 Q$, and $H_0 = Vt_0$ is the amount of deposited material expressed in ML units. The value of c depends on the kinetic control parameter $Q = t_\infty/\tau \gg 1$, which is equal to the ratio of the characteristic growth time of the equilibrium contact layer to that of the islands. The quantities z_0 and Φ_0 depend on the amount of deposited material (H_0): the case of $H_0 > h_c$ corresponds to a supercritical deposit, while $H_0 < h_c$ represents the subcritical case.

Analytical description of the nucleation stage requires using an expression for the island volume in terms of the variables z and x:

$$G(z) = \frac{l_0^2}{h_{eq}}\int_{-\infty}^{z} dx(z - x)^{3/2}g(x). \quad (6)$$

Evidently, the surface number density N of islands is determined as

$$N = \int_{-\infty}^{\infty} dx g(x). \quad (7)$$

Subsequent calculations are analogous to those described elsewhere [2]. Expression (5) is substituted into Eq. (4), and the result is substituted into formula (3) and then into formula (6). This eventually leads to a self-consistent integral equation for $G(z)$, which is solved by iterations. The result obtained in the first approximation for G is substituted into formula (3), which gives the island size distribution function. Integrating this function with respect to x in accordance with formula (7) yields an expression for the number density of islands. In order to determine the values of characteristics at the point of maximum metastability for a supercritical deposit, we notice that, for $H_0 \ge h_c$, $d\zeta/dz(z = 0) = 0$, and, hence, $dG/dz(z = 0) = d\Phi/dz(z = 0) = (\Phi_c/\Gamma)c$. This yields a relation between the quantities $F(\Phi_c)$ and Q (which appears to be $F(\Phi_c) = (5/2)\ln Q$ [2]) and gives the value of the normalization factor $g_s(\Phi_*)$ in formula (3). The expression for the critical deposit thickness is as follows:

$$h_c = h_{eq}\left[1 + \left(\frac{2}{5}\frac{T_e}{T\ln Q}\right)^{1/2}\right]. \quad (8)$$

Thus, our model predicts a weak logarithmic dependence of the critical thickness on the material flux [9]. Since h_c can be determined with high accuracy by RHEED, we can determine the parameter Q from relation (8), provided that h_{eq}, T_e, and T are known. For example, in the case of heteroepitaxy in the Ge/Si(100) system under consideration, we have $h_{eq} = 2.91$ ML, $h_c = 4.55$ ML, $T_e = 6700$ K, and $T = 600$ K, which yields $Q \approx 1.56 \times 10^4$.

The final expression for the number density of islands in the array is as follows:

$$N = N_{max}\begin{cases} \varphi^{-3}[1 - e^{-f} + fU(f)], & H_0 \le h_c, \\ 1 - e^{-f} + fU(f), & H_0 > h_c, \end{cases} \quad (9)$$

where $\varphi = \Phi_0/\Phi_c = (H_0 - h_{eq})/(H_c - h_{eq})$,

$$f(\varphi) = \begin{cases} \varphi^7\exp[F_c(1 - 1/\varphi^2)], & H_0 \le h_c, \\ \exp[2F_c(\varphi - 1)], & H_0 > h_c, \end{cases} \quad (10)$$

$F_c = F(\Phi_c)$, and the function $U(f)$ is defined as

$$U(f)$$
$$= \int_0^\infty d\xi\exp\left[-f\left(\frac{4}{3\sqrt{\pi}}e^\xi\int_\xi^\infty dy y^{3/2}e^{-y} + \frac{8}{15\sqrt{\pi}}\xi^{5/2}\right)\right]. \quad (11)$$

The maximum number density of islands achieved for supercritical deposits is defined as [2]

$$N_{max} = \frac{4}{l_0^2}h_{eq}\frac{T}{T_e}\left(\frac{\ln Q}{Q}\right)^{3/2}. \quad (12)$$

Figure 3 shows the plot of the number density N of germanium islands in the array on silicon versus the
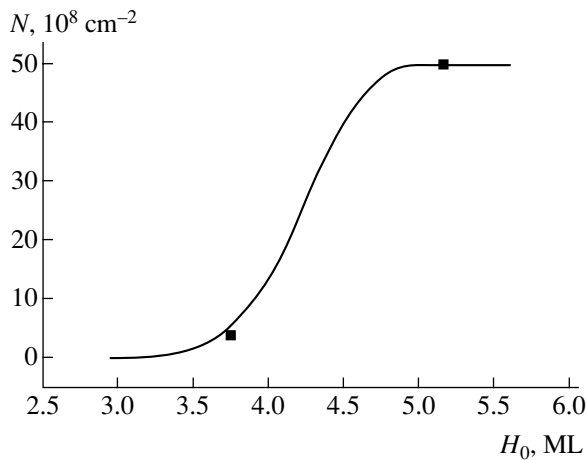
N, 10^8 cm^{-2}

Fig. 3. Calculated plot of the number density N of islands in the array versus the amount H_0 of Ge deposited onto Si. Black squares show the results of measurements for samples A and B.

amount H_0 of deposited germanium, which was calculated using Eqs. (9)–(12) for the parameters of the Gs/Si(100) system at $T = 600°C$. As can be seen, the number density of islands increases with the amount of deposited germanium and exhibits saturation in the supercritical region on a level of $N_{max} = 4.96 \times 10^9$ cm^{-2} (for $l_0 = 0.395$ nm) determined by formula (12). The calculated values of the number density at $H_0 = 0.55$ and 0.75 nm (3.79 and 5.17 ML) fit quite well to the experimental values obtained in this study.

To summarize, we have experimentally established the possibility of island formation in the GeSi(100) system at an effective thickness of the deposited germanium layer below the critical value for the transition from two- to three-dimensional growth. The observed effect was explained within the framework of the kinetic model of island formation in heteroepitaxial systems with lattice mismatch.

REFERENCES

1. O. P. Pchelyakov, Yu. B. Bolkhovityanov, A. V. Dvurechenskiĭ, *et al.*, Fiz. Tekh. Poluprovodn. (St. Petersburg) **34**, 1281 (2000) [Semiconductors **34**, 1229 (2000)].
2. V. G. Dubrovskii, G. E. Cirlin, and V. M. Ustinov, Phys. Rev. B **68**, 075409 (2003).
3. A. A. Tonkikh, V. G. Dubrovskii, G. E. Cirlin, *et al.*, Phys. Status Solidi B **236**, R1 (2003).
4. V. G. Dubrovskiĭ, Yu. G. Musikhin, G. É. Tsyrlin, *et al.*, Fiz. Tekh. Poluprovodn. (St. Petersburg) **38**, 342 (2004) [Semiconductors **38**, 329 (2004)].
5. A. A. Tonkikh, G. É. Tsyrlin, V. G. Dubrovskiĭ, *et al.*, Pis'ma Zh. Tekh. Fiz. **29** (16), 72 (2003) [Tech. Phys. Lett. **29**, 691 (2003)].
6. A. V. Osipov, F. Schmitt, S. A. Kukushkin, and P. Hess, Appl. Surf. Sci. **188**, 156 (2002).
7. P. Müller and R. Kern, Appl. Surf. Sci. **102**, 6 (1996).
8. C. Ratsch and A. Zangwill, Surf. Sci. **293**, 123 (1993).
9. I. Daruka and A.-L. Barabasi, Phys. Rev. Lett. **79**, 3708 (1997).

Translated by P. Pozdeev

A New High-T_C Ferromagnet: Manganese-Doped CdGeAs$_2$ Chalcopyrite

R. V. Demin[a], L. I. Koroleva[a,*], S. F. Marenkin[b,], S. G. Mikhaĭlov[b],**
V. M. Novotortsev[b], V. T. Kalinnikov[b], T. G. Aminov[b], R. Szymczak[c,*],**
H. Szymczak[c], and M. Baran[c]

[a] *Moscow State University, Moscow, 119899 Russia*
[b] *Kurnakov Institute of General and Inorganic Chemistry, Russian Academy of Sciences, Moscow, 117907 Russia*
[c] *Institute of Physics, Polish Academy of Sciences, 02668 Warsaw, Poland*
*e-mail: * koroleva@ofef343.phys.msu.ru; ** marenkin@rambler.ru; *** szymr@ifpan.edu.pl*
Received May 31, 2004

Abstract—New ferromagnets with high Curie temperatures, reaching 355 K, have been obtained by doping a GdGeAs$_2$ semiconductor compound with manganese. The obtained compounds are magnetically inhomogeneous, comprising a mixture of ferromagnetic (FM) and paramagnetic phases. The volume fraction of the FM phase increases with the degree of doping. The development of ferromagnetism in this system is probably related to the presence of vacancies of the (Cd, V_C, Mn)GeAs$_2$ type or to a nonstoichiometry of the (Cd, Ge, Mn)GeAs$_2$ type, since theoretical estimates show that the FM state is energetically more favorable than the spin glass state only in these cases. © *2004 MAIK "Nauka/Interperiodica".*

In recent years, much attention has been devoted to the investigation of dilute magnetic semiconductors, which are promising materials for devices simultaneously employing both the magnetic and semiconductor properties [1, 2]. The most thoroughly studied system is GaAs:Mn, in which the Curie temperature (T_C) does not exceed 110 K. However, applications in spintronics require ferromagnetic (FM) semiconductors with $T_C > 300$ K. Recently, such high-T_C ferromagnets were found among manganese-doped chalcopyrites CdGeP$_2$:Mn, ZnGeP$_2$:Mn [3–5] and ZnSnAs$_2$:Mn [6], in which the T_C values fall significantly above room temperature.

This paper reports on a new manganese-doped chalcopyrite, CdGeAs$_2$:Mn, which has a Curie temperature as high as $T_C = 355$ K.

A single crystal of CdGeAs$_2$ containing 0.5 mass % Mn was grown using a vertical variant of the Bridgman method. Polycrystalline samples were obtained by solid state reactions. According to the X-ray diffraction data, all samples had a single-phase structure of chalcopyrite. The magnetization measurements were performed using a SQUID magnetometer. The electric resistance was measured by the conventional four-point-probe technique. The paramagnetic (PM) susceptibility was measured by the weighing technique with electromagnetic compensation.

Figure 1 presents the plots of magnetization *M* versus temperature *T* for all samples measured in a magnetic field of 5 T. Figure 2 shows the *M*(*T*) curves for a polycrystalline sample with 3 mass % Mn measured in the course of cooling from 370 to 5 K in a magnetic field of 100 Oe (curve *1*) and in the course of heating from 5 to 370 K in the same magnetic field after preliminary cooling in a zero field (curve *2*). The magnetization isotherms at $T > T_C$ are nonlinear and exhibit no
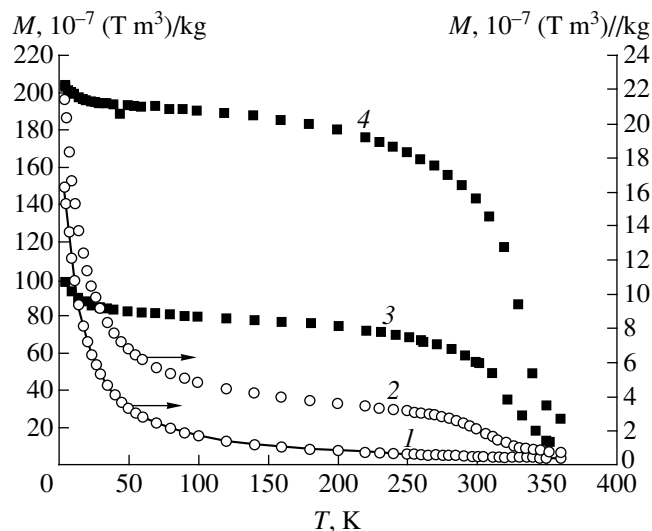

Fig. 1. Temperature dependences of the magnetization *M*(*T*) of CdGeP$_2$:Mn samples measured in a magnetic field of 5 T: (*1*) single crystal containing 0.5 mass % Mn; (*2–4*) polycrystalline samples containing 1, 3 and 6 mass % Mn, respectively.

saturation up to the maximum values of applied magnetic field (5 T) used in this study. The coercivity of polycrystalline samples was small (not exceeding 0.004 T), which was evidence of a low magnetocrystalline anisotropy.

For the single crystal doped with 0.5 mass % Mn, the experimental $M(T)$ curve measured in a field of 5 T was well approximated by the Langevin function for a system of noninteracting magnetic moments with $\mu = 7.1\ \mu_B$. This is illustrated in Fig. 1, which shows how the calculated $M(T)$ curve (solid curve *1*) fits to the experimental points. In polycrystalline samples, the temperature dependence of the magnetization was more complicated than in the single crystal. At $T > 80$ K, the behavior of $M(T)$ in polycrystalline samples was characteristic of a ferromagnet, but at $T < 80$ K, the magnetization M sharply increased with decreasing temperature, and the shape of the $M(T)$ curves was like that for the single crystal.

The behavior of the magnetization of polycrystalline samples suggests that manganese ions are inhomogeneously distributed: one part of the sample occurs in the FM state with a specific magnetization of M_1, and the other part occurs in a nearly PM state with the magnetization M_2, so that $M = M_1 + M_2$, where $M_1 > M_2$ at $T > 80$ K and $M_1 < M_2$ at $T < 80$ K. By extrapolating the straight portions of the $M(T)$ curves from the region of $T > 100$ K to their intersection with the M axis, we approximately estimated M_1 for 5 K $\leq T \leq 100$ K and then determined $M_2 = M - M_1$. It was found that $M_2(T)$ for the FM phase of polycrystalline samples is well approximated by the Langevin function for the magnetic moments $\mu = (7.4–8)\ \mu_B$ (see table), which is close to the value ($\mu = 7.1\ \mu_B$) determined for the single crystal. In the pure PM state, the maximum magnetic moment μ would correspond to $5\ \mu_B$ per Mn ion. The difference from the experimental values of $\mu = (7.4–8)\ \mu_B$ can be explained assuming that, in addition to the noninteracting molecules with manganese ions, there exist clusters involving several interacting molecules. The magnetization M_1 in polycrystalline samples accounts for about 12, 76, and 91% of the total magnetization for the compounds containing 1, 3, and 6 mass % Mn, respectively. It is the presence of an "almost-PM" part that accounts for the observed difference between $M(T)$ curves of a sample cooled to 5 K in a weak magnetic field (0.01 T) and a zero-field-cooled sample heated in the same field (Fig. 2).

The Curie temperature of such samples with a two-phase magnetic structure is essentially the T_C value of the FM part. Since the samples are magnetically inhomogeneous, their Curie temperatures cannot be determined by fitting the $M(T)$ curves to the Brillouin function or by using the Belov–Arrott method of thermodynamic coefficients. We determined the T_C values by extrapolating the steepest part of the $M(T)$ curve to its intersection with the T axis (the same method was used
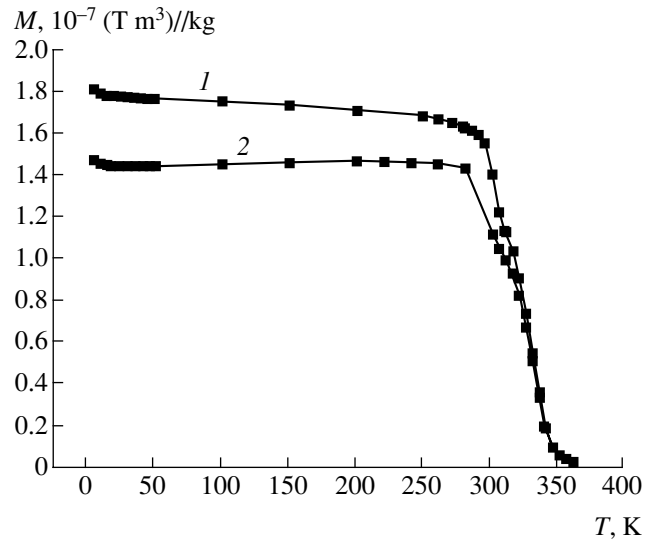
M, 10^{-7} (T m^3)//kg

Fig. 2. Temperature dependences of the magnetization of a polycrystalline CdGeAs$_2$:Mn sample measured in a magnetic field of 100 Oe: (*1*) in the cooling mode; (*2*) in the heating mode after zero-field cooling from 370 to 5 K.

in [4, 5]). The obtained values of T_C are presented in the table. The method used for determining T_C is quite well justified, since the contribution of M_2 to the total moment M in the region of T_C for the samples containing 3 and 6 mass % Mn is virtually independent of the temperature and is about two orders of magnitude smaller than the contribution due to M_1. This is clearly demonstrated by the comparison of the $M(T)$ curve for the single crystal containing 0.5 mass % Mn (described by the Langevin function) and the curves for the polycrystalline samples. Although the magnetic moments μ in both cases are approximately the same, the value of M_2 for the polycrystalline samples at each temperature is smaller than M of the single crystal because the volume of the "almost-PM" part is smaller than that of the FM part. The PM susceptibility in polycrystalline samples obeys the Curie–Weiss law with the values of paramagnetic Curie points θ given in the table. The values of θ and T_C are close, which is characteristic of ferromagnets.

Magnetic and electric characteristics of CdGeAs$_2$:Mn

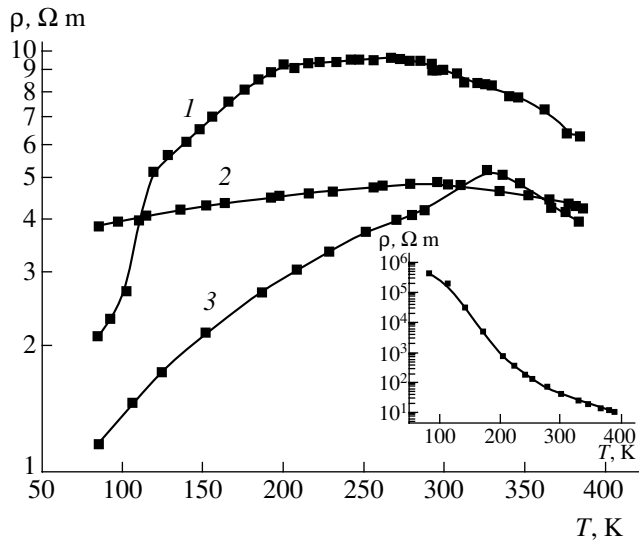| Sample	T_C, K	θ, K	μ, μ_B	$T_{\rho\ max}$, K
Single crystal with 0.5 mass % Mn			7.1	
Polycrystal with 1 mass % Mn	350	301	7.4	276
Polycrystal with 3 mass % Mn	355	329	8.0	324
Polycrystal with 6 mass % Mn	355	321	8.0	291

Fig. 3. Temperature dependences of the electric resistivity ρ of (*1–3*) polycrystalline $CdGeP_2$:Mn samples containing 1, 3 and 6 mass % Mn, respectively. The inset shows the $\rho(T)$ curve of the single crystal sample containing 0.5 mass % Mn.

Figure 3 shows the temperature dependences of the resistivity ρ for all $CdGeAs_2$:Mn samples studied. As can be seen, the $\rho(T)$ curve of the single crystal (see the inset in Fig. 3) has the shape typical of a nondegenerate semiconductor. In polycrystalline samples, the $\rho(T)$ curves exhibit maxima at $T = T_{\rho\,max} \le T_C$ ($T_{\rho\,max}$ values are given in the table). The conductivity of these samples has a semiconductor character at $T > T_{\rho\,max}$ and a metallic character at $T < T_{\rho\,max}$. In all samples, the magnetoresistance is absent (to within the experimental accuracy of 0.01%) in the entire range of temperatures from 80 to 400 K. Determination of the type of charge carriers from the sign of the thermopower at 300 K showed that all samples, except for the composition with 6 mass % Mn, exhibit hole conductivity, while the latter sample has electron conductivity.

Recently, Akai *et al.* [7, 8] studied the nature of ferromagnetism in dilute magnetic semiconductors by means of *ab initio* calculations of their electron structure. In these systems, the effective exchange interaction is determined for the most part by competition between the double exchange and superexchange interactions. If Cd^{2+} ions in $A^{II}B^{IV}C_2^{V}$ are replaced by Mn^{2+} ions, the superexchange prevails and the ground state corresponds to the spin glass [9]. When Ge^{4+} ions are replaced by Mn^{3+} ions (which are acceptors in the case under consideration), the system exhibits ferromagnetism due to the double exchange mediated by holes. However, calculations of the system formation energy showed that the FM state is energetically unfavorable. For the $CdGeP_2$:Mn system, it was found [10] that the presence of vacancies of the $(Cd, V_C, Mn)GeP_2$ type or a nonstoichiometry of the $(Cd, Ge, Mn)GeP_2$ type makes the FM state energetically more favorable than the spin glass state. Apparently, the same considerations can be used to explain the FM state and the high conductivity of the hole type in polycrystalline $CdGeP_2$:Mn samples containing 1 and 3 mass % Mn. In the system with 6 mass % Mn, which exhibits electron conductivity, a portion of the Mn atoms probably occurs at interstitials.

REFERENCES

1. H. Ohno, Science **281**, 951 (1998).
2. G. A. Prinz, Science **282**, 1660 (1998).
3. G. A. Medvedkin, T. Ishibashi, T. Nishi, *et al.*, Jpn. J. Appl. Phys. **39**, L949 (2000).
4. G. A. Medvedkin, K. Hirose, T. Ishibashi, *et al.*, J. Cryst. Growth **236**, 609 (2002).
5. K. Sato, G. A. Medvedkin, T. Nishi, *et al.*, J. Appl. Phys. **89**, 7027 (2001).
6. S. Choi, G.-B. Cha, S. C. Hong, *et al.*, Solid State Commun. **122**, 165 (2002).
7. H. Akai, Phys. Rev. Lett. **81**, 3002 (1998).
8. H. Akai, T. Kamatani, and S. Watanabe, J. Phys. Soc. Jpn **69** (Suppl. A), 112 (2000).
9. Y.-J. Zhao, W. T. Geng, A. J. Freeman, and T. Oguchi, Phys. Rev. B **63**, 201202(R) (2001).
10. K. Sato, G. A. Medvedkin, T. Ishibashi, *et al.*, J. Phys. Chem. Sol. **64**, 1461 (2003).

Translated by P. Pozdeev

Application of Holographic Interferometry to Optical Monitoring of Solid Surfaces

G. N. Zhizhin, A. K. Nikitin*, T. A. Ryzhova, and A. P. Loginov

Scientific-Technological Center for Unique Instrument Building, Russian Academy of Sciences, Moscow, Russia
Russian University of Peoples' Friendship, Moscow, Russia
* e-mail: alnikitin@sci.pfu.edu.ru
Received April 26, 2004

Abstract—A new optical method is proposed for probing transition layers on solid surfaces, which combines the high precision inherent in holographic interferometry and the high sensitivity characteristic of optical microscopy using surface electromagnetic waves. The proposed technique has been numerically modeled for monochromatic radiation in the visible spectral range. © 2004 MAIK "Nauka/Interperiodica".

Introduction. Holographic interferometry is widely used for the investigation of rapid processes in bulk samples [1]. The main advantage of this method in comparison to classical interferometry is the completely differential character of the recording of the wave front distortions. This feature is related to the fact that the classical method is based on the interference of spatially separated light waves existing at the same instant of time, while the holographic technique employs the interference of waves traveling over the same path in different periods of time. Owing to this circumstance, holographic interferometry detects only the wave front distortions caused by the introduction of an investigated object in the path of the wave, while the distortions introduced by elements of the interferometer circuit or by the viewports are not reflected by the differential interferogram, since these distortions are present in both interfering light waves. Using the differential character of the holographic interferometry, it is possible to increase the accuracy of measurements and to reduce the level of requirements of the quality of optical elements and their stability in the course of experiments.

The aim of holographic interferometry measurements usually consists in obtaining information about small variations of the volumetric properties of an object. This information is contained in the interference pattern superimposed on the virtual image of the object formed by the scene wave. Visual observation of the interference patterns restricts the accuracy of such measurements to half of the bandwidth, while photographic registration improves this parameter five to ten times.

There were attempts to apply holographic interferometry to the study of microscopic deformations in solids and physicochemical processes on solid surfaces [2, 3]. However, it was established that the precision of holographic measurements is insufficient for unambiguous interpretation of the results for systems involving transition layers formed on the sample surface.

In this paper, we suggest a new technique for the holographic interferometry of transition layers on solid surfaces, which is based on the excitation of surface electromagnetic waves (SEWs) on the probed surface area [4]. Using the proposed method, it is possible to increase the accuracy of the measurements, since the high precision inherent in holographic interferometry is combined with the high sensitivity characteristic of the SEW microscopy [5, 6].

Peculiarities of the photon excitation and detection of SEWs and the use of SEWs in optical microscopy. A SEW represents coupled formation of a wave of free charges on a solid surface with negative real part of the permittivity and an inhomogeneous *p*-polarized electromagnetic wave. The SEW field exponentially decays with the distance on both sides of the surface and in the lateral direction of wave propagation. SEWs are analogous to the Zennecke–Zommerfeld waves in the radio wave range and to Fano modes in the IR range.

The phase velocity of SEWs is lower than the velocity of light in the surrounding medium. For this reason, the photon excitation of these waves in microscopy applications is performed in the attenuated total reflectance (ATR) mode. The excitation of SEWs is accompanied by an increase in the incident wave field intensity (two to three orders of magnitude) and has a resonance character because the sample surface plays the role of an open resonator. Since the main part of the energy of the SEW field is transferred in a near-surface region, the characteristics of these waves (propagation range, phase velocity, field distribution) are determined by the properties of the sample surface and a transition layer. Information about the characteristics of SEWs and, hence, about the probed surface, is contained in the reflected radiation. This makes possible the use of
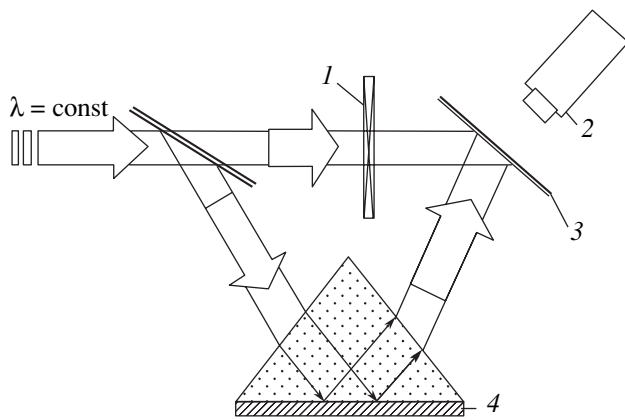
Fig. 1. Schematic diagram of the SEW-phase microscope: (*1*) controlled attenuator; (*2*) microscope; (*3*) screen; (*4*) sample.

SEWs (called surface plasmons in the case of conducting samples) in all the main optometric techniques [6].

Along with enhancement of the incident wave field, the excitation of SEWs is accompanied by a decrease in the intensity and a jumplike change in the phase of the reflected radiation [4–6]. For this reason, the main methods used to detect the excited SEWs in the reflected radiation are the amplitude and phase techniques.

SEWs have been also effectively used for increasing the sensitivity and vertical resolution of optical microscopy (holographic interferometry is in fact a kind of optical microscopy) [7]. A number of optical microscopy techniques have been developed that employ the SEWs excited by probing radiation on the sample surface [6]. The names of these techniques usually correspond to the characteristics of reflected radiation used for detecting SEWs.

In the amplitude mode suggested in 1987 by Yeatman and Ash [8], the surface inhomogeneities are detected using variations in the reflected radiation intensity cased by differences in the efficiency of SEW excitation on the clean and contaminated regions of the sample.

In the phase mode of SEW microscopy proposed in 1991 [9], the surface inhomogeneities are detected using variations in the phase of the reflected beam. In this case, the surface inhomogeneities are manifested by curved bands in the interference pattern formed with the aid of a usual optical microscope on a screen and observed in the region of intersection of the reference and reflected beams (Fig. 1). The idea of SEW-phase microscopy was used for the development of extremely sensitive optical sensors for external actions [10].

The ellipsometric mode [11] employs variations in both intensity and phase of the reflected *p*-polarized radiation, which provides more complete information about the distribution of inhomogeneities on the sample surface.

The above modes of SEW microscopy are characterized by high vertical resolution (up to fractions of a nanometer) and high sensitivity to external factors, but the accuracy of measurements is insufficiently high. This is related for the most part to a difference of the trajectories of rays in the scene beam reflected from the standard and probed regions of the sample surface. As a result, the inhomogeneities and variations of the parameters of the measuring device reduce the quality of the image.

SEW in holographic interferometry. Obviously, the resonance excitation of SEWs accompanied by considerable enhancement of the incident wave field could not escape the notice of the specialists in holography, since these features of SEWs can be effectively used in both writing and reading holograms. In 1969, shortly after the first experiments with the excitation and detection of SEWs, Bryngdahl [12] suggested several schemes for writing holographic images using SEWs excited by the reference or scene beams. Using these schemes, it is possible to obtain three-dimensional interferograms in a layer of photoresist deposited above a transparent metal film on a flat glass plate. While writing a hologram, the entire free surface of the plate is brought into optical contact (via an immersion liquid) with an ATR prism through which SEWs are excited in the metal film by one (reference or scene) of the light beams. The use of SEWs in writing and reading holograms offers the following advantages [12]: (i) it is possible to obtain very thin flat holograms with a thickness determined by the SEW penetration depth in the photoresist (~1 μm); (ii) the resonance character of the SEW excitation (with respect to the incidence angle θ and the radiation frequency ω) allows reading to be performed by white light, whereby the required θ and ω are automatically selected; (iii) the image can also be reconstructed using a monochromatic light with arbitrary ω, by selecting an appropriate θ value that ensures the excitation of SEWs in the metal film under photoresist.

The ideas of applying SEWs to holography were continuously developed [13, 14], and preference was given to using SEWs in the stage of image reconstruction, which provides for the following positive effects: (i) the reconstructing beam used to excite SEWs exhibits total internal reflectance from the prism base and, hence, creates no background interference for an observer monitoring the system from the other side of the prism; (ii) the image brightness and contrast are markedly improved due to an increase in the diffraction efficiency; (iii) this approach can be used for obtaining flat holographic screens using SEWs excited by TM modes of a planar metal–clad dielectric optical waveguide.

Our new proposal consists in using holographic interferometry for the investigation of transition layers on solid surfaces by exciting SEWs on the sample surface by the scene beam in the stage of hologram writing. However, not one of the schemes suggested previ-
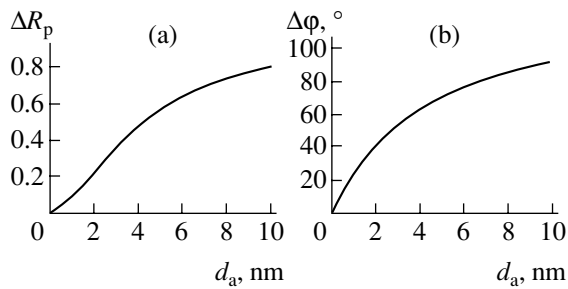
Fig. 2. Calculated curves of the (a) ΔR_p and (b) $\Delta\varphi$ versus thickness d_a of a LiF layer on a 45.5-nm-thick copper film, in which SEWs are excited by radiation with $\lambda = 632.8$ nm via an ATR prism with $n_p = 1.51$.

ously [12] is suited for this purpose. The problem consists in that both the layer to be studied and the photoresist film have to occur on the same side of the sample surface. However, when photoresist is applied onto the sample (metal film), it blocks access to the surface. Should photoresist be applied onto the film after the transition layer formation, none of the existing holographic interferometry schemes—neither the real time (RT) technique nor the double exposure (DE) method—can be realized. Therefore, in order to study the transition layer by holographic interferometry, SEWs should be involved in the formation of holograms implicitly, being excited by the scene beam, rather than directly. In this case, a hologram is written essentially in the scheme of SEW-phase microscopy (Fig. 1), in which the holographic plate is used instead of the screen. The recorded hologram can be reconstructed using either SEWs or a bulk wave.

Using the proposed method for writing the hologram of a transition layer, it is possible to compare the interferograms measured in various stages of a process on the sample surface in the RT or DE modes. The new method combines advantages of both SEW microscopy (high sensitivity and vertical resolution) and holographic interferometry (completely differential character of writing wave-front distortions and a fundamentally new level of studying dynamic processes using the RT and DE techniques).

As an example, let us consider the possibility of studying inhomogeneities in a LiF layer (with $n_a = 1.3$) on the surface of a copper film ($n_f = 0.145$, $k_f = 3.50$) by means of the proposed method using an ATR prism with $n_p = 1.51$ and radiation with $\lambda = 632.8$ nm for the SEW excitation in the sample structure. Figure 2 shows calculated curves of the increments in the reflectance (ΔR_p) and phase ($\Delta\varphi$) of the p-polarized component versus thickness d_a of the LiF layer. The calculations

were performed for the copper film thickness $d = 45.5$ nm and the incidence angle $\theta = 44°09'$. Taking into account the measurement accuracy for R_p (to within 1%) and $\Delta\varphi$ (to within 10^{-2} rad), we may conclude from the curves of $\Delta R_p(d_a)$ and $\Delta\varphi(d_a)$ in Fig. 2 that the method of holographic interferometry with SEW excitation by the scene beam provides the detection and identification of variations below 1 nm in the LiF layer thickness. According to [7], the sensitivity of ΔR_p and $\Delta\varphi$ response to the variations in d_a can be controlled by changing the incidence angle θ or the efficiency of SEW excitation in the stage of hologram writing.

Conclusions. We have proposed a new optical method for probing transition layers on solid surfaces by means of SEWs, which combines the advantages of both holographic interferometry and SEW microscopy. The new method has especially good prospects for investigations of the dynamic processes in transition layers on solid surfaces.

REFERENCES

1. C. M. Vest, *Holographic Interferometry* (Wiley, New York, 1979; Mir, Moscow, 1982).
2. R. A. Ashton, D. Slovin, and H. J. Gerritsen, Appl. Opt. **10**, 440 (1971).
3. K. N. Petrov and Yu. P. Presnyakov, Opt. Spektrosk. **44**, 309 (1978) [Opt. Spectrosc. **44**, 179 (1978)].
4. *Surface Polaritons*, Ed. by V. M. Agranovich and D. L. Mills (North-Holland, Amsterdam, 1982; Nauka, Moscow, 1985).
5. M. N. Libenson and I. A. Didenko, Opt. Vestn., No. 5–6, 1 (1992).
6. A. K. Nikitin, Doctoral Dissertation (Scientific-Technological Center for Unique Instrument Building, Russian Academy of Sciences, Moscow, 2002).
7. A. K. Nikitin and T. A. Ryzhova, Pis'ma Zh. Tekh. Fiz. **22** (9), 14 (1996) [Tech. Phys. Lett. **22**, 347 (1996)].
8. E. M. Yeatman and E. A. Ash, Electron. Lett. **23**, 1091 (1987).
9. A. K. Nikitin and A. A. Tishchenko, Pis'ma Zh. Tekh. Fiz. **17** (11), 76 (1991) [Sov. Tech. Phys. Lett. **17**, 418 (1991)].
10. A. V. Kabashin and P. I. Nikitin, Kvantovaya Élektron. (Moscow) **24**, 671 (1997).
11. A. K. Nikitin, Opt. Zh. **65** (11), 99 (1998).
12. O. Bryngdahl, J. Opt. Soc. Am. **59**, 1645 (1969).
13. J. J. Cowan, Opt. Commun. **12**, 373 (1974).
14. S. Maruo, O. Nakamura, and S. Kawata, Appl. Opt. **36**, 2343 (1997).

Translated by P. Pozdeev

Conductivity and the Hall Coefficient
of Nanostructured Titanium Nitride Films

R. A. Andrievski[a],*, Z. M. Dashevsky[b],**, and G. V. Kalinnikov[a]

*[a] Institute of Chemical Physics Problems, Russian Academy of Sciences,
Chernogolovka, Moscow oblast, 142432 Russia*
[b] Ben-Gurion University of Negev, 84105 Beer-Sheva, Israel
e-mail: *ara@icp.ac.ru; **zdashev@bgumail.ac.il
Received May 12, 2004

Abstract—The conductivity and the Hall coefficient of nanostructured TiN films synthesized by nonreactive RF magnetron sputtering have been experimentally studied. The mechanism of conductivity and the role of grain size are discussed. © *2004 MAIK "Nauka/Interperiodica".*

The results of investigations of the transfer phenomena in nanostructured films of titanium nitride (TiN) have been reported, for example, in [1–5]. However, to our knowledge, data on the effect of grain size on the galvanomagnetic properties of such films were only reported in [1] for multilayer TiN/VN epitaxial film structures (superlattices) with layer thicknesses δ in the range from 0.5 to 6 nm ($\delta_{TiN} = \delta_{VN}$). It was therefore of interest to study the role of grain size L in single-layer TiN films.

Titanium nitride films with a thickness of about 1 μm were obtained using a method described previously [4] based on the nonreactive RF magnetron sputtering of sintered powder targets with a diameter of 80 mm and a thickness of ~8 mm at a power of $N = 0.7$ kW. The samples were prepared at an argon pressure of 0.4 Pa and a substrate temperature of 150°C. The films were deposited onto silicon (for the measurement of electrical and galvanomagnetic properties) and stainless steel (for the transmission electron microscopy investigation) substrates.

The grain size in the deposit was controlled by applying an external magnetic field ($H = 400$ Oe), which was previously [6] shown to decrease both the average grain size and its mean square deviation (i.e., the width of the grain size distribution). The grain size distributions were constructed using the results of analysis of the dark-field electron microscopic images obtained using a Jeol 200CX electron microscope and processed using the special computer program packages Image-Pro Express 4.0 and Statistica. Each distribution was obtained using a data array for 1000–1500 grains. In order to avoid errors during the image analysis, the measurements were started with a minimum grain size of about 1 nm. The sample surface topography was studied using a Nanoscope IIIa atomic force microscope (AFM). The AFM images presented in Fig. 1 clearly illustrate the difference in microstructure and surface roughness of two TiN films with the average grain size L (by electron-microscopic data) 29.0 ± 15.0 nm for film I (deposited without applied magnetic field) and 8.8 ± 2.2 nm for film II (deposited in the magnetic field).

According to the X-ray diffraction and electron microdiffraction data, the films were single-phase and possessed a face-centered cubic structure of the NaCl type (with $a = 0.4292$ nm) typical of TiN. The results of analyses by means of Auger electron spectroscopy (AES) and energy-dispersive X-ray spectroscopy (EDX) showed quite uniform distribution of elements in depth of the films. The films were also analyzed for the content of oxygen and carbon impurities. Taking into account the single-phase structure and assuming that both oxygen and carbon atoms occupy lattice sites in the nitrogen sublattice of TiN, the general empirical formula of the deposited compound according to the AES data can be written as $Ti(N_{0.6}O_{0.2}C_{0.2})_{1.58}$ [5], which implies that the sample films were superstoichiometric. The electric resistance of the films on silicon substrates was measured by the conventional four-point-probe technique in the range of temperatures from 85 to 300 K. The Hall effect measurements were performed in a field of 1 T at room temperature.

Table 1 summarizes the main results of measurements, including the charge carrier density n and the mobility μ (estimated from the well-known relations valid in the single-band approximation $R_H = -1/en$ and $\sigma = en\mu$, where R_H is the Hall coefficient, σ is the conductivity, and e is the electron charge) and the conductivity activation energy Q determined from the temperature dependence of σ (Fig. 2). For comparison, Table 2 gives data for some other titanium nitride samples reported in the literature [1, 7, 8].

An analysis of the data presented in Tables 1 and 2 leads to the following conclusions:
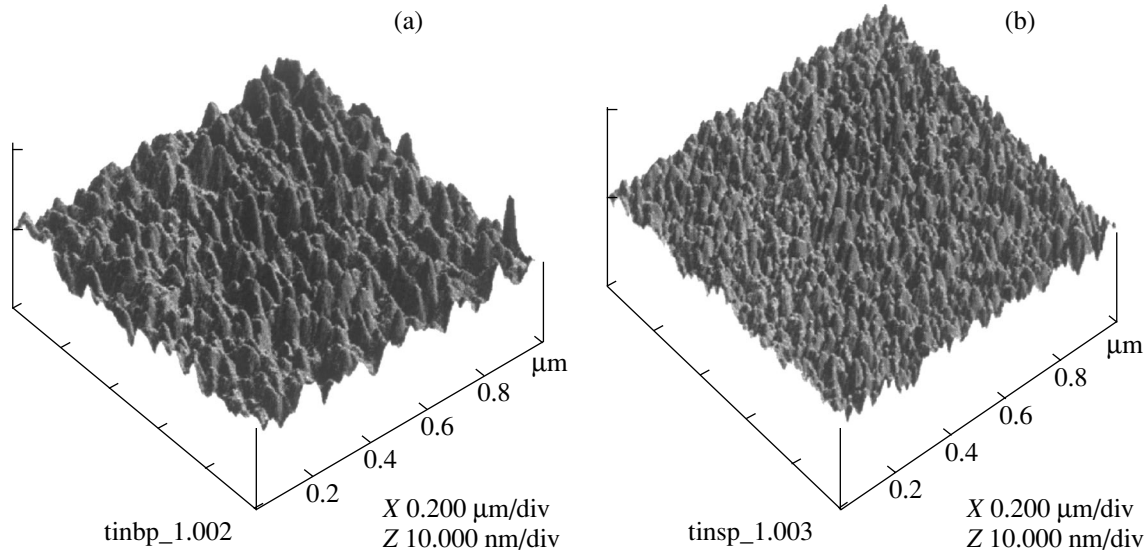
Fig. 1. Three-dimensional AFM images (1×1 µm) of ~1 µm TiN films deposited by nonmagnetron RF sputtering (a) without and (b) with applied magnetic field.

(i) The general level of conductivity in the TiN films studied is much lower compared to the values reported in [1, 7, 8], which is explained by the superstoichiometric character of our samples. A significant (by three to five orders of magnitude) decrease of electric conductivity in the superstoichiometric compositions, which is typical of group IV transition metal nitrides, is related to an increase in the fraction of the ionic bond component (including the transition from nitride to monoxide in $Me^{IV}N$–$Me^{IV}O$ type) and is sometimes accompanied by inversion of the R_H sign [8, 9].

(ii) Judging from the sign of R_H, the major charge carriers in the samples studied were electrons. The values of R_H were also the same in the films of types I and II. At a constant carrier density, a change in the conductivity with decreasing L in these films is determined only by a decrease in the mobility of carriers caused by their scattering on the grain boundaries. This is qualitatively consistent with the data reported in [1] (see Table 2) for nitride films with metallic conductivity.

(iii) In contrast to metal-like substoichiometric and stoichiometric nitrides [8], our films exhibited exponential growth in conductivity with increasing temperature. As is known (see, e.g., [10]), the conductivity activation energy can be determined by the presence of potential barriers. In the region of $T > 150$ K, the values of Q for the films of types I and II are close (0.21 and 0.18 eV, respectively). However, the plot of $\sigma = f(1/T)$

Table 1. Electrical and galvanomagnetic characteristics of TiN films

Sample type	Grain size L, nm	Conductivity σ, Ω^{-1} cm^{-1}		Hall coefficient R_H, cm^3/C	Carrier density n, cm^{-3}	Carrier mobility μ, cm^2/(V s)
		$T = 300$ K	$-Q$, eV			
Film I	29 ± 15	250	0.21 ($T > 150$ K) 0.087 (T < 150 K)	-2.6×10^{-4}	2.4×10^{22}	0.065
Film II	8.8 ± 2.2	26.5	0.18			0.007

Table 2. Room-temperature kinetic characteristics of TiNi (published data)

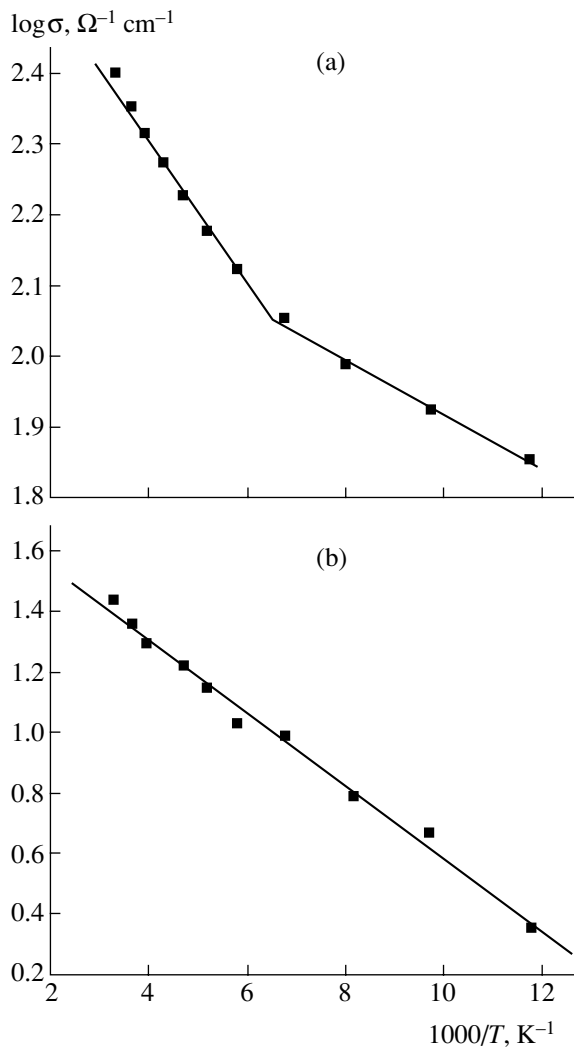| Sample	$\sigma \times 10^{-4}$, Ω^{-1} cm^{-1}	R_H, cm^3/C	n, cm^{-3}	μ, cm^2/(V s)
Single crystal TiN film [7]	5.56	–	–	–
Superlattice TiN/VN [1]	3.33	$-\sim1.4 \times 10^{-4}$	$(4.5 \pm 1) \times 10^{22}$	5 ($\delta_{TiN} > 3$ nm)
	1.43			~1.5 ($\delta_{TiN} = 0.5$ nm)
Sintered TiN [8]	0.5–3	$(-0.6 - +2) \times 10^{-4}$	10^{22}–10^{23}	1–10

Fig. 2. Temperature dependence of the conductivity of nanostructured TiN films of (a) type I and (b) type II.

for the coarse-grained film (type I) exhibits a break at $T \sim 150°C$, whereby the activation energy decreases approximately by half, which is probably related to a manifestation of the tunneling effect.

As is known [11], the fraction θ of near-boundary regions in nanostructured materials can be estimated from the relation $\theta = 3s/L$, where s is the width of the boundary region (usually assumed to be ~1 nm). For the films studied, these estimates are $\theta_I \sim 10\%$ and $\theta_{II} \sim 34\%$.

However, the difference must be more substantial with allowance for the grain size distribution. Thus, the density of carriers (predominantly electrons) in the samples of types I and II is the same despite a significant difference in the fraction of near-boundary regions. The temperature dependence of the conductivity of TiN films studied is exponential and exhibits a break for the films of type I. Elucidation of the nature of this anomaly requires additional investigations.

REFERENCES

1. N. Hirashita, J. E. Greene, U. Helmerson, *et al.*, J. Appl. Phys. **70**, 4963 (1991).
2. W. Tsai, M. Delfino, J. A. Fair, *et al.*, J. Appl. Phys. **73**, 4462 (1993).
3. R. A. Andrievski, Usp. Khim. **66**, 57 (1997) [Russ. Chem. Rev. **66**, 53 (1997)].
4. R. A. Andrievski, G. V. Kalinnikov, N. P. Kobelev, *et al.*, Fiz. Tverd. Tela (St. Petersburg) **39**, 1859 (1997) [Phys. Solid State **39**, 1661 (1997)].
5. R. A. Andrievski and G. V. Kalinnikov, Surf. Coat. Technol. **142–144**, 573 (2001).
6. G. V. Kalinnikov and R. A. Andrievski, Perspekt. Mater., No. 4, 26 (2003).
7. B. O. Johansson, J.-E. Sundgren, J. E. Greene, *et al.*, J. Vac. Sci. Technol. A **3**, 303 (1985).
8. E. A. Zhurakovskiĭ and V. F. Nemchenko, *Kinetic Characteristics and Electronic Structure of Interstitial Phases* (Naukova Dumka, Kiev, 1990) [in Russian].
9. B. O. Johansson, H. T. Hentzell, J. M. Harper, *et al.*, J. Mater. Res. **1**, 442 (1986).
10. B. M. Gol'tsman and Z. M. Dashevsky, *Film Thermoelements: Physics and Applications* (Nauka, Moscow, 1985) [in Russian].
11. R. A. Andrievski and A. M. Glezer, Fiz. Met. Metalloved. **88**, 50 (1999) [Phys. Met. Metallogr. **88**, 46 (1999)].

Translated by P. Pozdeev

Analytical Inversion of the Hypersingular Operator: Applications in the Theory of Antennae

S. I. Éminov

Novgorod State University, Novgorod, Russia
e-mail: tel@novsu.ac.ru; theorphy@novsu.ac.ru
Received May 17, 2004

Abstract—Analytical inversion of the hypersingular operator is obtained and used to develop an effective numerical-analytical method of solving hypersingular integral equations. Applications of the inverse operator to the theory of antennae are considered. © 2004 MAIK "Nauka/Interperiodica".

Introduction. By definition, a hypersingular integral equation has the following form:

$$(Au)(\tau) + (Nu)(\tau) = v(\tau), \quad -1 \le \tau \le 1, \quad (1)$$

where

$$(Au)(\tau) = \frac{1}{\pi}\frac{\partial}{\partial\tau}\int_{-1}^{1} u(t)\frac{\partial}{\partial t}\ln\frac{1}{|t-\tau|}dt, \quad (2)$$

$$(Nu)(\tau) = \int_{-1}^{1} u(t)N(t,\tau)dt. \quad (3)$$

Accordingly, operator A is also called hypersingular. Equation (1) is involved in the solution of many problems in the theories of diffraction and elasticity. Moreover, this is the basic equation in the theory of antennae. For this reason, there are many papers addressing the solution and analysis of Eq. (1).

In particular, it was suggested [1, 2] to use integration by parts for passing to a singular equation with respect to a derivative of an unknown function. Alternatively, direct numerical techniques have been developed [3, 4] for solving Eq. (1), which employ the collocation method and the Galerkin method.

However, direct numerical techniques are ineffective in many applications, in particular, in the antenna excitation theory. This is related to peculiarities of the right-hand part of Eq. (1) involving the $v(\tau)$ function, which may have a pronounced extremum and behave as a slowly converging series. In such cases, direct numerical techniques are ineffective.

In this Letter, a new method is proposed for solving the problem under consideration, which is based on the analytical inversion of the hypersingular operator.

Analytical inversion of the hypersingular operator. Previously, the hypersingular operator was studied in [4], where it was written in a different form as

$$(Au)(\tau) = \int_{-\infty}^{+\infty} |x| \int_{-1}^{1} u(t)\exp(ix(t-\tau))dtdx. \quad (4)$$

Since operator A is unbounded in space $L_2[-1, 1]$, by the identity of operators defined by Eqs. (2) and (4) we imply their equality on a dense set. This can be readily checked using the well-known relation

$$\ln\frac{1}{|\tau-t|} = C + \int_{0}^{1}\frac{\cos(\tau-t)x-1}{x}dx + \int_{1}^{+\infty}\frac{\cos(\tau-t)x}{x}dx,$$

where C is the Euler constant.

It was demonstrated [4] that operator A has a dense domain of definition in space $L_2[-1, 1]$ and is a symmetric and positive definite operator. This allows us to introduce the energy space H_A of this operator. In the analytical form, an orthonormal basis set of the energy space H_A can be analytically expressed as

$$\varphi_n(\tau) = \sqrt{\frac{2}{\pi n}}\sin[n\arccos(\tau)] = \sqrt{\frac{2}{\pi n}}\sqrt{1-\tau^2}U_n(\tau),$$
$$n = 1, 2, 3, \ldots, \quad (5)$$

$$(A\varphi_n, \varphi_m) = \begin{cases} 1, & m = n \\ 0, & m \ne n, \end{cases} \quad (6)$$

where $(\cdot, \cdot)$ denotes the scalar product in $L_2[-1, 1]$ and $U_n(\tau)$ are the Chebyshev polynomials of the second kind: $U_1(\tau) = 1$, $U_2(\tau) = 2\tau$, $U_3(\tau) = 4\tau^2 - 1$, etc.

In view of the importance of (6), let us consider a proof of this relation. As is known [2], the Chebyshev

polynomials of the first kind obey the relation

$$\frac{1}{\pi}\int_{-1}^{1}\frac{\cos(n\arccos(t))}{\sqrt{1-t^2}}\ln\frac{1}{|t-\tau|}dt = \frac{1}{n}\cos(n\arccos(\tau)), \quad (7)$$

$$n \geq 1.$$

Performing integration by parts in the expression for $A\varphi_m$, calculating the integral using relation (7), and differentiating the result, we obtain

$$A\varphi_n = \sqrt{\frac{2}{\pi m}}\frac{\partial}{\partial\tau}\left(\frac{1}{\pi}\int_{-1}^{1}\sin(m\arccos(t))\frac{\partial}{\partial t}\ln\frac{1}{|\tau-t|}dt\right)$$

$$= \sqrt{\frac{2}{\pi m}}\frac{\partial}{\partial\tau}\left(\frac{1}{\pi}m\int_{-1}^{1}\frac{\cos(m\arccos(t))}{\sqrt{1-t^2}}\ln\frac{1}{|\tau-t|}dt\right) \quad (8)$$

$$= \sqrt{\frac{2}{\pi m}}\frac{\partial}{\partial\tau}\cos(m\arccos(\tau)) = \sqrt{\frac{2}{\pi m}}\frac{\sin(m\arccos(\tau))}{\sqrt{1-\tau^2}}m.$$

This yields

$$(A\varphi_m, \varphi_n) = \sqrt{\frac{2}{\pi m}}m\sqrt{\frac{2}{\pi n}}$$

$$\times\int_{-1}^{1}\frac{\sin(m\arccos(\tau))\sin(n\arccos(\tau))}{\sqrt{1-\tau^2}}dt$$

$$= \sqrt{\frac{2}{\pi m}}m\sqrt{\frac{2}{\pi n}}\int_{0}^{\pi}\sin(m\varphi)\sin(n\varphi)d\varphi = \begin{cases}1, & m = n, \\ 0, & m \neq n,\end{cases}$$

which proves relation (6).

Let us consider an equation containing only the hypersingular operator,

$$(Au)(\tau) = \frac{1}{\pi}\frac{\partial}{\partial\tau}\int_{-1}^{1}u(t)\frac{\partial}{\partial t}\ln\frac{1}{|t-\tau|}dt = v(\tau), \quad (9)$$

$$-1 \leq \tau \leq 1,$$

and find a solution of this equation in the form of a series,

$$u(t) = \sum_{n=1}^{+\infty}c_n\varphi_n(t). \quad (10)$$

Substituting formula (10) into Eq. (9), multiplying both parts by φ_m in $L_2[-1, 1]$, and taking into account relation (6), we obtain

$$c_n = (y, \varphi_m).$$

Therefore, a solution of Eq. (9) can be written as

$$u(t) = \sum_{n=1}^{+\infty}(v, \varphi_n)\varphi_n(t). \quad (11)$$

Taking into account definition (5) of the basis set functions $\varphi_n(t)$, this series can be rewritten as

$$u(\tau)$$
$$= \frac{2}{\pi}\int_{-1}^{1}v(t)\left(\sum_{n=1}^{+\infty}\frac{1}{n}\sin(n\arccos(t))\sin(n\arccos(\tau))\right)dt. \quad (12)$$

Using the known sum of the series,

$$\sum_{n=1}^{+\infty}\frac{1}{n}\sin x\sin x'$$
$$= \frac{\ln 2}{2} + \ln\left|\sin\frac{x+x'}{2}\right| - \frac{1}{2}\ln|\cos x - \cos x'|, \quad (13)$$

we obtain the final expression for the solution of Eq. (9):

$$u(\tau) = \frac{2}{\pi}\int_{-1}^{1}v(t)$$
$$\times\left(\frac{\ln 2}{2} + \ln\sin\frac{\theta(t)+\theta(\tau)}{2} - \frac{1}{2}\ln|\tau - t|\right)dt, \quad (14)$$

where $\theta(t) = \arccos(t)$. Thus, we have analytically found a solution of Eq. (4), that is, obtained the analytical inversion of the hypersingular operator.

Reduction of the hypersingular equation to an infinite system of Fredholm-type equations of the second kind. A numerical-analytical method of solution. In order to solve the initial hypersingular equation,

$$\frac{1}{\pi}\frac{\partial}{\partial\tau}\int_{-1}^{1}u(t)\frac{\partial}{\partial t}\ln\frac{1}{|t-\tau|}dt + \int_{-1}^{+1}u(t)N(t,\tau)dt = v(\tau), \quad (15)$$

$$-1 \leq \tau \leq 1,$$

let us expand the unknown function in terms of the basis set,

$$u(t) = \sum_{n=1}^{+\infty}c_n\varphi_n(t) \quad (16)$$

and reduce Eq. (15) in space H_A to an equivalent infinite system in the space of sequences l_2,

$$c_n + \sum_{m=1}^{+\infty}c_m N_{mn} = v_n, \quad 1 \leq n \leq +\infty, \quad (17)$$

where

$$N_{mn} = \int\limits_{-1}^{+1}\int\limits_{-1}^{+1} N(t,\tau)\varphi_m(t)\varphi_n(\tau)dtd\tau,$$

$$v_n = \int\limits_{-1}^{+1} v(\tau)\varphi_n(\tau)d\tau.$$

If the operator $A^{-1}N$ is completely continuous in space H_A, then Eq. (17) is a Fredholm-type equation of the second kind in the space of sequences l_2, whereby the matrix elements N_{mn} form a completely continuous operator. One criterion of the complete continuity of the $A^{-1}N$ operator in space H_A was formulated in [4].

Now, let us proceed with solving the infinite system of equations (17). In many problems of mathematical physics, infinite systems can be successfully solved by method of truncation. According to this, an approximate solution is found for a truncated system,

$$\tilde{c}_n + \sum_{m=1}^{M} \tilde{c}_m N_{mn} = v_n, \quad 1 \le n \le M, \qquad (18)$$

and an exact solution of the hypersingular equation is obtained using the formula

$$u(t) = \sum_{n=1}^{M} \tilde{c}_n\varphi_n(t).$$

The rate of convergence of the truncation procedure also depends on the rate of decrease of the right-hand side of Eqs. (17). In many applied problems, this rate is slow and the truncation method is ineffective. This problem can be solved using the new numerical-analytical method described below. Let us look for a solution of the infinite system (17) in the following form:

$$c_n = v_n + \dot{c}_n. \qquad (19)$$

Substituting expression (19) into Eq. (17), we obtain

$$\dot{c}_n + \sum_{m=1}^{+\infty} \dot{c}_n N_{mn} = -\sum_{m=1}^{+\infty} v_m M_{mn}. \qquad (20)$$

The right-hand side of this system decreases quite rapidly because the matrix elements N_{mn} determine a completely continuous operator. Solving system (20) by method of truncation and taking into account formula (19), we obtain a solution of hypersingular equation (15) in the following form:

$$u(t) = \sum_{n=1}^{+\infty} v_n\varphi_n(t) + \sum_{n=1}^{M} \tilde{\dot{c}}_n\varphi_n, \qquad (21)$$

where $\tilde{\dot{c}}_n$ is the solution of the truncated system corresponding to Eqs. (20). Applying formula (14) for the

analytical inversion of the hypersingular operator, we can express solution (21) as follows:

$$u(\tau) = \frac{2}{\pi}\int\limits_{-1}^{1} v(t)\left(\frac{\ln 2}{2} + \ln\sin\frac{\theta(t)+\theta(\tau)}{2} - \frac{1}{2}\ln|\tau-t|\right)dt$$

$$+ \sum_{n=1}^{M} \tilde{\dot{c}}_n + \varphi_n. \qquad (22)$$

Hypersingular equation of a dipole antenna. A hypersingular equation describing the current $I(\tau)$ flowing over the surface of a dipole has the following form [4]:

$$\beta(AI)(\tau) + (NI)(\tau) = v(\tau), \quad -1 \le \tau \le 1, \qquad (23)$$

where

$$(NI)(\tau)$$

$$= \frac{l}{2\pi^2}\int\limits_{0}^{+\infty}\left[(x^2-1)I_0(\sqrt{x^2-1}\,a)K(\sqrt{x^2-1}\,a) - \frac{x}{2a}\right]$$

$$\times \int\limits_{-1}^{+1} I(t)\cos(lx(\tau-t))dtdx,$$

$$\beta = \frac{1}{4\pi la}, \quad v(\tau) = i\sqrt{\frac{\varepsilon}{\mu}}E^0(\tau);$$

I_0 and K_0 are the modified Bessel functions; E^0 is the primary electric field; ε and μ are the dielectric permittivity and magnetic susceptibility, respectively; $2l$ is the electrical length; and a is the electrical radius of the dipole.

In the theory of dipoles, as well as in mathematical physics in general, the primary field is frequently represented in terms of the delta function as

$$E^0(\tau) = U_0\delta(\tau), \qquad (24)$$

where $\delta(\tau)$ is the Dirac delta and U_0 is the voltage amplitude. However, this model is inapplicable for exactly solving Eq. (23) because, according to the formulas of analytical inversion, the solution would become infinite. For this reason, let us represent the primary field as

$$E^0(\tau) = \frac{U_0}{2T}\begin{cases}1, & |\tau| \le T, \\ 0, & |\tau| > T.\end{cases} \qquad (25)$$

When the parameter T tends to zero, function (25) approaches delta function (24) in the integral sense.

The input impedance of a dipole antenna calculated by two methods

N	Galerkin method		Numerical-analytical method	
	ReZ	ImZ	ReZ	ImZ
2	91.347	51.292	115.41	22.880
5	100.53	44.011	116.59	19.332
10	105.44	38.999	116.62	19.431
15	107.95	35.854	116.54	19.682
20	109.65	33.467	116.49	19.822

In this case, integral (14) can be calculated explicitly:

$$\frac{2}{\pi}\int_{-1}^{1} E^0(t)\left(\frac{\ln 2}{2} + \ln\sin\frac{\theta(t)+\theta(\tau)}{2} - \frac{1}{2}\ln|\tau - t|\right)dt$$

$$= U_0\frac{f(T,\tau) - f(-T,\tau)}{\pi T},$$ (26)

where

$$f(t,\tau) = \frac{\ln 2}{2}t + \frac{1}{2}\ln\frac{1 - t\tau + \sqrt{1-t^2}\sqrt{1-\tau^2}}{2}(t-\tau)$$

$$- \frac{\theta(t)\sqrt{1-\tau^2}}{2} - \frac{(t-\tau)\ln(1-\tau)}{2}.$$

An analysis of expression (26) reveals various properties of the system. For $T = 1$, the right-hand side of this equation obeys the Meixner edge conditions. For $\tau = 0$ and $T \longrightarrow 0$, the right-hand side in Eq. (26) logarithmically tends to infinity (which explains the inapplicability of delta function model (24)).

In conclusion, let us consider a solution obtained using formula (22) for hypersingular equation (23) with the parameters $I = \pi/2$, $a = l/20$, and $T = 0.01$. The results of calculation of the input impedance of a dipole defined by the formula

$$Z = \frac{U_0}{I(0)}$$

for various numbers of basis set functions N are presented in the table. These data illustrate slow convergence of the Galerkin method and rapid convergence of the proposed numerical-analytical method.

REFERENCES

1. A. I. Kalandiya, *Mathematical Methods of Two-Dimensional Elasticity* (Nauka, Moscow, 1973) [in Russian].

2. V. V. Panasyuk, M. P. Savruk, and Z. T. Nazarchuk, *Method of Singular Integral Equations in Two-Dimensional Problems of Diffraction* (Naukova Dumka, Kiev, 1984) [in Russian].

3. I. K. Lifanov, *Method of Singular Integral Equations and Numerical Experiment* (Yanus, Moscow, 1995) [in Russian].

4. S. I. Eminov, Radiotekh. Élektron. (Moscow) **38**, 2160 (1993).

Translated by P. Pozdeev

The Physical Nature of the Optical Emission and Absorption Accompanying Explosive Decomposition of Heavy Metal Azides

V. I. Oleshko*, V. I. Korepanov, V. M. Lisitsyn, and V. P. Tsypilev

Tomsk Polytechnical University, Tomsk, Russia
* e-mail: oleshko@tpu.ru
Received May 12, 2004

Abstract—The kinetics and spatial characteristics of the optical emission and absorption have been studied in the course of explosive decomposition of silver azide initiated by a pulsed electron beam. The emission and absorption observed after the induction period reflect the process of formation and expansion of the products of chemical decomposition of silver azide. © *2004 MAIK "Nauka/Interperiodica".*

The mechanism of explosive decomposition of heavy metal azides (HMAs) initiated by pulsed electron and laser beams is still incompletely clear and subject to discussion [1–5]. One of the most effective and promising methods for the investigation of primary processes involved in the explosive decomposition of HMAs consists in monitoring, with high time resolution (on a nanosecond level), the kinetics of optical emission and absorption accompanying the explosion.

Aduev *et al.* [2, 3] established that optical emission kinetics exhibits a complicated character: the first peak of optical emission arises with an 0.2 µs delay relative to the excitation pulse and lasts for 1–1.5 µs, while the second emission peak is observed between 2.5 and 7 µs. It was suggested that the first peak, characterized by a continuous emission spectrum, and the synchronously observed optical absorption within the excitation band are caused by processes occurring in the solid phase prior to mechanical disintegration of the explosive (these phenomena are called "preexplosion luminescence" and "preexplosion optical absorption"). The second peak was assigned [2] to the emission from plasma formed at the moment of explosive decomposition of HMAs.

Previously [6], we reported that HMA samples excited by a pulse of accelerated electrons exhibited a noninertial peak of optical emission with properties typical of pulsed cathodoluminescence from wide-bandgap semiconductors: the emission pulse at 300 K had a duration below 20 ns and a spectrum with a short-wavelength limit at the fundamental absorption edge. Thus, according to the above model, two peaks of emission—the first (with duration below 20 ns) and the second (1–1.5 µs wide and delayed by 0.2 µs)—are attributed to luminescence from the solid phase, which is hardly probable.

The aim of this study was to monitor the kinetic and spatial characteristics of the optical emission from silver azide excited by a pulsed electron beam and to establish the nature of delayed (inertial) optical emission and absorption observed after the induction period. The main experimental problem was to separate the solid-phase luminescence and the optical emission from plasma and to determine the moment of phase transition in the explosive.

The dynamics of formation and expansion of the products of explosion was studied using an experimental scheme depicted in Fig. 1. The explosion was initiated by a pulsed electron beam with an effective electron energy of ~0.3 MeV, a pulse duration of ~25 ns, and a power density of ~0.1 J/cm². Powdered silver azide (AgN_3) was compacted under a pressure of 10^9 Pa into samples having the form of disks with a thickness of $d_2 = 200$–300 µm and a diameter of 5 mm. Sample *1* was mounted in holder *2* (having a channel for the electron beam passage) and surrounded by ring screen *3*
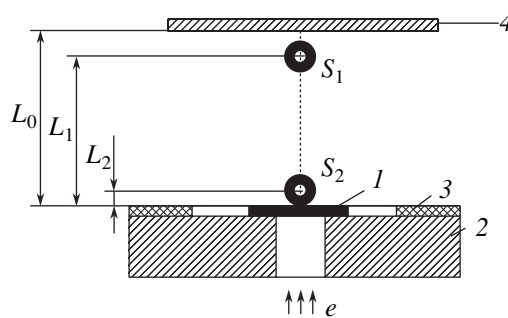

Fig. 1. Schematic diagram of the monitoring of optical emission and transmission of the products of explosive decomposition of silver azide (see the text for explanations).
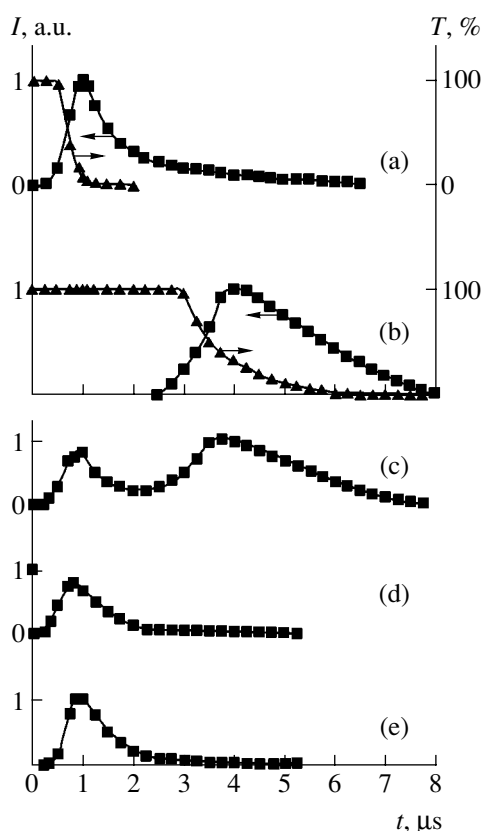
Fig. 2. Kinetics of optical emission and transmission accompanying the explosive decomposition of silver azide (see the text for explanations).

having a thickness of $d_1 \geq d_2$. Sheet screen *4* was placed at a distance of L_0 from the sample in order to block expansion of the explosion products.

The optical transmission of the products of explosive decomposition of AgN_3 was measured using a collimated probing laser beam (He–Ne laser, $\lambda = 632.8$ nm) passing parallel to the rear sample surface at a distance of L_1 from the sample. The intensity of radiation transmitted through the plasma torch of the explosive decomposition products was studied as a function of the time after excitation of the sample. Images of the sample and the plasma expansion zone were projected by lenses onto the exit slits of two grating monochromators (MDR-23). Using two photomultipliers (FEU-118), it was possible to monitor the kinetics of both optical emission and transmission of the products of explosive decomposition of AgN_3 at the given distance from the rear side of the sample. The signals from photodetectors in both (emission and transmission) channels was fed via matched loads ($R = 50$ Ω) into a double-beam oscillograph (S8-14). The optical emission and transmission could be monitored in any region of the expansion zone of the plasma torch. The dimensions of these regions were determined by the monochromator slit widths and the apertures ($S_1 = 0.5$ mm

and $S_2 = 2$ mm) arranged in front of the entrance slits. In the scheme depicted in Fig. 1, the optical emission from the AgN_3 sample could not reach the detector measuring the emission kinetics. Therefore, any emission measured by this detector originates outside of the sample and is due to the products of the explosive decomposition of AgN_3.

Figures 2a and 2b show the typical kinetics of the optical emission ($\lambda = 600$ nm) and transmission of the products of explosive decomposition measured for the zones near the rear surface of AgN_3 ($L_2 = 0.2$ mm) and near screen *4* ($L_1 = 9$ mm), respectively. The results of panoramic monitoring of the optical emission from the entire plasma torch zone bounded by the screen are presented in Fig. 2c. The time is measured from the moment of sample excitation by the electron beam. The curves in Figs. 2a and 2b indicate that the signals due to the optical emission and absorption of the explosive decomposition products appear with a delay of $t_1 = t_2 + t_3$, where t_2 is the induction period and t_3 is the time of plasma front propagation to the probed region. For $L_2 = 0.2$ mm, the delay time is ~300–400 ns, while for $L_1 = 9$ mm this time is $t_1 \sim 2.8$–3 µs. The kinetic curve obtained by panoramic monitoring of the entire plasma torch zone exhibits both emission peaks.

In order to study the complete kinetics of emission accompanying the explosive decomposition of AgN_3, we used an experimental arrangement in which the sample was oriented at an angle of 45° relative both to the electron beam direction and to the optical axis of the detection scheme. In this geometry, it was possible to measure (without spatial resolution) all kinds of electron beam initiated emission from the irradiated surface of the sample. The oscillograms of optical emission were measured under different conditions. The curve presented in Fig. 2d was obtained for the open exposed surface of the sample, while the curve in Fig. 2e corresponds to the same surface screened by a thin (~10-µm-thick) aluminum foil. Such a foil is transparent for the electron beam, but not for the light. A comparison of the results of two experiments shows that the first curve displays two emission peaks, corresponding to the non-delayed cathodoluminescence and the emission delayed by ~0.2 µs, while the second curve has only one peak. The pulse of cathodoluminescence is not transmitted through the foil, but the second peak is observed because the foil is destroyed by the expanding explosive decomposition products. The peak of the second curve is shifted by ~100 ns relative to that of the corresponding signal observed from the open (unscreened) sample surface, which is related to a certain retardation of the expanding products by the foil.

The experimental facts described above provide unambiguous evidence for the plasma origin of the delayed emission peaks and agree well with the theory of explosive decomposition. Indeed, according to this theory [7], the products of explosion in the initial stage

exist in the form of a dense (compressed by a pressure of 3×10^{10} Pa) plasma with a temperature of up to 3500–4400 K. The maximum of the continuous emission spectrum of this plasma must occur at a wavelength of ~700–800 nm. Note that the maximum of "preexplosion luminescence" was observed in this very interval [3].

The kinetic characteristics of the optical emission and absorption accompanying the explosive decomposition of AgN_3 can be explained as follows. At the moment of the electron beam action, AgN_3 exhibits a cathodoluminescence pulse with a width equal to that of the excitation pulse (~25 ns). After termination of the induction period, with approximately ~0.2 μs delay, the explosive decomposition of AgN_3 leads to the formation of a dense low-temperature plasma cloud. This moment corresponds to the leading front of the first delayed emission peak and the accompanying optical absorption signal. The kinetics of decay of this emission component is determined by the process of free expansion of the plasma torch in vacuum. The subsequent plasma expansion stage does not influence the optical emission, but is always manifested in the absorption. The second delayed emission peak is observed only if the expanding plasma torch meets an obstacle.

Thus, the results of our investigations show that the luminescence from AgN_3 takes place only at the moment of electron beam action on the explosive. The following delayed optical emission peak is related to the emission from gaseous products of explosive decomposition near the excited sample surface.

REFERENCES

1. E. I. Aleksandrov and V. P. Sipilev, Fiz. Goreniya Vzryva **17** (5), 77 (1981).

2. B. P. Aduev, É. D. Aluker, Yu. A. Zakharov, *et al.*, Pis'ma Zh. Éksp. Teor. Fiz. **66** (2), 101 (1997) [JETP Lett. **66**, 111 (1997)].

3. Yu. A. Zakharov, É. D. Aluker, B. P. Aduev, *et al.*, *Pre-Explosion Phenomena in Azides of Heavy Metals* (Khimmash, Moscow, 2002) [in Russian].

4. V. P. Tsypilev, V. I. Korepanov, V. M. Lisitsyn, *et al.*, Izv. Tomsk. Politekh. Univ. **306** (6), 46 (2003).

5. S. M. Ryabykh, V. S. Dolganov, and K. Sh. Karabukaev, Fiz. Goreniya Vzryva **29** (2), 75 (1993).

6. V. I. Korepanov, V. M. Lisitsyn, and V. I. Oleshko, Pis'ma Zh. Tekh. Fiz. **28** (24), 48 (2002) [Tech. Phys. Lett. **28**, 1043 (2002)].

7. C. Johansson and P. Persson, *Detonics of High Explosives* (Academic, New York, 1970).

Translated by P. Pozdeev

Reconstruction of the Equation of a System
with Two Delay Times from Time Series

V. I. Ponomarenko and M. D. Prokhorov

Institute of Radio Engineering and Electronics (Saratov Branch),
Russian Academy of Sciences, Saratov, Russia
e-mail: sbire@sgu.ru

Abstract—A method is proposed for the use of time series for reconstructing the equations of a system with time-delay feedback characterized by two delay times. The performance of the proposed method is illustrated by application to a generalized Mackey–Glass equation. © *2004 MAIK "Nauka/Interperiodica"*.

Introduction. Dynamical systems with time-delay feedback (time-delay systems), the behavior of which is not entirely determined by the present state, but depends on the preceding states as well, are frequently encountered in nature [1]. Accordingly, time-delay systems are usually described in terms of differential equations with delayed arguments. Such models are successfully used in various fields of physics, biology, physiology, and chemistry [2–6]. In modeling a time-delay system, it is frequently necessary to take into account the dependence of the current state on several preceding states, that is, to use a model with several delay times [7–9]. In recent years, several different approaches were developed for reconstructing the model equations of delay systems from their time series [10–19]. However, the proposed methods were used only for the reconstruction of differential equations with a single delay time. Application of the proposed methods in the case of systems with two or more delay times is not always possible.

In this paper, methods developed previously [16, 17] for the reconstruction of the model equations of time-delay systems from their chaotic time series are extended so as to include the case of systems characterized by two delay times.

Description of the method. Consider a time-delay system described by a first-order differential equation with two delay times, τ_1 and τ_2, of the following general type:

$$\dot{x}(t) = F(x(t), x(t - \tau_1), x(t - \tau_2)). \quad (1)$$

In order to restore the delay times τ_1 and τ_2 from the observable time series $x(t)$, we will use a method [16] employing the fact that time series of delay systems of the type $\dot{x}(t) = G(x(t), x(t - \tau))$ possess virtually no extrema separated from each other by τ. It will be shown that this method, based on the laws governing the distribution of maxima in the time series of time-delay systems, can be applied to the systems of type (1).

Differentiating Eq. (1) with respect to time, we obtain

$$\ddot{x}(t) = \frac{\partial F}{\partial x(t)} \dot{x}(t) + \frac{\partial F}{\partial x(t - \tau_1)} \dot{x}(t - \tau_1)$$
$$+ \frac{\partial F}{\partial x(t - \tau_2)} \dot{x}(t - \tau_2). \quad (2)$$

The extrema of the time series $x(t)$ described by Eq. (1) in the typical case are quadratic. Such extremal points obey the conditions $\dot{x}(t) = 0$ and $\ddot{x}(t) \neq 0$. Therefore,

$$a\dot{x}(t - \tau_1) + b\dot{x}(t - \tau_2) \neq 0, \quad (3)$$

where

$$a = \partial F(x(t), x(t - \tau_1), x(t - \tau_2))/\partial x(t - \tau_1),$$

$$b = \partial F(x(t), x(t - \tau_1), x(t - \tau_2))/\partial x(t - \tau_2).$$

Inequality (3) holds provided that $\dot{x}(t - \tau_1) \neq 0$ or $\dot{x}(t - \tau_2) \neq 0$. This implies that the derivatives $\dot{x}(t)$ and $\dot{x}(t - \tau_1)$, as well as $\dot{x}(t)$ and $\dot{x}(t - \tau_2)$, do not vanish simultaneously or, in other words, there are no extrema spaced by τ_1 or τ_2 from a given quadratic extremum. In order to find τ_1 or τ_2, one has to indicate extrema in the initial time series $x(t)$, determine the numbers N of the pairs of extrema spaced by various times τ, and construct the distribution $N(\tau)$. The $N(\tau)$ curve will exhibit pronounced minima at $\tau = \tau_1$ and $\tau = \tau_2$ corresponding to the delay times. Note, however, that the minima in $N(\tau)$ are not as pronounced as in the case of a system with a single delay time because only one term in inequality (3) must be nonzero.

Reconstruction of the other parameters of a system with two delay times from its time series will be illustrated for delay systems described by the equation

$$\varepsilon_0 \dot{x}(t) = -x(t) + f_1(x(t - \tau_1)) + f_2(x(t - \tau_2)), \quad (4)$$

where f_1 and f_2 are nonlinear functions and ε_0 is a dimensionless parameter characterizing the inertia of the system. Differentiating Eq. (4) with respect to time, we obtain

$$\varepsilon_0 \ddot{x}(t) = -\dot{x}(t) + \frac{\partial f_1(x(t - \tau_1))}{\partial x(t - \tau_1)} \dot{x}(t - \tau_1)$$
$$+ \frac{\partial f_2(x(t - \tau_2))}{\partial x(t - \tau_2)} \dot{x}(t - \tau_2). \quad (5)$$

This equation indicates that the conditions

$$\dot{x}(t - \tau_1) = \dot{x}(t - \tau_2) = 0, \quad (6)$$

lead to the relation $\varepsilon_0 \ddot{x}(t) = -\dot{x}(t)$, which yields a formula for the parameter of inertia:

$$\varepsilon_0 = -\frac{\dot{x}(t)}{\ddot{x}(t)}. \quad (7)$$

Thus, the parameter ε_0 can be evaluated by finding points obeying conditions (6) in the time series $x(t)$, determining the first and second derivatives at these points, calculating the corresponding values by formula (7), and taking their average.

In order to reconstruct the nonlinear functions f_1 and f_2, let us project a trajectory described by Eq. (4) from the infinite-dimensional phase space of time-delay system (4) onto the three-dimensional space $(\varepsilon_0 \dot{x}(t) + x(t), x(t - \tau_1), x(t - \tau_2))$. In this space, the set of points visited by the system occurs on a two-dimensional surface because, according to Eq. (4),

$$\varepsilon_0 \dot{x}(t) + x(t) = f_1(x(t - \tau_1)) + f_2(x(t - \tau_2)). \quad (8)$$

A section of this surface by the plane $x(t - \tau_2) = \text{const}$ allows the nonlinear function f_1 to be determined to within a constant. Indeed, the points in this section satisfy the equation $\varepsilon_0 \dot{x}(t) + x(t) = f_1(x(t - \tau_1)) + c_1$, where $c_1 = f_2(x(t - \tau_2))$ for the selected $x(t - \tau_2) = \text{const}$. Using the same method, we may reconstruct (to within a constant) the nonlinear function f_2 by using a section of the above surface by the plane $x(t - \tau_1) = \text{const}$. The points in this section satisfy the equation $\varepsilon_0 \dot{x}(t) + x(t) = f_2(x(t - \tau_2)) + c_2$, where $c_2 = f_1(x(t - \tau_1))$ for the selected $x(t - \tau_1) = \text{const}$.

Verification of the method. We will demonstrate the performance of the proposed reconstruction method
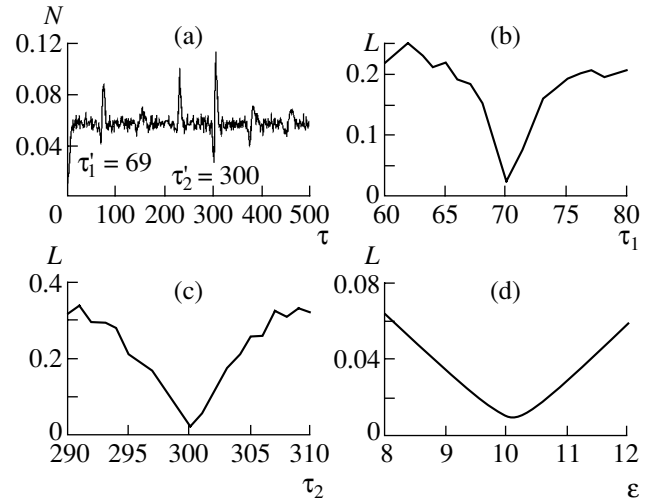

Fig. 1. Reconstruction of a system with two delay times: (a) plot of the number N of the pairs of extrema in a time series of Eq. (9) spaced by various times τ, normalized to the total number of extrema; (b) plot of the segments length L versus τ_1 for points (ordered with respect to abscissa) on the plane $(x(t - \tau_1) + c_1', \varepsilon_0' \dot{x}(t) + x(t))$; (c) L versus τ_2 for points on the plane $(x(t - \tau_2) + \hat{c}_2, \varepsilon_0' \dot{x}(t) + x(t))$; (d) L versus ε for points on the plane $(x(t - \hat{\tau}_1) + \hat{c}_1, \varepsilon \dot{x}(t) + x(t))$.

by applying the procedure outlined above to a generalized Mackey–Glass equation with two delay times:

$$\dot{x}(t) = -bx(t) + \frac{1}{2}\frac{a_1 x(t - \tau_1)}{1 + x^c(t - \tau_1)} + \frac{1}{2}\frac{a_2 x(t - \tau_2)}{1 + x^c(t - \tau_2)}. \quad (9)$$

Dividing both parts of Eq. (9) by b, we reduce this equation to the form of Eq. (4) with $\varepsilon_0 = 1/b$. We have performed numerical calculations with a unit integration step for a system (9) with the parameters $a_1 = 0.2$, $a_2 = 0.3$, $b = 0.1$, $c = 10$, $\tau_1 = 70$, and $\tau_2 = 300$, which corresponded to the motion on a chaotic attractor of high dimensionality.

Figure 1a shows the plot of $N(\tau)$. The first two of the most pronounced minima of this function allow the delay times to be estimated as $\tau_1' = 69$ and $\tau_2' = 300$. Note that another characteristic minimum in $N(\tau)$ is observed near $\tau = \tau_1 + \tau_2$. For these reconstructed values of τ_1' and τ_2', the average value of the parameter of inertia is $\varepsilon_0' = 9.4$ ($\varepsilon_0 = 1/b = 10$). The derivatives $\dot{x}(t)$ and $\ddot{x}(t)$ were evaluated from the time series using a local parabolic approximation. In order to decrease the error of determination of the parameter ε_0 by formula (7), the points with very small $\ddot{x}(t)$ values were rejected.

By projecting a time series of Eq. (9) onto the three-dimensional space $(\varepsilon_0' \dot{x}(t) + x(t), x(t - \tau_1'), x(t - \tau_2'))$ and constructing the sections of this space by the planes
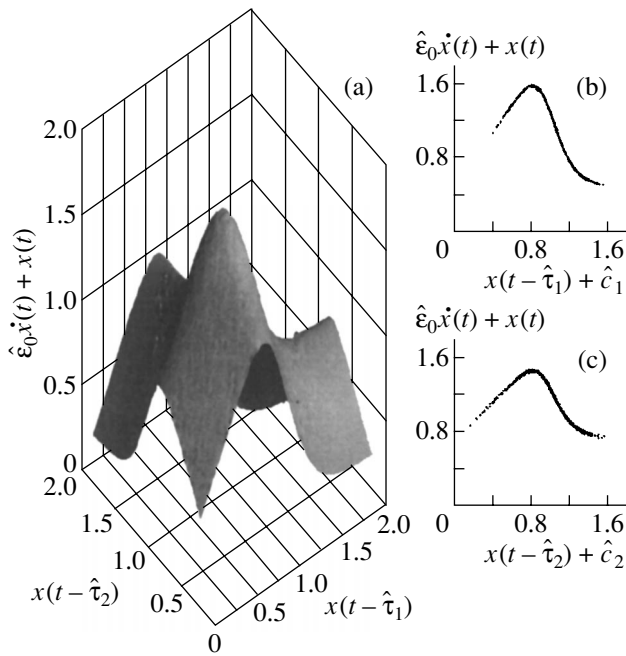
Fig. 2. Reconstruction of the nonlinear functions in Eq. (4) for $\hat{\varepsilon}_0 = 10.1$, $\hat{\tau}_1 = 70$ and $\tau_2 = 300$: (a) reconstructed surface described by Eq. (8) representing the sum of functions f_1 and f_2; (b) reconstruction of the nonlinear function f_1 to within $\hat{c}_1 = f_2(x(t - \hat{\tau}_2))$ for $x(t - \hat{\tau}_2) = 1$; (c) reconstruction of the nonlinear function f_2 to within $\hat{c}_2 = f_1(x(t - \hat{\tau}_1))$ for $x(t - \hat{\tau}_1) = 1$.

$x(t - \tau_1') = $ const and $x(t - \tau_2') = $ const, we reconstructed (to within constants) the nonlinear functions f_1 and f_2. However, because of relatively large errors involved in the determination of parameters τ_1 and ε_0, these nonlinear functions were determined with insufficient accuracy.

In order to provide for a higher quality of reconstruction of the model equation, it is possible to use the following procedure of refining the system parameters. By varying the value of τ_1 in a small vicinity of $\tau_1' = 69$, we constructed the plots of $\varepsilon_0' \dot{x}(t) + x(t)$ versus $x(t - \tau_1') + c_1'$ (where c_1' is determined by selecting the section $x(t - \tau_2') = $ const) so as to obtain the most unambiguous (single-valued) relationship. A quantitative criterion of such a unique relationship necessary for the refinement of τ_1 was the minimum length of a segment $L(\tau_1)$ connecting points (ordered with respect to abscissa) on the plane $(x(t - \tau_1) + c_1', \varepsilon_0' \dot{x}(t) + x(t))$. The curve of $L(\tau_1)$ (Fig. 1b) normalized to the number of points in the section under consideration exhibits a minimum at $\hat{\tau}_1 = 70$. Using the same procedure, we have refined the delay time τ_2 in a small vicinity of

$\tau_2' = 300$ (Fig. 1c). Note that the section $x(t - \hat{\tau}_1) = $ const is constructed using the refined value of $\hat{\tau}_1 = 70$. A minimum in $L(\tau_2)$ is observed at $\hat{\tau}_2 = 300$ (Fig. 1c). In the general case, $\hat{\tau}_2 \neq \tau_2'$ and the procedure of refinement for τ_1 is repeated for the section $x(t - \hat{\tau}_2) = $ const. Sequential refinement of the τ_1 and τ_2 values is continued until the delay times cease to change. For small deviations of the initial approximated parameters τ_1' and τ_2' from the true values, the procedure is converging and allows both delay times to be exactly determined.

After refinement of the delay times, it is necessary to refine the parameter of inertia as well. The new estimate, $\hat{\varepsilon}_0$, can be obtained using formula (7) and the procedure described above. However, more reliable evaluation is provided by using all points in one of the sections. This is achieved by varying ε in a small vicinity of ε_0' and constructing the plots of $\varepsilon \dot{x}(t) + x(t)$ versus $x(t - \hat{\tau}_1) + \hat{c}_1$ (where $\hat{c}_1$ is determined by selecting the section $x(t - \hat{\tau}_2) = $ const) so as to obtain the most unambiguous relationship. The corresponding curve of $L(\varepsilon)$ (Fig. 1d), normalized in the same way as $L(\tau_1)$ and $L(\tau_2)$, exhibits a minimum at $\hat{\varepsilon}_0 = 10.1$. It should be noted that the time of computation of the proposed procedure of sequential refinement of the system parameters is several orders of magnitude higher than that of the method based on the simultaneous trial of three variable parameters (ε, τ_1, τ_2) in the embedding space $(\varepsilon \dot{x}(t) + x(t), x(t - \tau_1), x(t - \tau_2))$.

Figure 2 shows the results of reconstruction of the nonlinear functions f_1 and f_2 for time-delay system (4) with refined parameters $\hat{\varepsilon}_0$, $\hat{\tau}_1$, and $\hat{\tau}_2$. The set of points in the three-dimensional space (Fig. 2a) reproduces with a good precision the two-dimensional surface described by Eq. (8). Using the corresponding sections of this surface (Figs. 2b and 2c), it is possible to reconstruct the nonlinear functions f_1 and f_2 to within a constant. The quality of reconstruction of these functions increases with the increasing sampling frequency (with decreasing integration step). In order to check the performance of the proposed method in the presence of perturbations, we applied it to a noisy system. It was found that the procedure described above ensures restoration of a time-delay system when the noise level is on the order of 10%.

REFERENCES

1. J. K. Hale and S. M. V. Lunel, *Introduction to Functional Differential Equations* (Springer, New York, 1993).

2. Y. Kuang, *Delay Differential Equations with Applications in Population Dynamics* (Academic Press, Boston, 1993).

3. K. Ikeda, Opt. Commun. **30**, 257 (1979).

4. R. Lang and K. Kobayashi, IEEE J. Quantum Electron. **16**, 347 (1980).

5. S. P. Kuznetsov, Izv. Vyssh. Uchebn. Zaved. Radiofiz. **25**, 1410 (1982).

6. G. A. Bocharov and F. A. Rihan, J. Comput. Appl. Math. **125**, 183 (2000).

7. K. L. Cooke and P. Driessche, J. Math. Biol. **35**, 240 (1996).

8. S. A. Gourley and M. V. Burtucelli, J. Math. Biol. **35**, 843 (1997).

9. H. Seidel and H. Herzel, Physica D **115**, 145 (1998).

10. M. J. Bünner, M. Popp, Th. Meyer, *et al.*, Phys. Rev. E **54**, 3082 (1996).

11. H. Voss and J. Kurths, Phys. Lett. A **234**, 336 (1997).

12. S. P. Ellner, B. E. Kendall, S. N. Wood, *et al.*, Physica D **110**, 182 (1997).

13. M. J. Bünner, Th. Meyer, A. Kittel, and J. Parisi, Phys. Rev. E **56**, 5083 (1997).

14. R. Hegger, M. J. Bünner, H. Kantz, and A. Giaquinta, Phys. Rev. Lett. **81**, 558 (1998).

15. M. J. Bünner, M. Ciofini, A. Giaquinta, *et al.*, Eur. Phys. J. D **10**, 165 (2000).

16. B. P. Bezruchko, A. S. Karavaev, V. I. Ponomarenko, and M. D. Prokhorov, Phys. Rev. E **64**, 056216 (2001).

17. V. I. Ponomarenko and M. D. Prokhorov, Pis'ma Zh. Tekh. Fiz. **28** (16), 37 (2002) [Tech. Phys. Lett. **28**, 680 (2002)].

18. V. S. Udaltsov, J.-P. Goedgebuer, L. Larger, *et al.*, Phys. Lett. A **308**, 54 (2003).

19. M. D. Prokhorov, V. I. Ponomarenko, and A. S. Karavaev, Pis'ma Zh. Tekh. Fiz. **30** (2), 81 (2004) [Tech. Phys. Lett. **30**, 78 (2004)].

Translated by P. Pozdeev

The 1/*f* Spectrum of Acoustic Cavitation

V. P. Koverda*, A. V. Reshetnikov, V. N. Skokov, and A. V. Vinogradov

Institute of Thermal Physics, Ural Division, Russian Academy of Sciences, Ekaterinburg, 620219 Russia
* e-mail: koverda@itp.uran.ru
Received March 22, 2004

Abstract—The fluctuations of a response signal during acoustic cavitation in water in an ultrasonic field were studied by photometry of the transmitted laser radiation. In a broad range of frequencies, the spectral density of photocurrent fluctuations exhibits the 1/*f* behavior and their amplitude distribution function has a bimodal character. Coarsening of the scale of the experimental time series makes the bimodal character more pronounced and reveals the scale invariance of fluctuations. © *2004 MAIK "Nauka/Interperiodica".*

Many systems of both natural and technogenic origin feature stochastic processes in which low-frequency fluctuations account for a considerable fraction of energy. Mathematically, this is manifested by a power form, $S \sim 1/f^{\alpha}$, of the frequency dependence of the fluctuation power. The exact inverse proportionality of the power spectral density to the frequency ($\alpha = 1$) is characteristic of the voltage drop fluctuations observed for an electric current passing in a resistor [1]. Such processes have been studied in radiophysics for a long time. The interaction of nonequilibrium phase transitions in thermal systems also gives rise to fluctuations with a power spectral density proportional to 1/*f* [2–5]. In this case, the fluctuations are not small and their amplitude is sometimes comparable to the average signal. Despite extensive investigations devoted to the 1/*f* spectra, the question concerning a single origin of such spectra and the possible mechanism of generation of the scale-invariant fluctuations is still under discussion. A single source of the 1/*f* fluctuations during phase transitions was experimentally established for the local crisis of nitrogen boiling on the surface of a current-carrying superconducting film [2].

According to the phenomenological theory of 1/*f* fluctuations [2–5], the 1/*f* spectrum arises as a result of the interaction of various nonequilibrium phase transitions. The simplest stochastic equations describing the dynamics of fluctuations in a discrete system are as follows:

$$\begin{aligned}
\frac{\partial \phi}{dt} &= -\phi \psi^2 + \psi + \Gamma_1(t), \\
\frac{\partial \psi}{\partial t} &= -\phi^2 \psi + 2\phi + \Gamma_2(t),
\end{aligned} \qquad (1)$$

where ϕ, ψ are the dynamic variables and $\Gamma_1(t)$, $\Gamma_2(t)$ are the Gaussian δ-correlated noises with identical dispersions. Note that the coefficient 2 at ϕ in the second

equation makes the two equations in system (1) nonequivalent. System (1) can generate stationary stochastic processes $\phi(t)$ and $\psi(t)$ with power spectra obeying the 1/*f* and 1/*f²* laws, respectively. The function $\chi_i = \psi_i/(\varepsilon + \psi_i^2)$ (inverse with respect to ψ_i), where ε is a small parameter, also has a spectrum of the 1/*f* type. The theory of fluctuation processes with 1/*f* power spectra for nonequilibrium phase transitions shows that ψ_i is a scale-invariant function.

The probability density distribution $P(\chi_i)$ has two maxima (bimodal shape) and is described by the formula [5]

$$P(\chi_i) = C\chi^2 \exp\left(-\frac{|\chi_i|}{\sigma_\chi}\right), \qquad (2)$$

where σ_χ is the standard deviation and C is the normalization factor. If the time scale is increased by averaging over a certain time interval τ (called the scale transformation coefficient or scaling factor) according to the equation

$$y_j^{(\tau)} = \frac{1}{\tau} \sum_{i=\tau j}^{\tau(j+1)-1} x_i, \quad 0 \le j \le N/\tau, \qquad (3)$$

where x_i is the stochastic variable (ϕ_i or χ_i), the Gaussian distribution for the stochastic process $\phi(t)$ tends to $P(\chi)$ and acquires an exponential character typical of the statistics of extremal fluctuations (2).

It should be noted that the behavior of the distribution function for the nonequilibrium phase transitions differs from that for the turbulent pulsations. In the latter case, coarsening of the time scale leads to the Gaussian character of distribution (see, e.g., [6]). The above results refer to the case of a single source of 1/*f* fluctuations. During scaling transformations of the ensemble

of sources, the Gaussian character of distribution of the averaged time series is retained by virtue of the central limit theorem. Such cases are most frequently encountered in experiment. Scaling transformations of the distribution functions of experimentally measured fluctuations in the case of nonequilibrium phase transitions of various origins are of considerable interest from the standpoint of determining the source and elucidating the mechanism of formation of the 1/*f* spectrum.

This paper presents the results of experimental investigation of 1/*f* fluctuations during acoustic cavitation in water. Both theoretical and experimental investigations of the phenomenon of acoustic cavitation [7–9] show that the complicated character of the interactions between cavitation pockets and between these pockets and acoustic waves in a cell may lead to bistability and to transitions between stationary states. Such transitions in the cavitation cloud can be considered as nonequilibrium phase transitions in the complicated system of interacting cavitation pockets and acoustic waves. The stationary stochastic process involving such nonequilibrium phase transitions in the acoustic field may have a spectrum of the 1/*f* type.

The experiments were performed using a standard magnetostrictive source of ultrasonic oscillations with a frequency of 22 kHz. The radiator was placed into an optical cell filled with water. An increase in the radiator power to a certain level led to the appearance of cavitation. Variation of the radiator frequency gave rise to resonance phenomena enhancing cavitation. The integral spectra of the power of fluctuations in the cell were measured using a piezoelectric sensor. In the low-frequency range, the spectra were typical of white noise (with uniform distribution of the power over frequencies). The fluctuations of current measured in the radiator coils also had the form of white nose.

Substantially different results were obtained by laser probing of cavitation pockets in the cell, which is related to the more local character of this probe. The laser beam was passed through the cell, the transmitted light intensity was measured using a photodiode, and the response signal was digitized by an analog-to-digital converter and fed to a computer for recording and processing.

The spectra of the stochastic process accompanying cavitation were obtained by probing various regions of the cavitation cloud with the laser beam. The results only weakly depended on the region probed. In the initial stage of cavitation, the spectrum of photocurrent fluctuation power in the low-frequency range had (like the acoustic emission spectrum) a shape typical of white noise. An increase in the radiator power led to a sharp growth in the intensity of fluctuations, while some variation of the frequency was accompanied by transitions between two levels of these oscillations.

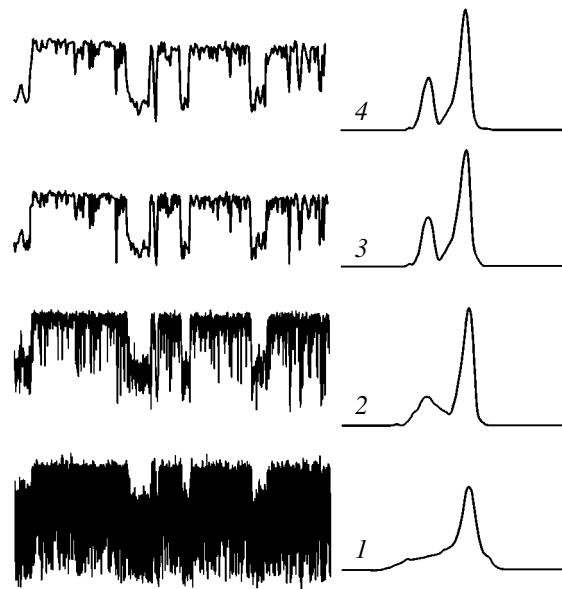Figure 1 presents the typical experimental time series and the corresponding distribution (*1*) of the

Fig. 1. Initial (*1*) and coarsened (*2–4*) time series and the corresponding distribution functions of photocurrent fluctuation amplitudes for the scaling factor $\tau = 1$ (*1*), 30 (*2*), 100 (*3*) and 200 (*4*).

oscillation amplitudes. The bimodal character of the distribution function was clearly revealed by scaling transformations of the fluctuations. Coarsened time series were obtained by averaging the experimental patterns over a certain time interval τ according to formula (3), where the stochastic variable was represented by the photocurrent intensity. For the first scale, the coarse time series represents the initial one. The length of each subsequent coarse time series decreases by a factor of τ, that is, contains N/τ points. Figure 1 shows a sequence of such coarsened time series and the corresponding distribution functions (*2–4*). As the scaling factor increases, both the coarse time series and the distribution functions become alike (cease to depend on τ). In other words, the amplitude distribution becomes scale invariant in agreement with the theoretical model [5]. It should be noted that the presence of short-wavelength high-amplitude peaks as such does not influence the scale invariance and the 1/*f* behavior of power spectra, because these components account for a very small fraction of energy.

Figure 2 shows the power spectrum of fluctuations in the transition regime of cavitation. As can be seen, the spectrum exhibits the 1/*f* behavior for the power varying over four orders of magnitude.

In conclusion, the acoustic cavitation in water features a regime characterized by the 1/*f* behavior of the power spectral density and by a bimodal distribution of the amplitude of fluctuations. Coarsening of the scale of the time series leads to scale-invariant distributions. The obtained results agree with theoretical notions
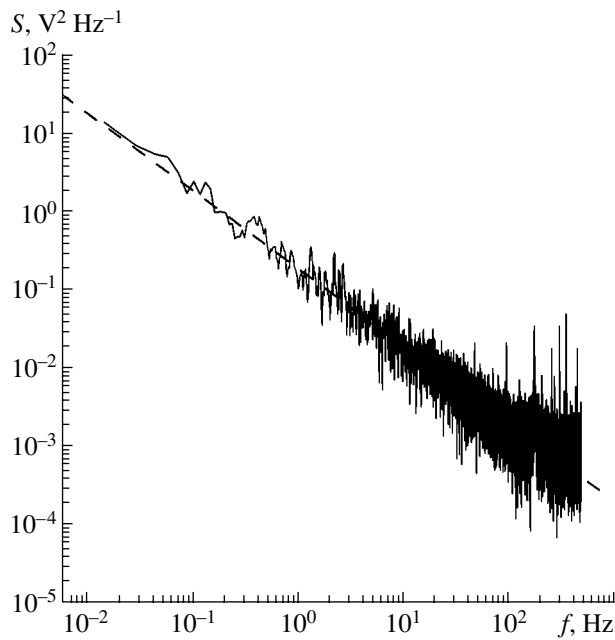
S, V^2 Hz^{-1}

Fig. 2. The power spectrum of photocurrent fluctuations (dashed line corresponds to the 1/f dependence).

about the generation of 1/f fluctuations during nonequilibrium phase transitions.

REFERENCES

1. Sh. M. Kogan, Usp. Fiz. Nauk **145**, 285 (1985) [Sov. Phys. Usp. **28**, 170 (1985)].

2. V. P. Koverda, V. N. Skokov, and V. P. Skripov, Zh. Éksp. Teor. Fiz. **113**, 1748 (1998) [JETP **86**, 953 (1998)].

3. V. N. Skokov, V. P. Koverda, A. V. Reshetnikov, *et al.*, Int. J. Heat Mass Transf. **46**, 1879 (2003).

4. V. P. Koverda and V. N. Skokov, Dokl. Akad. Nauk **386**, 187 (2002) [Dokl. Phys. **47**, 654 (2002)].

5. V. P. Koverda and V. N. Skokov, Dokl. Akad. Nauk **393**, 184 (2003) [Dokl. Phys. **48**, 615 (2003)].

6. V. Carbone, R. Cavazzana, V. Antoni, *et al.*, Europhys. Lett. **58**, 349 (2002).

7. I. Akhatov, U. Parlitz, and W. Lauterborn, Phys. Rev. E **54**, 4990 (1996).

8. A. O. Maksimov and E. V. Sosedko, Pis'ma Zh. Tekh. Fiz. **29** (3), 40 (2003) [Tech. Phys. Lett. **29**, 102 (2003)].

9. G. N. Sankin and V. S. Teslenko, Dokl. Akad. Nauk **393**, 362 (2003) [Dokl. Phys. **48**, 665 (2003)].

Translated by P. Pozdeev

The Characteristics of Layers for Stratified Luneberg Lens

S. V. Kuzmin

St. Petersburg State Polytechnic University, St. Petersburg, 195251 Russia
e-mail: kuzminsv@pochtamt.ru
Received March 29, 2004

Abstract—The dependence of characteristics of a stratified Luneberg lens on the layer parameters has been studied in numerical experiments using a mathematical model based on the rigorous solution of the electrodynamic problem of diffraction on a multilayer sphere. © 2004 MAIK "Nauka/Interperiodica".

Manufacturing a classical Luneberg lens with a continuous radial refraction index profile encounters considerable difficulties. For this reason, it is a common practice to use such antennas with stepped rather than continuous index profiles [2–6].

This paper presents the results of numerical experiments using the mathematical model of a multilayer (stratified) Luneberg lens developed in [3–8]. Obviously, the characteristics of such a system depend on the parameters of layers. Below, we will consider the role of the following factors:

(i) Deviations of the permittivity of layers from the calculated values.

(ii) The number of layers (it was established that even a small number of layers is sufficient to provide that the characteristics of a stratified lens would be virtually identical to those of an analogous continuous system [2, 3]).

(iii) The method of subdivision into layers.

(iv) Dielectric losses in the lens material. The consideration is based on the known dependence of the antenna gain on its diameter for various values of the loss tangent $\tan\delta$ [3]. This dependence has a maximum because the gain is proportional to $\exp\{-D\tan\delta\}$, where D is the antenna diameter. It was demonstrated [3] that losses compensate for an increase in the directivity.

The analysis will be applied to an antenna with the following parameters: relative diameter, $D/\lambda = 10$; distance from the lens center to feed, $b = 1.1D/2$; feed radiation pattern, $\exp\{-3.12 \times 10^{-4}\vartheta^2\}$; feed field intensity level at the lens edge ($\vartheta = 65°$), 0.26 (for the maximum antenna gain [3]); permittivity of the lens material, $\varepsilon' = 2.55$; and loss tangent of the lens material, $\tan\delta = 10^{-3}$.

In the classical Luneberg lens, the refraction index has a continuous radial profile and is equal to unity at the lens edge. In a real lens, the index at the edge is greater than unity. For this reason, the Luneberg lens is considered as comprising a sphere of radius a with a continuous index profile $\left(\dfrac{a}{D/2} = \dfrac{1}{\sqrt{\varepsilon_1}}\right)$, where ε_1 is the permittivity at the lens edge) and a homogeneous outer layer [1] (in our example, $\varepsilon_1 = 1.1$). The continuous part is subdivided into layers. We will consider three approaches to this subdivision:

(1) The index profile is divided into equal parts with respect to n ($n = \sqrt{\varepsilon}$), so that the radii of sequential layers are $r_1, r_2, \ldots, r_{nl-1} = a$ (nl is the number of layers), and each layer is divided into halves. The index of each layer is determined as the average, $n_i = n(r_{i-1} + 0.5(r_i - r_{i-1}))$, which yields a subdivision uniform with respect to the refraction index n.

(2) The permittivity profile is divided into equal parts with respect to ε, so that the radii of sequential layers are $r_1, r_2, \ldots, r_{nl-1} = a$, and each layer is divided into halves. The permittivity of each layer is determined as the average, $\varepsilon_i = \varepsilon(r_{i-1} + 0.5(r_i - r_{i-1}))$, which yields a subdivision uniform with respect to the permittivity ε.

(3) The lens is divided into layers of equal thickness, so that the radii of sequential layers are $r_1, r_2, \ldots, r_{nl-1} = a$, where $r_1 = r_2 - r_1 = r_3 - r_2 \ldots$. The permittivity of each layer is determined as the average, $\varepsilon_i = \varepsilon(r_{i-1} + 0.5(r_i - r_{i-1}))$, which yields a subdivision uniform with respect to the radius.

Since the dielectric losses depend on the permittivity, it is convenient to introduce the effective permittivity and effective loss tangent [3]:

$$\varepsilon_{\text{eff}} = \varepsilon'_{\text{eff}}(1 - i\tan\delta_{\text{eff}}),$$

$$\tan\delta_{\text{eff}} = \frac{n'}{\sqrt{\varepsilon'_{\text{eff}}}}\frac{\sqrt{\varepsilon'_{\text{eff}}} - 1}{n' - 1}\tan\delta,$$

where $n' = \sqrt{\varepsilon'}$ and $\varepsilon'_{\text{eff}}$ is the permittivity of a given layer. In contrast to [5, 6], we take into account the
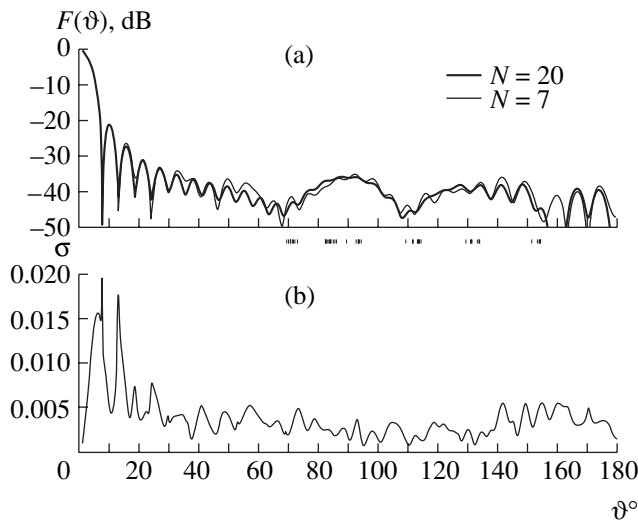
Fig. 1. (a) The radiation patterns of two stratified Luneberg lenses and (b) the standard deviation of the radiation patterns (in the E-plane) of the antennas with $N = 7$ made of a material with and without permittivity errors.

properties of a real insulator (penopolystyrene) used for manufacturing such antennas. The smaller the permittivity (the greater the relative volume of air in the lens material), the lower the level of losses.

For a lens with the given diameter, it is sufficient to take five to seven layers [2, 3]. The results of numerical experiments using different methods of subdivision and various numbers N of layers are presented in the table, where $b/(D/2)$ is the distance to the feed in relative units, G is the antenna gain (with allowance for dielectric losses), AE is the aperture efficiency (in relative units), and FSL is the first side lobe level (upper, E-plane; lower, H-plane). The experimental procedure involved focusing of the antenna. A criterion was min-

imization of the FSL level. Each variant was characterized by radiation patterns in the E- and H-planes.

Let us consider the variants with various N. For $N = 20$, the radiation patterns are independent of the method of subdivision and virtually coincide. This pattern will be considered as the reference. In the analysis of other cases, we will compare the behavior in three regions: (A) forward radiation (0°–65°), (B) side radiation (65°–115°), and (C) backward radiation (115°–180°).

$N = 8$. In the case of subdivision with respect to n, the radiation pattern is distorted, especially in regions B and C. The subdivision with respect to r gives good results in the regions A and C, but the level of side lobes in region B is 10 dB greater than that in the reference pattern. The best result is provided by the subdivision with respect to ε, for which the radiation pattern differs from the reference only in several points.

$N = 7$. The subdivision with respect to n leads to significant differences of the radiation pattern from the reference only in region C. For the subdivision with respect to r and ε, the situation is practically the same as above.

$N = 6$ and 5. For all variants of subdivision, the radiation patterns exhibit considerable distortions in region A (which are somewhat lower in the case of subdivision with respect to ε).

In all cases, the radiation patterns are more significantly distorted in the H-plane, which is related to a difference in the coefficients of reflection from interfaces for various polarizations.

Based on the data presented in the table and taking into account the above considerations, we may select for further investigation the lens consisting of seven layers uniform with respect to ε. Figures 1a and 2a show the radiation patterns of this lens in comparison to the reference.

Characteristics of N-layer Luneberg lenses determined in numerical experiments using different methods of subdivision into layers

	Subdivision uniform with respect to n				Subdivision uniform with respect to ε				Subdivision uniform with respect to r			
	$\dfrac{b}{D/2}$	G, dB	AE	FSL, dB	$\dfrac{b}{D/2}$	G, dB	AE	FSL, dB	$\dfrac{b}{D/2}$	G, dB	AE	FSL, dB
5	1.14	29.36	0.87	−21.2 −21.9	1.13	29.38	0.88	−21.2 −21.9	1.1	28.63	0.74	−21.8 −22.1
6	1.12	29.41	0.88	−21.2 −21.7	1.11	29.40	0.88	−21.2 −21.6	1.1	29.00	0.81	−21.7 −22.3
7	1.11	29.44	0.89	−21.2 −21.4	1.11	29.43	0.89	−21.1 −21.6	1.1	29.23	0.85	−21.5 −22.1
8	1.11	29.33	0.87	−20.9 −21.0	1.1	29.45	0.89	−21.2 −21.4	1.1	29.38	0.88	−21.4 −21.7
20	1.1	29.47	0.90	−21.4 −21.4	1.1	29.47	0.90	−21.4 −21.4	1.1	29.47	0.90	−21.4 −21.4

THE CHARACTERISTICS OF LAYERS FOR STRATIFIED LUNEBERG LENS
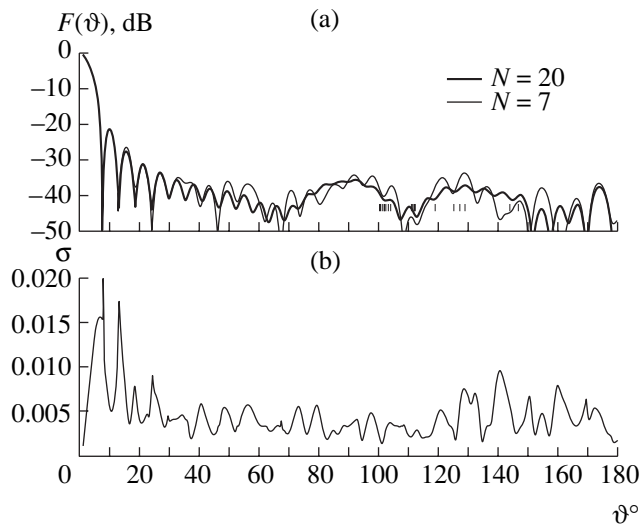

Fig. 2. (a) The radiation patterns of two stratified Luneberg lenses and (b) the standard deviation of the radiation patterns (in the *H*-plane) of the antennas with $N = 7$ made of a material with and without permittivity errors.

In the synthesis of a material for the lens, deviations of the real permittivity from the required value are unavoidable. For this reason, it is necessary to study the influence of such errors on the radiation pattern. For example, let us consider the case when the error is uniformly distributed and the layer permittivity ε_i' is set as follows: $\varepsilon_i + \Delta_i > \varepsilon_i' > \varepsilon_i - \Delta_i$, where ε_i is the preset value and $\Delta_i = 0.02\varepsilon_i$. In the numerical experiment, the radiation patterns were constructed for 20 various realizations of the radial permittivity profile (with focusing of the antenna). It was established that the optimum distance from the lens center to the feed (focal distance) varied within small limits, $b = 1.11 \pm 0.02D/2$, the average gain was $G = 29.35$ dB (862.04 ± 0.55 a.u.), and the average aperture efficiency value was $\nu = 0.87 \pm 0.03$ a.u. The average radiation pattern practically coincided with that of a lens made of a perfect material.

Figures 1b and 2b show the angular dependence of the standard deviation of the radiation pattern of an antenna made of a material with errors from the pattern of the lens made of a perfect material [9, formula (14.2.14)].

When constructing a stratified Luneberg lens of a different diameter or made of a different material, it is necessary to reproduce the investigation described above. Optimization of the layer parameters significantly reduces the cost of the antenna. Depending on the level of requirements for the lens characteristics, it is possible to reduce the number of layers and/or use a material with a higher level of losses and reduced level of requirements with respect to errors in the permittivity.

Acknowledgments. The author is grateful to Prof. D.V. Shannikov for valuable advice and for his help in preparation of this paper.

REFERENCES

1. S. P. Morgan, J. Appl. Phys. **29**, 1358 (1958).
2. J. R. Sanford, IEEE Antennas Propag. Mag. **37**, 76 (1995).
3. D. V. Shannikov and S. V. Kuzmin, in *Proceedings of the 1st IEEE International Conference on Circuits and Systems for Communications, St. Petersburg, 2002.*
4. D. M. Sazonov and N. Ya. Frolov, Zh. Tekh. Fiz. **35** (6), 763 (1965) [Sov. Phys. Tech. Phys. **10**, 990 (1965)].
5. J. R. Sanford, IEEE Trans. Antennas Propag. **42**, 690 (1994).
6. A. B. Vedenskiĭ, E. B. Zakharov, A. I. Skorodumov, and Yu. Ya. Kharlanov, Radiotekh. Élektron. (Moscow) **36** (4) (1991).
7. G. T. Markov and A. F. Chaplin, *Excitation of Electromagnetic Waves* (Énergiya, Moscow, 1967) [in Russian].
8. D. V. Shannikov and S. V. Kuzmin, Pis'ma Zh. Tekh. Fiz. **29** (22), 39 (2003) [Tech. Phys. Lett. **29**, 941 (2003)].
9. E. S. Venttsel', *The Theory of Probabilities* (Vysshaya Shkola, Moscow, 1998) [in Russian].

Translated by P. Pozdeev

TECHNICAL PHYSICS LETTERS   Vol. 30   No. 11   2004

Synthesis and Structural Characterization of a Heterocomposition Based on Porous Layers of SiC Polytypes

L. M. Sorokin, G. N. Mosina, A. S. Tregubova, A. A. Lebedev,
N. S. Savkina, and V. B. Shuman

Ioffe Physicotechnical Institute, Russian Academy of Sciences,
St. Petersburg, 194021 Russia

Received June 22, 2004

Abstract—We have studied the structure of transverse cross sections of a heterocomposition consisting of porous layers of silicon carbide polytypes (substrate 6H-SiC/por-6H-SiC/epi-3C-SiC/por-3C-SiC). The epitaxial layer of 3C-SiC polytype (epi-3C-SiC) was grown by sublimation in vacuum on the surface of a porous 6H-SiC sublayer (por-6H-SiC) obtained by electrochemical etching of a 6H-SiC substrate. The boundary between the 3C-SiC epilayer and the porous 6H-SiC sublayer contains no defective transition layer, and the 3C-SiC epilayer is free of dislocations. © *2004 MAIK "Nauka/Interperiodica"*.

Silicon carbide (SiC) is known to be a polytype material, 4H-SiC and 6H-SiC being the most widely occurring and thoroughly studied polytypes. Since the commercially available SiC single crystals still contain a large number of micropipes and dislocations, the formation of high-quality epitaxial layers suitable for device applications on this basis is still problematic.

From the standpoint of modern electronics, the most attractive material is the cubic modification of silicon carbide (3C-SiC) characterized by higher mobilities of electrons and holes in comparison to the other polytypes. Unfortunately, the use of cubic silicon carbide for basic research and semiconductor technology is limited because of the absence of methods capable of providing for the growth of 3C-SiC polytype of high quality in sufficient amounts. Investigations are mostly performed on single crystal 3C-SiC epilayers grown on silicon or 6H-SiC substrates. In the latter case, however, it is difficult to obtain a sharp interface between the two polytypes, which is a necessary condition for high-quality heterostructures [1].

In recent years, much effort has been devoted to investigations of the optical and electrical properties of porous layers formed by electrochemical etching of 4H- and 6H-SiC polytypes, which are characterized by increased photoluminescence [2–5].

It can be assumed that electrochemical etching under certain conditions can lead to the removal of some structural defects, such as dislocations, micropipes, and composition inhomogeneities, which opens ways to using these etched surfaces for the subsequent growth of epilayers with a lower density of defects as compared to the initial substrates. In particular, previously [6, 7] we demonstrated that single crystal epilay-

ers can be obtained on a porous surface of 6H-SiC polytype. The fact that the porous material was depleted of silicon at the inner surfaces of pores had no negative effect on the epilayer, whose composition insignificantly deviated from stoichiometry only in the vicinity of the interface [8].

There have been several publications devoted to the structure of porous 3C-SiC layers [9–11]. However, the porous material was in all cases formed in 3C-SiC layers grown on silicon substrates. To our knowledge, no data were reported on the structure of porous 3C-SiC layers formed on SiC substrates. In addition, it would be of interest to study the structure of the boundary between the porous 6H-SiC and epitaxial 3C-SiC layers. This system admits the formation of 3C-SiC microinclusions (quantum dots) inside the 6H-SiC layer. Such structures are of considerable basic and applied interest in view of the development of novel optoelectronic devices.

In this context, our investigations were aimed at obtaining an epilayer of the cubic modification of silicon carbide (epi-3C-SiC) on a porous silicon carbide (por-6H-SiC) sublayer on the Si-side of a single crystal 6H-SiC substrate, followed by electrochemical etching of the epilayer with the formation of an outer porous (por-3C-SiC) layer. In this study, we have used X-ray topography and transmission electron microscopy (TEM) to characterize the structure of the following heterocomposition: 6H-SiC substrate (thickness, ~250 μm)/por-6H-SiC (~20 μm)/epi-3C-SiC (14 μm)/por-3C-SiC (7 μm).

The samples were prepared using Lely-grown 6H-SiC substrates with a low density of basal dislocations (~10^{-1} cm^{-2}), as determined from X-ray topo-

grams measured using CuK_α radiation for $(11\bar{2}0)$ reflections in the transmission mode. The porous layers were obtained using the following procedure. The first porous layer was formed on the Si-side of a single crystal 6H-SiC substrate (initial concentration of uncompensated donors, 8.5×10^{17} cm^{-3}) by electrochemical etching in an HF–H_2O–C_2H_5OH (1 : 1 : 2) electrolyte solution for 15 min at a current density of 20 mA/cm^2. The thickness of this porous layer, determined by examining a cleaved substrate in a scanning electron microscope, was 18.2 ± 0.1 µm. The gravimetric porosity was $18.5 \pm 0.5\%$. Then, a 3C-SiC epilayer was grown above the porous layer by sublimation in vacuum at 1800°C at an excess pressure of silicon. The layer thickness determined using the interference pattern in the reflection spectrum of the epilayer was 13.7 ± 0.3 µm. The second (outer) porous layer was obtained by electrochemical etching of the epilayer at the same current density (20 mA/cm^2), but for a shorter period of time (5 min).

The structural perfection of the epilayer was characterized by X-ray backscattering using CuK_α radiation. An analysis of the topograms measured in the (311) and (331) reflections showed that the epilayer grown on the porous Si-side of 6H-SiC has a structure of 3C-SiC comprising twinned regions misoriented by 60°. In the X-ray topograms (Fig. 1), these regions are manifested by the opposite contrast: dark (*B*) against bright (*A*). The twinned regions had various dimensions, and it was possible to find twins with an area of several square millimeters. The twinned regions consisted of small twin lamellae and stacking faults typical of 3C-SiC epilayers (in Fig. 1, these defects can be observed in the bright *A*-regions). The twinned structure of 3C-SiC epilayers was originally reported in [12].

The transverse sections $(11\bar{2}0)$ of the heterocomposition were studied by TEM. In order to prepare the sample with a $(11\bar{2}0)$-cut surface relative to the hexagonal substrate, the heterocomposition was oriented in a DRON-3 diffractometer so as to determine the azimuthal direction, in which the cut was made with a diamond disk. Subsequent sample preparation followed the conventional procedure, including gluing two cuts together with their epitaxial surfaces in contact, sequential grinding with various abrasive powder fractions to a thickness of 30–40 µm, and final ion-beam thinning until the appearance of perforation sites.

The results of our structural investigations were as follows. The patterns of microdiffraction from the transverse sections with hexagonal and cubic structures confirmed that the cut was made via a $(11\bar{2}0)$ plane relative to the hexagonal substrate. A continuation of this plane in the cubic epilayer was the $(11\bar{2})$ plane, which implied that a (111)-oriented epilayer was grown on a (0001) surface of the substrate.
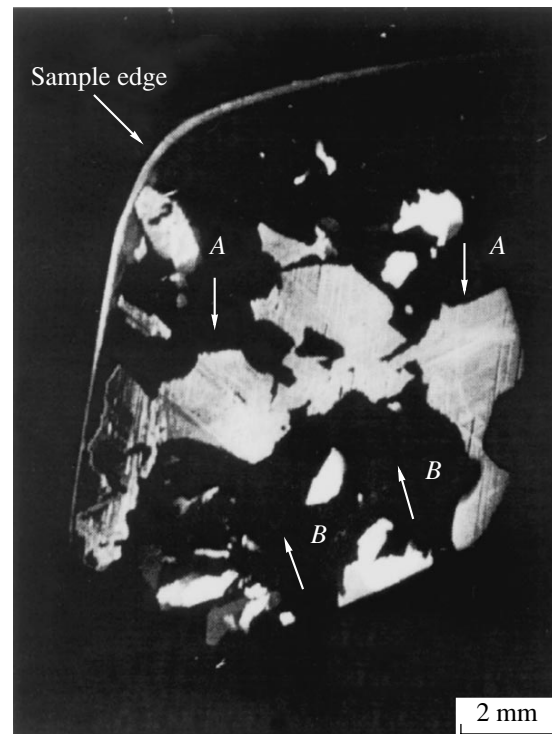

Fig. 1. X-ray topogram in the backscattering mode for the asymmetric (311) reflection from a 3C-SiC epilayer grown on a porous layer of the 6H-SiC(0001) substrate. Bright areas (*A*) correspond to the regions of the 3C-SiC epilayer occurring in the reflecting position, while dark areas (*B*) represent the regions of twinned orientation. The bands observed in the bright areas reflect the presence of stacking faults in the epilayer.

Of special interest was the structure of the upper part (~0.5-µm-thIck) of the porous 3C-SiC layer (Fig. 2). This layer was strongly inhomogeneous and exhibited peculiarities previously observed both in transverse sections [13, 14] and on planar samples [14] of the 6H-SiC substrates with porous 6H-SiC layers. It was suggested [13, 14] that these peculiarities correspond to the sites of the onset of active interaction between electrolyte and silicon carbide surface upon voltage application to the electrochemical cell. The appearance of these peculiarities is probably related to the presence of structural detects on the initial substrate surface. The regions of bright contrast in the electron micrographs (Fig. 2) correspond to channels (pores) formed as a result of the electrochemical etching. The pores form a fanlike structure, in which the outer pores are oriented at a small angle relative to the surface of the porous layer. The minimal angle between inner pores is ~60°. At a distance of about 1.5 µm from the surface, the inner pores sharply change their orientation (the angle between outer and inner pores is ~120°) to form a fanlike pattern of rays converging downward. At a depth of ~2.5 µm, the pores change the orientation again, but their subsequent propagation in depth does not exhibit any clear orientation. Only near the boundary between
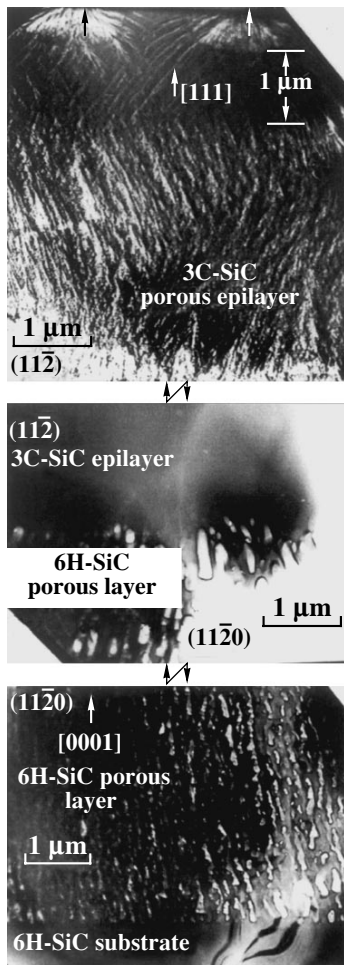
Fig. 2. Electron micrographs showing the structure of all regions in the cross section of the heterocomposition studied (substrate, first porous layer, epilayer, second porous layer). Note zig-zag changes in the direction of pores (channels) in the 3C-SiC epilayer (top image). Arrows indicate the sites of preferred pore nucleation.

the porous and epitaxial 3C-SiC layers (~0.3 μm from the por-3C-SiC/epi-3C-SiC interface) are the channels again aligned in the [111] direction (perpendicular to the interface and parallel to the current lines during the anodic etching).

The remaining part of the 3C-SiC layer (below the outer porous layer) has a quite homogeneous single crystal structure. We did not observe any defects in this layer. The structure of the porous 6H-SiC sublayer (on which the 3C-SiC epilayer was grown) is close to a structure described previously [8]. The boundary between the 3C-SiC epilayer and the porous 6H-SiC sublayer is not sharp and exhibits a wavy character. Within a 1- to 1.5-μm-thick layer, pores extended in the direction perpendicular to the interface are significantly greater (in the average size) compared to pores in the remaining part of the porous 6H-SiC layer. This peculiarity of the porous layer at the boundary with the epilayer is explained by sublimation etching taking place

prior to the epitaxial growth. A part of the porous layer is sublimed and pores in the remaining layer are probably etched and increased in size. In the remaining part of the porous 6H-SiC sublayer, the pores are rather strictly aligned in the [0001] direction, that is, perpendicularly to the boundary between this layer and the 6H-SiC substrate (i.e., parallel to the current lines during the first anodic etching). The interface between the porous 6H-SiC layer and the substrate is very sharp, in agreement with the results of all electron-microscopic investigations of such boundaries.

It should be noted that, in the case when the 3C-SiC epilayer is grown immediately on a hexagonal 6H-SiC substrate (without porous interlayer), it is difficult to avoid the formation of a transition region comprising alternating layers of the two (6H-SiC and 3C-SiC) polytypes [15]. As is known, epitaxial growth of the 3C-SiC polytype on a 6H-SiC substrate surface is performed in the presence of excess silicon in a growth reactor. Even small deviations from this condition lead to unstable growth of the 3C-SiC polytype because the energies of formation for the two polytypes are close. Apparently, the presence of inhomogeneities on the substrate surface may also favor unstable growth of the 3C-SiC polytype. As a result, there appears an intermediate layer consisting predominantly of 6H-SiC with uniformly distributed islands of the 3C-SiC polytype. Evidently, by controlling the ratio of silicon and carbon in the reactor during epitaxial growth by sublimation in vacuum, it is possible to obtain structures with quantum dots of the 3C-SiC polytype.

In conclusion, it should be noted that the main structural feature of the porous layer of 3C-SiC, in contrast to the porous layer of 6H-SiC, is the direction of pore propagation in depth of the layer. In the 6H-SiC polytype, the pores are aligned in the [0001] direction parallel to the current lines in the etching stage, whereas the direction of pores propagating in depth of the 3C-SiC polytype initially deviates from the current lines. The structure of 3C-SiC has three physically equivalent {111} planes, which are not perpendicular to the (111) surface of the epilayer. As a result, preferred etching may proceed along these planes, rather than along the normal to the sample surface.

Thus, we demonstrated the possibility of obtaining 3C-SiC epilayers with highly perfect structures on porous 6H-SiC sublayer on the Si-side of a single crystal 6H-SiC substrate. The electron-microscopic examination of the porous 3C-SiC layer showed that the character of pore propagation in depth of this layer differs from that in the 6H-SiC polytype. In 3C-SiC, the direction of pore alignment into channels down to a depth of 2–3 μm deviates from the current lines perpendicular to the sample surface.

REFERENCES

1. A. A. Lebedev, G. N. Mosina, I. P. Nikitina, *et al.*, Pis'ma Zh. Tekh. Fiz. **27** (24), 57 (2001) [Tech. Phys. Lett. **27**, 1052 (2001)].

2. J. S. Shor, I. Grimberg, B. Z. Weiss, and B. D. Kutz, Appl. Phys. Lett. **62**, 2836 (1993).

3. T. Matsumoto, J. Takahashi, T. Tamaki, *et al.*, Appl. Phys. Lett. **64**, 226 (1994).

4. A. O. Konstantinov, C. I. Harris, and E. Jansen, Appl. Phys. Lett. **65**, 2699 (1994).

5. A. O. Konstantinov, A. Henry, C. I. Harris, and E. Jansen, Appl. Phys. Lett. **66** (17), 2250 (1995).

6. N. A. Mynbaeva, N. S. Savkina, A. Zubrilov, *et al.*, Mater. Res. Soc. Symp. Proc. **587**, 08.6.1 (2000).

7. N. S. Savkina, V. V. Ratnikov, A. Yu. Rogachev, *et al.*, Fiz. Tekh. Poluprovodn. (St. Petersburg) **36**, 812 (2002) [Semiconductors **36**, 758 (2002)].

8. L. M. Sorokin, N. S. Savkina, V. B. Shuman, *et al.*, Pis'ma Zh. Tekh. Fiz. **28** (11), 23 (2002) [Tech. Phys. Lett. **28**, 935 (2002)].

9. A. Takazava, T. Tamura, and M. Yamada, Jpn. J. Appl. Phys. **32**, Part 1, 3148 (1993).

10. T. Monguch, H. Fujioka, K. Ono, *et al.*, J. Electrochem. Soc. **145**, 2241 (1998).

11. V. Lysenko, D. Barbier, and B. Champagnon, Appl. Phys. Lett. **79**, 2366 (2001).

12. A. N. Andreev, N. Yu. Smirnova, A. S. Tregubova, *et al.*, Fiz. Tekh. Poluprovodn. (St. Petersburg) **31**, 285 (1997) [Semiconductors **31**, 232 (1997)].

13. W. Shin, T. Hikosaka, W.-S. Seo, *et al.*, J. Electrochem. Soc. **145**, 2456 (1998).

14. A. M. Danishevskii, M. V. Zamoryanskaya, A. A. Sitnikova, *et al.*, Semicond. Sci. Technol. **13**, 1111 (1998).

15. N. S. Savkina, A. M. Strel'chuk, L. M. Sorokin, *et al.*, Mater. Sci. Forum **433**–**436**, 293 (2003).

Translated by P. Pozdeev

Obtaining X-ray Shadow Images
Using High-Resolution Enlargement Kumakhov Optics

A. Yu. Romanov* and V. N. Chernik

Institute for Roentgen Optics, Moscow, Russia
* e-mail: androm2@yandex.ru
Received April 27, 2004

Abstract—X-ray shadow images have been obtained using cone-shaped polycapillary structures of high-resolution Kumakhov optics. The proposed method develops a substantially new direction in X-ray microscopy. This technique does not require using expensive microfocus X-ray sources employed in the traditional X-ray imaging systems characterized by spatial resolution on a level of 5–6 μm. The images obtained in this study show resolution on a level of 1 μm. © 2004 MAIK "Nauka/Interperiodica".

In order to obtain images with spatial resolution on a micron level using the existing X-ray shadow imaging microscopes, it is necessary to use special expensive X-ray sources based on synchrotrons or microfocus X-ray tubes [1, 2]. This circumstance significantly increases the price and complicates the design of X-ray microscopes. One solution of this problem is offered by developing X-ray optical systems for microscopes based on Kumakhov optics [3–7]. This polycapillary optics provides for an increase in both contrast and resolution of X-ray images.

In contrast to the projection scheme of enlargement in air gap, where the resolution is determined by the source size, the resolution of a scheme employing capillary optics is determined for the most part by the entrance dimensions of capillaries. Using polycapillary structures in the optical scheme of a transmission microscope, it is possible to obtain X-ray images with a resolution on the level of two to three entrance diameters of the channel [5, 6].

Since the first experiments in polycapillary X-ray microscopy [5, 6], the technology of polycapillary structures has been significantly developed. This progress provides for a significant increase in the performance of X-ray microscopy schemes implementing the principles of Kumakhov optics. Therefore, it is expedient to study the possible applications of modern Kumakhov optics to high-resolution X-ray microscopy.

This paper presents the results of experiments showing the possibility of using high-resolution cone-shaped polycapillary structures of Kumakhov optics for obtaining X-ray shadow images.

The experimental optical scheme comprised an X-ray source, a test object, a polycapillary cone structure, and an X-ray image converter (Fig. 1). The operation of this scheme of X-ray microscopy is based on projecting an X-ray shadow image onto the entrance of a polycapillary cone structure with a large ratio of the

exit (D_k) and entrance (d_k) diameters: $M_k = D_k/d_k = 5–15$. The lattice of the entrance holes of the polycapillary structure divides the image into elements, thus forming an array. Each capillary accepts an element of the image and transfers it with enlargement to a detector (X-ray film or image converter). This provides for the first stage of image enlargement (in the X-ray range). This enlargement is determined by the ratio $M_0 = D_0/d_0$, where d_0 and D_0 are the entrance and exit diameters of the capillaries, respectively (note that $M_0 = M_k \equiv M$).

The cone function is to form and enlarge the image, improve the resolution, and increase the contrast. The length L and magnification M of the polycapillary cone structure are related to the focal distance f (a distance from the X-ray tube focus to the cone entrance) by the formula $f = L/(M - 1)$. For example, a structure with $M = 10$ and $L = 45$ mm has $f = 5$ mm. The imaged area is determined by the entrance area of the polycapillary cone structure.

On the existing level of technology developed at the Institute of X-ray Optics (Moscow), it is possible to obtain polycapillary cones with an entrance channel
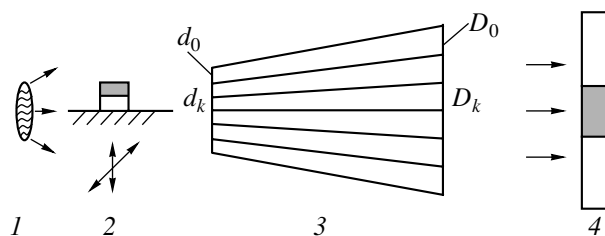

Fig. 1. Schematic diagram of the experimental arrangement: (*1*) focal spot of the X-ray tube; (*2*) test object; (*3*) polycapillary cone structure: (*4*) X-ray image converter.

diameter of $d_0 = 0.15$ μm and the ratio of the exit and entrance diameters $D_0/d_0 = 10$–15.

In these experiments, we used a polycapillary cone with an entrance channel diameter of $d_0 \approx 0.3$ μm and an exit diameter of $D_0 \approx 4.5$ μm. The whole assembled structure had an entrance diameter of $d_k = 0.3$ mm and an exit diameter of $D_k = 4.5$ mm, so that $M_k = 15$. Using this structure, it is possible to obtain a magnification of $M = 15$ in the X-ray optics tract. Previously, Nikitin [6] used a polycapillary cone structure with $d_0 = 0.8$ μm, $D_0 = 4$ μm, and $L = 23$ mm, for which $M = 5$.

The X-ray source was a microfocus tube (BS-13) of the transmission type with a copper anode and electromagnetic beam focusing operating in the regime of 2.5 W, 40 kV. The X-ray tube provided for a focal spot size of about 200 μm; the exposure duration was 10 s.

The X-ray pattern obtained at the polycapillary cone exit is converted into an optical image on the scintillation screen of the X-ray image converter. Then, the image of the object studied is further enlarged by a microobjective in the optical tract and the image brightness is enhanced in an electrooptical converter. Finally, the enlarged and enhanced image is detected by a CCD camera and converted into a digital form. The total resolution of the X-ray image converter in the phosphor-coated plane was ~5 μm.

The video image from the CCD camera is fed into a personal computer and processed using a program package with pixel accumulation, averaging, and division, after which the final enlarged image is displayed on the computer monitor.

Figure 2 shows the X-ray shadow image of a test object representing a 2-μm-thick tungsten plate on a 2.5-μm-high silicon pedestal protruding above a thick silicon plate. The silicon pedestal had a small thickness (~10 μm) in the direction of the X-ray beam, which explains the much lower contrast of the pedestal as compared to that of the ~0.5-mm-thick base silicon plate. The thickness of the tungsten sample in the X-ray beam direction was about 10 μm, which was sufficient for obtaining a good contrast. As can be seen in Fig. 2, the image displays clearly resolved details on a micron level, which agrees with theoretical estimates of the resolution ($R = 3d_0 = 0.9$ μm). The image also displays a network formed due to the polycapillary structure
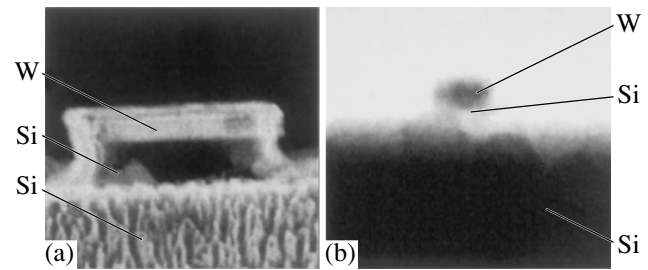

Fig. 2. Enlarged images of the test object (a) in the electron microscope and (b) in the X-ray shadow projector with high-resolution polycapillary Kumakhov optics.

walls. Methods aimed at eliminating this network at the computer processing stage are in progress.

Nikitin *et al.* [5] obtained images of two gold wires with a diameter of 10 μm spaced by 3 μm. However, an analysis of the obtained pattern allowed the real resolution to be evaluated at 1.5–2 μm. The images of the test object obtained in this study are directly indicative of the micron resolution. The results of our experiments indicate that the resolution can be further improved to reach a level on the order of 0.1 μm through optimization of the optical scheme and the characteristics of important components, in particular, the polycapillary cone structure.

REFERENCES

1. C. G. Schoer, J. Meyer, M. Kuhlmann, *et al.*, Appl. Phys. Lett. **81**, 1527 (2002).
2. S. C. Mayo, P. R. Miller, S. W. Wilkins, *et al.*, J. Microsc. **207**, 79 (2002).
3. M. A. Kumakhov and F. F. Komarov, Phys. Rep. **191**, 289 (1990).
4. S. B. Dabagov, Usp. Fiz. Nauk **173**, 1083 (2003) [Phys. Usp. **46**, 1053 (2003)].
5. A. N. Nikitin, N. S. Ibraimov, and S. V. Nikitina, Proc. SPIE **2859**, 227 (1996).
6. A. N. Nikitin, Proc. SPIE **3115**, 117 (1997).
7. A. Yu. Romanov, Izmer. Tekh., No. 7 (2004) (in press).

Translated by P. Pozdeev

Laser Photoacoustic Imaging of Inhomogeneous Objects

K. L. Muratikov

Ioffe Physicotechnical Institute, Russian Academy of Sciences, St. Petersburg, 194021 Russia
Received June 7, 2004

Abstract—The process of photoacoustic response formation in inhomogeneous objects is analyzed. In a quasi-static case, the photoacoustic image is formed predominantly due to inhomogeneities in the thermoelastic coupling coefficient. Expressions describing thermoelastic strains in an inhomogeneous object with allowance for the inhomogeneous thermoelastic coupling coefficient in the general form are obtained within the framework of a three-dimensional model using the perturbation theory. A comparative analysis is performed for the process of photoacoustic image formation in various regimes of piezoelectric sensor operation. The results are used to explain the behavior of a photoacoustic signal at the ends of vertical cracks. © 2004 MAIK "Nauka/Interperiodica".

Processes involved in the generation, propagation, and detection of thermal waves excited by laser radiation in inhomogeneous solids have received much attention (see, e.g., [1, 2]). The interest in studying these processes is related to the need for correct interpretation of the results obtained by methods of photoacoustic and photothermal microscopy. While the problems pertaining to photothermal microscopy have been studied in sufficient detail [3, 4], the situation in photoacoustic microscopy with piezoelectric signal detection is much less satisfactory. Interpretation of the results of photoacoustic experiments with a piezoelectric detector is usually based on the models of photoacoustic response formation developed for homogeneous objects [5]. An important distinctive feature of photoacoustic microscopy with piezoelectric signal detection, in comparison to photothermal microscopy, is the need to take into account thermoelastic strains arising in the probed object as a result of absorption of the laser radiation energy. It should be noted that no systematic analysis of the formation of photoacoustic piezoelectric response from inhomogeneous objects have been performed so far within the framework of a three-dimensional model.

In this context, the main aim of this study was to analyze the process of excitation of acoustic oscillations in inhomogeneous objects under the action of nonstationary laser radiation. In order to solve this task, it is necessary to determine nonstationary thermoelastic strains arising in a solid in the course of absorption of modulated laser radiation. In the general case, these strains can be described using the equations of motion [6],

$$\rho \frac{\partial^2 u_i}{\partial t^2} = \frac{\partial \sigma_{Ij}}{\partial x_j}, \qquad (1)$$

where ρ is the density of a given material, u_i are the components of the strain tensor, and σ_{ij} are the components of the stress tensor in the object.

In this study, the object is suggested to be inhomogeneous. Accordingly, the stress tensor components can be represented in the form usual for the analysis of thermoelasticity [6], with the coefficients of elasticity and thermoelastic coupling dependent on the coordinates. The inhomogeneity of the object is assumed to be weak, so that the Lamé elastic constants (λ and μ) and the thermoelastic coupling coefficient (γ) can be represented as $\lambda = \lambda_0 + \lambda_1$, $\mu = \mu_0 + \mu_1$, and $\gamma = \gamma_0 + \gamma_1$, where λ_0, μ_0, and γ_0 are the values of parameters characterizing the corresponding homogenous properties of the object and λ_1, μ_1, and γ_1 are small components describing the inhomogeneities inside the object. By virtue of the above assumptions, $\lambda_0 \gg \lambda_1$, $\mu_0 \gg \mu_1$, and $\gamma_0 \gg \gamma_1$.

Taking into account these conditions, the strain vector components Δu_i and the temperature variations ΔT in the object excited by nonstationary laser radiation can be also represented as $\Delta u_i = \Delta u_i^{(0)} + \Delta u_i^{(1)}$ and $\Delta T = \Delta T^{(0)} + \Delta T^{(1)}$, where $\Delta u_i^{(0)}$ and $\Delta T^{(0)}$ describe the strain and temperature distributions generated by laser radiation in the homogeneous object, while $\Delta u_i^{(1)}$ and $\Delta T^{(1)}$ correspond to the perturbations caused by inhomogeneities present in the object.

In accordance with the above assumptions, equations of motion (1) can be linearized with respect to $\Delta u_i^{(1)}$ and $\Delta T^{(1)}$. In addition, we will take into account that, in a broad range of frequencies, the lengths of acoustic waves in solids are much greater than the lengths of thermal waves. Even in materials with high thermal conductivities, this relation is valid up to frequencies on the order of 1 GHz. Therefore, the photoacoustic images formed within this frequency range are determined predominantly by thermal waves, since the images formed by the acoustic waves are poorly resolved. Within the framework of the model under

consideration, the analysis will be restricted to the case of objects homogeneous with respect to thermal properties. Then, we may assume that $\Delta T^{(1)} = 0$ and $\Delta T^{(0)}$ can be determined from the equation of heat conduction in a homogeneous object. Under the above assumptions, the left-hand side of Eq. (1) can be transformed so as to correspond to the linear equations of motion in a quasi-static form [6], while the right-hand side can be truncated so as to retain only terms of the type $\frac{\partial}{\partial x_i}(\gamma_1 \Delta T^{(0)})$.

In order to solve the obtained equations, it is necessary to set the boundary conditions. These conditions are usually formulated for a fixed or free boundary [6]. In this analysis, we will consider the formation of a response signal in the object with a fixed upper boundary. The Green function for the equations of motion in the infinite space in a quasi-static approximation was obtained in [6]. Using this result and the method of reflections [7], the Green function for a semi-infinite space with the boundary conditions $\Delta u_i|_{z=0} = 0$, which corresponds to the case of an object with a fixed upper boundary, can be represented in the following form:

$$G_{ik} = \frac{1+\sigma}{8\pi E(1-\sigma)}\left\{[(3-4\sigma)\delta_{ik} + n_i^{(-)}n_k^{(-)}]\frac{1}{r^{(-)}}\right.$$

$$\left. - [(3-4\sigma)\delta_{ik} + n_i^{(+)}n_k^{(+)}]\frac{1}{r^{(+)}}\right\}. \quad (2)$$

Here, σ is the Poisson coefficient, E is the Young modulus, and

$$r^{(\pm)} = \sqrt{(x-x')^2 + (y-y')^2 + (z \pm z')^2},$$

$$\mathbf{n}^{(\pm)} = \frac{(x-x', y-y', z \pm z')}{r^{(\pm)}}.$$

Once the Green function (2) is known, we can determine the components of the $\Delta u_i^{(1)}$ vector by the formula

$$\Delta u_i^{(1)} = -\int d^3r' G_{ik}(\mathbf{r}', \mathbf{r})\frac{\partial}{\partial x_k'}(\gamma_1(\mathbf{r}')\Delta T^{(0)}(\mathbf{r}')). \quad (3)$$

Expressions (3) correspond to the complete solution of the problem under consideration in the first order of perturbation theory. According to this, the photoacoustic image of an inhomogeneous object in our case is formed due to inhomogeneities in the thermoelastic coupling coefficient.

The expressions for $\Delta u_i^{(1)}$ can be simplified in the case when $z \gg |x - x_0|$ and $z \gg |y - y_0|$ (see figure). For
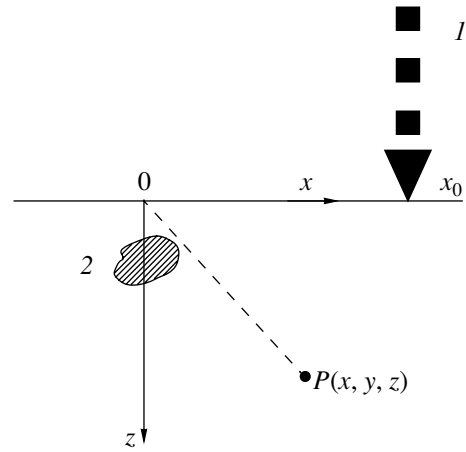
Geometry of photoacoustic imaging: (*1*) exciting laser radiation; (*2*) inhomogeneity in the probed object; $P(x, y, z)$ is the point of strain registration.

example, the strain components $\Delta u_x^{(1)}$ and $\Delta u_z^{(1)}$ are given by the formulas

$$\Delta u_x^{(1)} = \frac{1+\sigma}{2\pi E(1-\sigma)}\frac{1}{z^3}\int d^3r'(x-x')\gamma_1(\mathbf{r}')\Delta T^{(0)}(\mathbf{r}'),$$

$$\Delta u_z^{(1)} = \frac{1+\sigma}{\pi E}\frac{1}{z^2}\int d^3r'\gamma_1(\mathbf{r}')\Delta T^{(0)}(\mathbf{r}'). \quad (4)$$

Using these formulas, it is possible to determine the response signal detected by a piezoelectric sensor at a distance of z from the upper boundary. Depending on the oscillation mode excited in the piezoelement, the response signal ΔV can be proportional to $\frac{\partial \Delta u_z^{(1)}}{\partial z}$ or

$\left(\frac{\partial \Delta u_x^{(1)}}{\partial x} + \frac{\partial \Delta u_y^{(1)}}{\partial y}\right)$ [5, 8]. The latter expression refers to thin piezoelectric sensors exhibiting bending oscillations in the course of signal detection.

It is possible to show that, in accordance with formulas (4), the piezoelectric signals are determined to within a constant factor by the same expression. In the first case,

$$\Delta V_1 = C_1 \frac{1+\sigma}{\pi E}\frac{1}{z^3}\int d^3r'\gamma_1(r')\Delta T^{(0)}(r'), \quad (5)$$

where C_1 is a coefficient dependent on the piezoelectric sensor characteristics. Formula (5) presents the general solution of the problem under consideration in the first order of perturbation theory. As can be seen from this expression, the photoacoustic image is determined by inhomogeneities of the thermoelastic coupling coefficient. In order to calculate the photoacoustic signal

using formula (5), it is necessary to know the temperature distribution $\Delta T^{(0)}$ in the homogeneous object. The solution of this problem has been studied in a number of publications and is not considered here.

For the sake of illustration, the results obtained above can be applied to objects in which the inhomogeneities are caused by the initial strains. Within the framework of the proposed model, the dependence of $\gamma^{(1)}$ on the initial strains in the first order of perturbation theory can be represented as follows: $\gamma^{(1)} = \beta_0(U_{xx} + U_{yy} + U_{zz})$, where U_{ik} are the initial strain components and β_0 is a coefficient of proportionality.

An important application of the obtained expression for $\gamma^{(1)}$ is an analysis of the behavior of a photoacoustic signal at the ends of radial cracks. The conditions of photoacoustic signal formation in this case were considered previously [9–12]. It was established that, by determining the internal stresses via the initial strains, it is possible to find a relationship between the photoacoustic piezoelectric response and internal stresses. According to this approach, the photoacoustic signal ΔV_1 can be represented in terms of formula (5) as

$$\Delta V_1 = C_1\beta_0\frac{1-\sigma^2}{\pi E^2}\frac{1}{z^3}\int d^3 r'(\sigma_{xx}^{(r)}(r') + \sigma_{yy}^{(r)}(r'))\Delta T^{(0)}(r'), (6)$$

where $\sigma_{xx}^{(r)}$ and $\sigma_{yy}^{(r)}$ are components of the internal stress tensor. Using explicit expressions for the stress tensor components $\sigma_{xx}^{(r)}$ and $\sigma_{yy}^{(r)}$ [12], formula (6) can be rewritten as

$$\delta V_1 = C_1\beta_0\frac{1-\sigma^2}{\pi E^2 z^3}\sqrt{\frac{2}{\pi}}\left[K_I\cos\frac{\theta}{2} - K_{II}\sin\frac{\theta}{2}\right]$$
$$\times \int d^3 r'\frac{\Delta T^{(0)}(r')}{(x'^2 + y'^2)^{1/4}}, \quad (7)$$

where K_I and K_{II} are the stress intensity coefficients characterizing the behavior of a crack with respect to the normal and tangential stress components, respectively, and θ is the angle between the crack and axis in the direction to the point of observation.

Formulas (6) and (7) represent a three-dimensional generalization of the results obtained previously using a one-dimensional model [13, 14]. According to this theory, the influence of internal stresses on the photoacoustic signal is related entirely to nonlinear thermoelastic properties of the object, rather than with any other special properties. Therefore, the obtained results have a universal character and can be used for the interpretation of experimental data obtained through detection of internal stresses in various materials.

In particular, the obtained expressions indicate that the dependence of the photoacoustic signal on internal stresses is determined by the same quantities as those involved in the stress pattern analysis by measurement of thermal emission (SPATE) [15], although the processes underlying these methods are of different physical natures. These differences are of principal significance from the standpoint of determination of the spatial resolution. Indeed, the spatial resolution of SPATE falls within a millimeter range, whereas photoacoustic imaging is capable of providing the resolution on a micron level. It should be noted that formula (7) can be used, in accordance with the methods developed previously [11, 12], for determining the cracking stress intensity coefficients from the data of photoacoustic measurements taking into account the three-dimensional character of thermal wave generation.

REFERENCES

1. A. Rosencwaig, *Progress in Photothermal and Photoacoustic Science and Technology* (PTR Prentice-Hall, New Jersey, 1994), Vol. 2, pp. 1–23.
2. J. Jumel, D. Rochais, F. Enguehard, and F. Lepoutre, Rev. Sci. Instrum. **74**, 608 (2003).
3. A. L. Glazov and K. L. Muratikov, Zh. Tekh. Fiz. **57**, 2184 (1987) [Sov. Phys. Tech. Phys. **32**, 1320 (1987)].
4. S. K. Likharev and E. I. Rau, Izv. Akad. Nauk SSSR, Ser. Fiz. **54**, 255 (1990).
5. W. Jackson and N. M. Amer, J. Appl. Phys. **51**, 3343 (1980).
6. L. D. Landau and E. M. Lifshitz, *Course of Theoretical Physics*, Vol. 7: *Theory of Elasticity* (Nauka, Moscow, 1987; Pergamon, New York, 1986).
7. A. N. Tikhonov and A. A. Samarskii, *Equations of Mathematical Physics*, 4th ed. (Nauka, Moscow, 1972; Pergamon Press, Oxford, 1964).
8. M. Qian, Chin. J. Acoust. **14**, 97 (1995).
9. K. L. Muratikov and A. L. Glazov, Zh. Tekh. Fiz. **70** (8), 69 (2000) [Tech. Phys. **45**, 1025 (2000)].
10. K. L. Muratikov, A. L. Glazov, D. N. Rose, and J. E. Dumar, J. Appl. Phys. **88**, 2948 (2000).
11. K. L. Muratikov, A. L. Glazov, D. N. Rose, and J. E. Dumar, Pis'ma Zh. Tekh. Fiz. **28** (9), 48 (2002) [Tech. Phys. Lett. **28**, 377 (2002)].
12. K. L. Muratikov, A. L. Glazov, D. N. Rose, and J. E. Dumar, Zh. Tekh. Fiz. **73** (8), 90 (2003) [Tech. Phys. **48**, 1028 (2003)].
13. K. L. Muratikov, Pis'ma Zh. Tekh. Fiz. **24** (13), 82 (1998) [Tech. Phys. Lett. **24**, 536 (1998)].
14. K. L. Muratikov, Zh. Tekh. Fiz. **69** (7), 59 (1999) [Tech. Phys. **44**, 792 (1999)].
15. P. Stanley and J. M. Dulieu-Smith, Exp. Tech. **20**, 21 (1996).

Translated by P. Pozdeev

On the Heat Capacity of Nanocrystalline Substances

S. Sh. Rekhviashvili

Kabardino-Balkarian State University, Nalchik, Kabardino-Balkaria, Russia
e-mail: rsergo@mail.ru
Received May 6, 2004

Abstract—The heat capacity of a nanocrystalline solid possessing a fractal structure is considered within the framework of the Debye model. An expression for the heat capacity is obtained from which the Debye and Dulong–Petit laws follow in particular cases. The heat capacity of nanocrystalline solids may decrease at high temperatures and increase at low temperatures, depending on the fractal dimension of the sample structure. © 2004 MAIK "Nauka/Interperiodica".

In recent years, much attention has been devoted to low-dimensional solid structures in view of the prospects of their use in nanoelectronics and the development of methods such as molecular beam epitaxy and nanoprobe lithography. Recently, Malinovskaya and Sachkov [1] studied the heat capacity of a nanocrystalline solid and pointed out that polycrystalline nanodisperse materials can be expected to possess reduced heat capacity. The calculations in [1] were performed with allowance for the volume and surface contributions to the energy, and it was assumed that atoms both in the bulk and on the surface oscillate at constant frequencies. However, this assumption can be considered as adequate from the standpoint of physics only within a rather narrow frequency interval (in the optical range), which can be hardly acceptable in the case of nanocrystalline substances.

In this study, the heat capacity of solids is calculated using an approach based on the concept of fractal dimension. According to the proposed model, a nanocrystalline substance is modeled by a fractal filled with a phonon gas.

As is known, the fractal dimension is introduced in the problem of covering a geometric set (with balls or cubes) and defined via the relation [2] $z = \xi^{-D}$, where z is the number of cells covering the given set, ξ is the similarity factor (equal to the ratio of dimensions of the cell and the set), and D is the fractal dimensions. Taking into account this definition, the number of phonons can be expressed as

$$z = \frac{C}{\lambda^D} = B\omega^D, \qquad (1)$$

where λ and ω are the phonon wavelength and frequency and C and B are constant quantities dependent on the geometry, structure, and physical properties of samples. According to Eq. (1), the dimension D may vary from one to three. The corresponding spectral density

$$g(\omega) = \frac{dz}{d\omega} = BD\omega^{D-1} \qquad (2)$$

must obey a normalization condition. Since the number of allowed frequencies is equal to the number of degrees of freedom [3], the normalization condition in the case under consideration is as follows:

$$\int_0^{\omega_0} g(\omega)d\omega = DN_A, \qquad (3)$$

where ω_0 is the characteristic frequency (Debye frequency) and N_A is the Avogadro constant. Substituting formula (2) into Eq. (3), we obtain

$$\omega_0 = \left(\frac{DN_A}{B}\right)^{1/D}. \qquad (4)$$

Using relation (4), we exclude constant B from formula (2) and obtain the final expression for the spectral density:

$$g(\omega) = D^2 N_A \frac{\omega^{D-1}}{\omega_0^D}. \qquad (5)$$

Taking into account this equation and the expression for the phonon energy, $E(\omega) = \hbar\omega/[\exp(\hbar\omega/kT) - 1]$, we obtain for the average energy

$$\langle E \rangle = \int_0^{\omega_0} g(\omega)E(\omega)d\omega = \frac{D^2 N_A}{\omega_0^D} \int_0^{\omega_0} \frac{\hbar\omega^D d\omega}{\exp(\hbar\omega/kT) - 1}. \qquad (6)$$
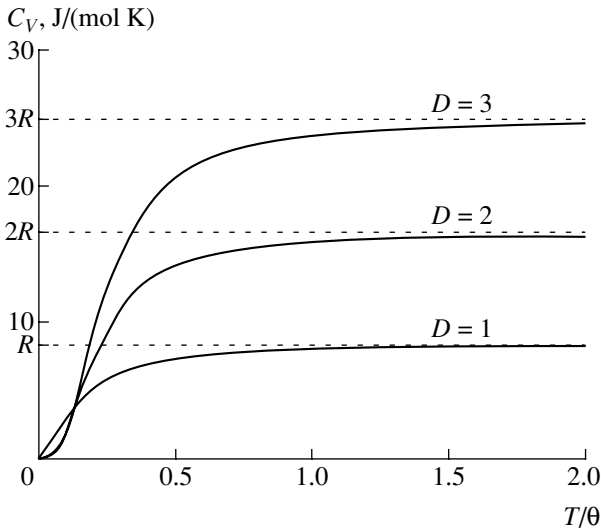
C_V, J/(mol K)

Fig. 1. Plots of the heat capacity versus temperature for the systems with various fractal dimensions.
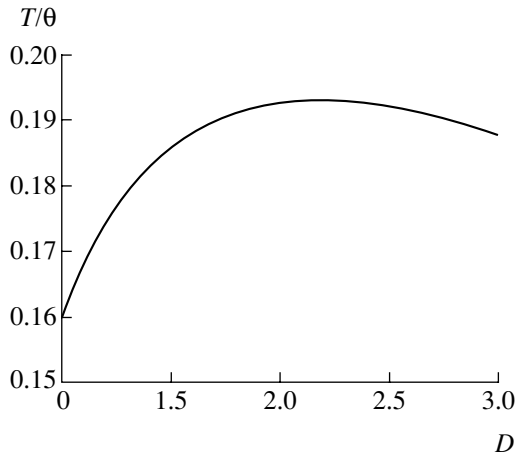

Fig. 2. A plot of the equilibrium temperature versus fractal dimension.

Substituting the variable $x = \hbar\omega/kT$ into expression (6), we obtain

$$\langle E \rangle = D^2 R\theta\left(\frac{T}{\theta}\right)^{D+1} \int_0^{\theta/T} \frac{x^D dx}{\exp(x)-1}, \qquad (7)$$

where $\theta = \hbar\omega_0/k$ is the characteristic temperature and R is the gas constant. The integral in formula (7) cannot be expressed in terms of elementary functions.

At high temperatures ($T \gg \theta$), x is small and $\exp(x) \approx 1 + x$. In this case, Eq. (7) yields the following expression for the heat capacity:

$$C_V = DR. \qquad (8)$$

Formula (8) is an analog of the Dulong–Petit law for fractals. At low temperatures ($T \ll \theta$), the upper integration limit in formula (7) can be replaced by infinity and the heat capacity is expressed as

$$C_V = D^2(D+1)\Gamma(D+1)\zeta(D+1)R\left(\frac{T}{\theta}\right)^D, \qquad (9)$$

where $\Gamma(D+1)$ is the Euler gamma function and $\zeta(D+1)$ is the Riemann zeta function. Formula (9) is an analog of the Debye law for fractals.

In the general case, Eq. (7) yields the following expression for the heat capacity:

$$C_V = D^2 R\left(\frac{T}{\theta}\right)^D \int_0^{\theta/T} \frac{x^{D+1}\exp(x)dx}{(\exp(x)-1)^2}. \qquad (10)$$

As can be readily seen, Eqs. (7)–(10) for $D = 3$ lead to the classical relations of the Debye model [3]. Figure 1 shows the temperature dependences of heat capacity calculated for various D. As expected, in a broad temperature range, reduction in the system dimension is accompanied by a decrease in the heat capacity. However, at low temperatures ($T < 0, 1\theta$), reduction in the system dimension may lead to an increase in the heat capacity. In order to confirm this conclusion, it is necessary to perform thorough experimental investigations of the heat capacity as a function of the fractal dimension and temperature.

A change in the crystal structure of a substance is a second-order phase transition that may influence the heat capacity. According to the general phenomenological theory, such a transition leads to the appearance of a certain ordered state characterized by a special parameter, which is equal to zero in the state of complete disorder and acquires only positive values upon ordering [4]. In our case, the ordering is associated with the concept of fractals and the aforementioned special parameter is the fractal dimension D. It is possible to show that the equation

$$\frac{d\langle E \rangle}{dD} = 0, \qquad (11)$$

which is the condition of equilibrium of a given structure, has a nontrivial solution. Indeed, calculating derivative of the energy (7) with respect to D, we obtain

$$\int_0^{1/y} \frac{x^D \ln(yx\exp(2/D))}{\exp(x)-1}dx = 0, \qquad (12)$$

where $y = T/\theta$. As can be readily seen from Eq. (12), the integrand may acquire (depending on the relation between y and D) both positive and negative values,

which is evidence of the existence of a solution. The solution of Eq. (12) is a positive function $y(D)$. Figure 2 shows this function calculated with sufficiently high precision by numerical methods. A remarkable feature of this function is the characteristic extremum reached at a fractal dimension D between two and three.

REFERENCES

1. T. D. Malinovskaya and V. I. Sachkov, Izv. Vyssh. Uchebn. Zaved. Fiz., No. 12, 84 (2003).

2. R. M. Crownover, *Introduction to Fractals and Chaos* (Jones and Bartlett, London, 1995; Postmarket, Moscow, 2000).

3. N. B. Brandt and S. M. Chudinov, *Electrons and Phonons in Metals* (Mosk. Gos. Univ., Moscow, 1990) [in Russian].

4. L. D. Landau and E. M. Lifshitz, *Course of Theoretical Physics*, Vol. 5: *Statistical Physics* (Nauka, Moscow, 1976; Pergamon, Oxford, 1980).

Translated by P. Pozdeev

Donor Center Formation in Silicon Implanted with Hydrogen Ions

Yu. M. Pokotilo, A. N. Petukh, and V. V. Litvinov

Belarussian State University, Minsk, Belarus
e-mail: pokotilo@bsu.by
Received June 4, 2004

Abstract—We have studied the electrical properties of Schottky diodes based on epitaxial *n*-Si films irradiated by low-energy (300 keV) hydrogen ions. The implantation of protons at room temperature leads to the formation of shallow donors whose concentration–depth profile coincides with that of the incorporated hydrogen. These donor centers are stable on heating up to 150°C and are completely annealed at a temperature of about 250°C. Heating above 270°C leads to the formation of well-known donor centers with a concentration more than two times that of the centers of the first type. Donors of the second type are annealed in two stages at 375−425 and 450–525°C. The nature of the donor centers of both types is related to the formation and transformation of two-dimensional hydrogen-containing defects in a radiation-damaged crystal. © *2004 MAIK "Nauka/Interperiodica".*

As is known [1–3], proton irradiation of silicon to a total dose of 10^{16}–10^{17} cm^{-2} followed by a short-term (~20 min) annealing at 350–550°C leads to formation of hydrogen-containing donor centers of two types, including deep double (HDD) and shallow (SHD) donors. The relative content of HDD and SHD centers depend on the irradiation dose and annealing temperature [4]. The formation of these donor centers is accompanied by annealing of the radiation-induced defects [5, 6]. However, the results of the investigations performed so far did not elucidate the nature of hydrogen-containing shallow donors.

This Letter presents new data on the formation of hydrogen-containing donors in epitaxial silicon films irradiated by low-energy hydrogen ions.

The experiments were performed with Schottky diodes based on epitaxial *n*-Si films with $\rho \approx 1.2$ Ω cm. The thickness of a phosphorus-doped epitaxial layer was about 5 μm. The surface of the silicon layer was coated with vacuum-deposited films of molybdenum and silver (ohmic contact). Then, the samples were irradiated at room temperature by 300-keV H$^+$ ions to a total dose of 10^{15} cm^{-2}. The irradiation was performed through the Ag–Mo contact layer at an ion beam intensity of 3×10^{12} cm^{-1} s^{-1}, which completely excluded heating of the targets during ion bombardment. Finally, the hydrogen-implanted samples were annealed in air in a quartz tube. The electron density distribution in the diode base was studied by the conventional *C–V* technique at a frequency of 1.2 MHz.

Figure 1 presents the typical electron density distributions (*N*) in the base of a Mo–Si Schottky diode in the initial state, after ion irradiation, and in various stages of isochronous (20 min) annealing. The solid curve in

Fig. 1 shows the calculated concentration–depth profile (N_H) of incorporated hydrogen ions simulated using the TRIM program package [7]. As can be seen, the electron density immediately after irradiation (curve *2*) increases by ~1×10^{16} cm^{-3}. This increase takes place in a thin layer of the diode base coinciding with the region of localization of implanted hydrogen (curve *6*) and is related to the formation of hydrogen-containing donors of a new type.
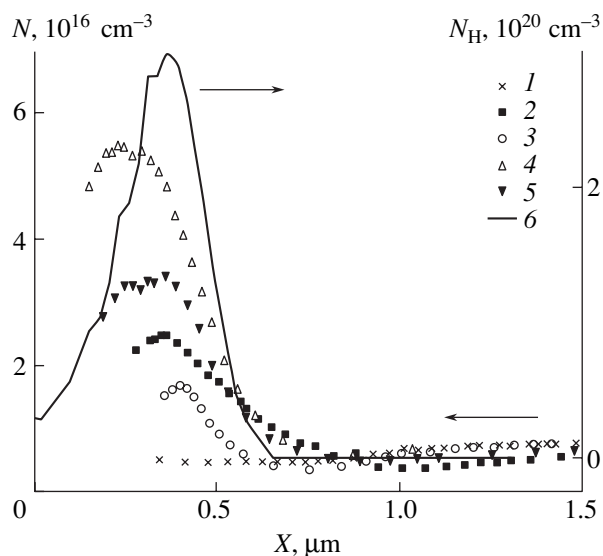

Fig. 1. Electron density (*N*) profiles in the base of a Mo–Si Schottky diode (*1*) in the initial state, (*2*) after ion irradiation, and (*3–5*) in various stages of isochronous (20 min) annealing at *T* = 175 (*3*), 350 (*4*), and 450°C (*5*). Curve *6* shows the calculated concentration–depth profile (N_H) of incorporated hydrogen ions [7].

As is known, the implantation of hydrogen into silicon leads to the formation of a large number of compensating radiation-induced defects [8]. These are deep defects characterized by ionization energies above 0.1 eV, which lead to compensation of the material. In our case, the observed defects are shallow donors with ionization energy below 0.1 eV, which are formed without heat treatment in the base region free of radiation-induced defects. Indeed, the mean projected range of hydrogen ions from the surface of the multilayer (Ag–Mo–Si) target, according to our calculations, is $R_p = 1.65$ μm, and R_p is greater by $(0.3–0.4)R_p$ than the average depth of formation of the radiation-induced defects [9]. This fact was experimentally confirmed in [10]. Therefore, the radiation damage in the region of the maximum of the implanted hydrogen profile (Fig. 1) has to be small. The results of the deep-level transient spectroscopy measurements showed that the concentration of radiation-induced acceptors (~7 × 10^{14} cm^{-3}) is comparable with that observed in the samples annealed at 350–550°C [4].

Figure 2 shows the results of measurements performed in the course of isochronous annealing of an ion-irradiated sample. As can be seen, the observed donors are annealed at 250°C. Subsequent increase in the temperature is accompanied by the formation of the well-known centers of the HDD and SHD types [3]. The maximum concentration of these centers is observed after heat treatment at 350–550°C. HDD centers are annealed within the temperature interval 375–475°C, while the reconstructed SHD centers are annealed at $T > 475$°C [4]. Our results also confirm the reversible character of variation of the SHD concentration in samples quenched from 90–300°C in water.

In conclusion, we have observed shallow hydrogen-containing donors formed without heat-treatment in the epitaxial silicon layers implanted with low-energy hydrogen ions. These donors are annealed at $T = 100–250$°C, and the subsequent increase in the annealing temperature leads to the formation of the well-known donor centers of the HDD and SHD types. The formation and annealing of the hydrogen-containing donors of all three types, as well as the reconstruction of SHD centers during cyclic temperature variations, take place in the same base region coinciding with the maximum of the implanted ion concentration–depth profile. Long-term (~10 h) heat treatments of the samples at temperatures up to 500°C did not produce any significant smearing of the profiles of hydrogen-containing donors. Therefore, the mechanism of formation and reconstruction of the observed hydrogen-containing donors cannot be determined by hydrogen impurity diffusion and is most likely related to the formation
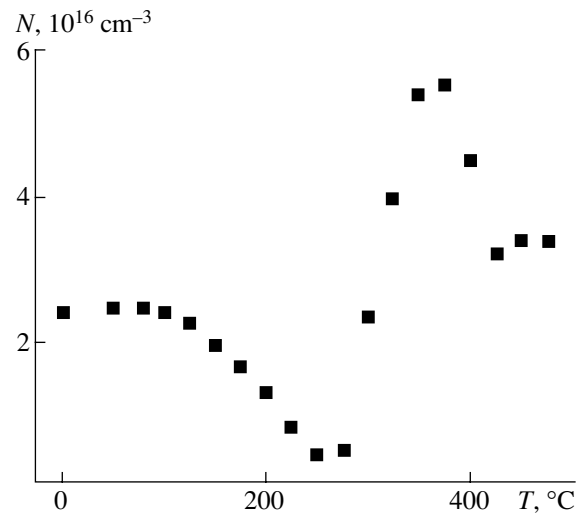

Fig. 2. A plot of the electron density N in the base of ion-irradiated Schottky diodes versus the temperature of isochronous (20 min) annealing.

and transformation of low-mobility two-dimensional hydrogen-containing structures [11, 12].

REFERENCES

1. Y. Ohmura, Y. Zohta, and M. Kanazawa, Phys. Status Solidi A **15**, 93 (1973).
2. S. J. Pearton, J. W. Corbett, and M. Stavola, *Hydrogen in Crystalline Semiconductors* (Springer-Verlag, Berlin, 1992).
3. B. N. Mukashev, Kh. A. Abdulin, and Yu. V. Gorelkinskiĭ, Usp. Fiz. Nauk **170**, 143 (2000) [Phys. Usp. **43**, 139 (2000)].
4. B. N. Mukashev, M. F. Tamendarov, S. Zn. Tokmoldin, *et al.*, Phys. Status Solidi A **91**, 509 (1985).
5. Yu. V. Gorelkinskii, V. O. Sigle, and Zh. S. Takibaev, Phys. Status Solidi A **22**, 55 (1974).
6. B. N. Mukashev, K. N. Nussupov, and M. F. Tamendarov, Phys. Status Solidi B **96**, 17 (1979).
7. J. R. Biersack and L. G. Haggmark, Nucl. Instrum. Methods **174**, 257 (1980).
8. V. A. Kozlov and V. V. Kozlovskiĭ, Fiz. Tekh. Poluprovodn. (St. Petersburg) **35**, 769 (2001) [Semiconductors **35**, 735 (2001)].
9. F. F. Komarov and A. F. Komarov, *Physics of Ion Implantation in Solids* (Tekhnoprint, Minsk, 2001) [in Russian].
10. H. Kauppinen, C. Corbel, K. Skog, *et al.*, Phys. Rev. B **55**, 9598 (1997).
11. N. H. Nickel, G. B. Anderson, N. M. Jonson, *et al.*, Physica B **273–274**, 212 (1999).
12. S. Zh. Tokmoldin, B. N. Mukashev, Kh. A. Abdullin, *et al.*, Physica B **273–274**, 204 (1999).

Translated by P. Pozdeev

The Mechanism of Radiative Recombination in the Region of Interband Transitions in Single Crystal Silicon

A. M. Emel'yanov

Ioffe Physicotechnical Institute, Russian Academy of Sciences, St. Petersburg, 194021 Russia
e-mail: Emelyanov@mail.ioffe.ru
Received May 19, 2004

Abstract—Bimolecular description of the mechanism of radiative recombination in the region of interband transitions fails to explain the linear dependence of the electroluminescence (EL) intensity on the current in single crystal silicon at 300 K for a high level of injection and the exponential decay of emission after switching off the current. The results of experiments can be adequately interpreted within the framework of an exciton mechanism of the radiative recombination in silicon. © 2004 MAIK "Nauka/Interperiodica".

In recent years, there has been a considerable growth in the number of papers devoted to radiative recombination in the region of interband transitions in single crystal silicon (c-Si). This interest is related to the fact that the quantum efficiency reached for the interband transitions in this material [1–3] became practically comparable with that in direct-band semiconductors. Recently [4], it was shown that interpretation of the linear dependence of the electroluminescence (EL) intensity on the forward current through the *p–n* junction [4, 5] in single crystal silicon at ~300−500 K for a high level of injection requires revision of some commonly accepted physical notions concerning the recombination of charge carriers in c-Si.

The existing theory of radiative recombination in c-Si, which was developed by van Roosbroeck and Shockley [6], is based on the so-called bimolecular mechanism, according to which the rate (*R*) of radiative recombination per unit volume in the absence of degeneracy is proportional to the densities of holes (*p*) and electrons (*n*):

$$R = \beta np, \tag{1}$$

where β is the proportionality factor independent of *n* and *p*. Such a bimolecular description of the radiative recombination process was recently used, for example, in [7–9]. However, as was demonstrated in [4], the linear dependence of the interband EL intensity on the current in c-Si under conditions of a high level of injection (whereby the density of major carriers is significantly greater than the dopant concentration and, by virtue of quasineutrality, $n \cong p$) can be explained on the basis of relation (1) only provided that the lifetime of minority carriers (τ_p) is inversely proportional to their density. It is known (see, e.g., [10]) that the relation $\tau_p \propto 1/p$ can hold if the recombination proceeds according to the Auger mechanism involving impurity centers. However, such a behavior contradicts (as will be dem-

onstrated below) the results of investigations of the EL decay kinetics in c-Si.

We have experimentally studied the room-temperature EL of c-Si using a commercial silicon diode (D245A) with a donor concentration in the base region below 10^{14} cm^{-3} and a *p–n* junction area of about 20 mm^2. The emission was extracted via a hole made in the diode case. The experimental procedure of measurement of the EL spectrum and kinetics was described in detail elsewhere [4]. A new important feature of this study was that the kinetics was measured under the conditions of practically absent loss of carriers from the diode to the external circuit.

Figure 1 shows the EL spectrum of the silicon diode studied. The vertical lines in Fig. 1 indicate the energies of quanta corresponding to the onset of EL intensity growth in the long-wavelength part of the spectrum for various mechanisms of radiative recombination in c-Si. It can be seen that (at least) a considerable pert of EL intensity is due to recombination via excitons with the participation of phonons. The integral EL intensity *Y* exhibited a linear dependence on the diode current, at least in the range of currents from 0.3 to 1.2 A. In this interval, the conditions of high injection level were satisfied as confirmed by estimates of the carrier density obtained using the carrier lifetimes measured by conventional methods [13, 14].

Figure 2 shows the EL decay kinetics for three values of the diode current. The EL decay with the time *t* can be described by the exponent $Y \propto \exp(-t/\tau)$, where τ is a constant quantity. For the recombination of free charge carriers (with neglect of the formation and recombination of excitons in the region of EL decay), we obtain the relation

$$d\left(\int_0^L p\,dx\right)/dt = -\int_0^L p\,dx/\tau_p, \tag{2}$$

where integration is performed over a semiconductor layer with the thickness L in which the recombination takes place [4]. In the case of $\tau_p \propto 1/p$ and exponential decay of the EL intensity, Eqs. (1) and (2) lead to the relation $\int_0^L p^2\, dx \propto \int_0^L p\, dx$. This relation can be valid only for $p = \text{const}$, which contradicts the experimental data. Therefore, the exponential EL kinetics cannot be explained for $\tau_p \propto 1/p$. The same result is obtained when Eq. (2) takes into account a partial recombination via excitons.

It was shown [4] that the linear dependence of the interband EL intensity on the current, as well as the EL kinetics observed for a high level of injection, can be explained assuming that $\beta \propto 1/p$. However, within the framework of the notions about bimolecular recombination of free charge carriers, it is impossible to select the physical mechanisms and laws ensuring that $\beta \propto 1/p$.

An adequate explanation of the observed behavior can be provided by assuming that virtually all radiative recombination in the region of interband transitions in c-Si proceeds via excitons not only at low temperatures (as is usually assumed), where the exciton character of the spectrum is consistent with the linear dependence of the EL intensity on the excitation level and with the exponential decay [15], but at room temperature and at higher temperatures as well. In this case, the recombination kinetics in the region where the EL intensity is a linear function of the current is describe by the equation

$$d\!\left(\int_0^L p\,dx\right)\!/dt + d\!\left(\int_0^l w\,dx\right)\!/dt$$
$$= j/q - \int_0^L p\,dx/\tau_p - \int_0^L w\,dx/\tau_w. \tag{3}$$

Here, w and τ_w are the exciton concentration and lifetime, respectively; j is the current density; and q is the elementary charge. The rate of radiative recombination via excitons per unit volume is

$$R_w = w/\tau_r, \tag{4}$$

where τ_r is the radiative lifetime of excitons. Assuming that τ_r and τ_w are independent of w, we obtain under equilibrium conditions (whereby the left-hand side of Eq. (3) is zero) a relation,

$$Y \propto \left(\int_0^L w\,dx\right)\!/\tau_r = \left(i/q - \int_0^L p\,dx/\tau_p\right)\!\tau_w/\tau_r, \tag{5}$$

from which it follows that $Y \propto j$ for $\int_0^L p\,dx/\tau_p \propto j$. This dependence is experimentally confirmed for $\tau_p = \text{const}(p)$ [10]. It can be shown that the exciton mechanism does not contradict the exponential EL decay
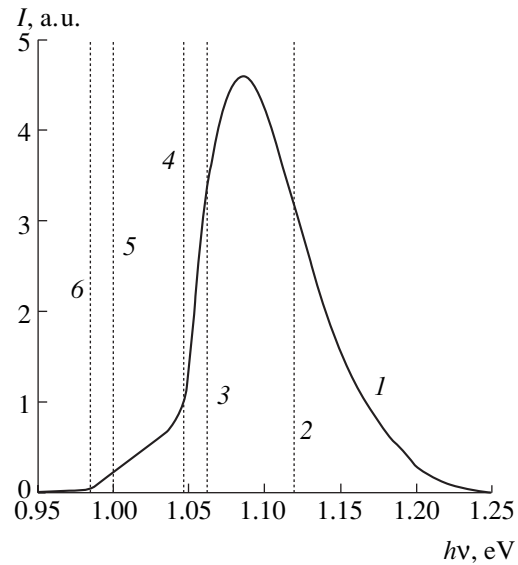

Fig. 1. The EL spectrum of the silicon diode measured for a current of 0.4 A (curve *1*). The vertical dashed lines indicate the energies of quanta corresponding to (*2*) the bandgap width in c-Si ($E_g = 1.12$ eV), (*3*) E_g minus the energy spent for recombination of the TO phonon ($E_{pt} \cong 58$ meV) accounting for the main EL peak [8], (*4*) E_g minus E_{pt} and minus the exciton binding energy $E_{ex} \cong 15$ meV [11], (*5*) E_g minus the maximum energy of the optical phonon in c-Si ($E_{pt} \cong 120$ meV) [12], and (*6*) E_g minus $E_{pt} \cong 120$ meV and minus E_{ex}.
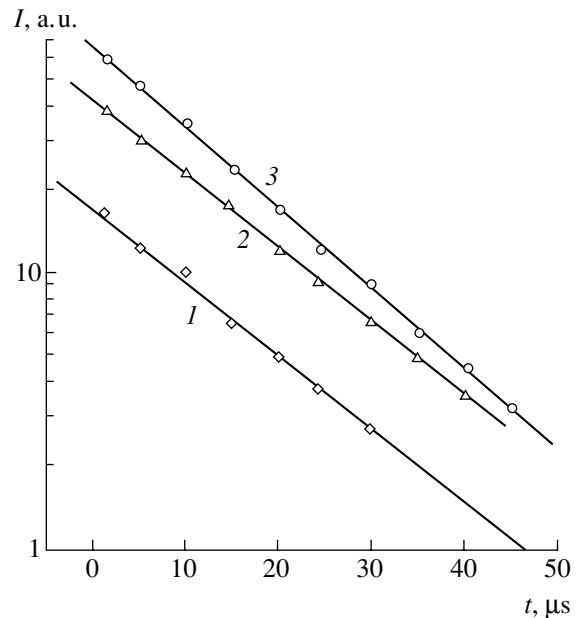

Fig. 2. EL decay kinetics measured in a silicon diode for three values of the forward current (A): (*1*) 0.4; (*2*) 0.8; (*3*) 1.2.

kinetics. Moreover, it was demonstrated that the shape of the EL spectrum can also be described within the framework of the notions about recombination via excitons [16].

The presence of a considerable contribution of exciton radiation (estimated at ~50% at 300 K) to the spectrum of interband (edge) EL in c-Si was recently reported in [17, 18]. However, for this (partial) contribution, it is impossible to explain all experimental results—in particular, the absence of bending points at the intersections of curve *1* (Fig. 1) with lines *3* and *5*. The concentration of excitons was estimated, under assumption of thermodynamic equilibrium, from theoretical stipulations of [11]. For currents within the range 0.3–1.2 A, the estimates amount to several percent of the density of holes injected into the diode base. Therefore, the above model notions require that τ_r be smaller by more than two orders of magnitude than the radiative lifetime of free charge carriers (τ_f). Such a considerable difference between τ_r and τ_f may be related to the fact that the average distance between free carriers in the experiments was more than five times the Bohr radius of the exciton ($r_B = 4.2$ nm [19]). In addition, radiative recombination in c-Si requires a certain correlation in the mutual arrangement of electron, hole, and phonon, which is most probably realized in the case of recombination via excitons. According to estimates available in the literature (see, e.g., [19, 20]), τ_r falls in the range from 10^{-6} to 10^{-3} s. For some τ_r from this interval, the EL intensities observed in experiment coincide with the values determined using formula (4) despite the fact that the exciton concentrations w are much smaller than the values predicted by the theory [11].

REFERENCES

1. M. A. Green, J. Zhao, A. Wang, *et al.*, Nature **412**, 805 (2001).

2. Wai Lek Ng, M. A. Lourenco, R. M. Gwilliam, *et al.*, Nature **410**, 192 (2001).

3. Th. Trupke, J. Zhao, A. Wang, *et al.*, Appl. Phys. Lett. **82**, 2996 (2003).

4. A. M. Emel'yanov, N. A. Sobolev, and E. I. Shek, Fiz. Tverd. Tela (St. Petersburg) **46**, 44 (2004) [Phys. Solid State **46**, 40 (2004)].

5. N. A. Sobolev, A. M. Emel'yanov, E. I. Shek, and V. I. Vdovin, Fiz. Tverd. Tela (St. Petersburg) **46**, 39 (2004) [Phys. Solid State **46**, 35 (2004)].

6. W. van Roosbroeck and W. Shockley, Phys. Rev. **94**, 1558 (1954).

7. Th. Dittrich, V. Yu. Timoshenko, J. Rappich, *et al.*, J. Appl. Phys. **90**, 2310 (2001).

8. P. D. Altukhov and E. G. Kuzminov, Solid State Commun. **111**, 379 (1999).

9. T. Trupke, M. A. Green, P. Würfel, *et al.*, J. Appl. Phys. **94**, 4930 (2003).

10. L. M. Blinov, E. A. Bobrova, V. S. Vavilov, *et al.*, Fiz. Tverd. Tela (Leningrad) **9**, 3221 (1967) [Sov. Phys. Solid State **9**, 2537 (1967)].

11. D. E. Kane and R. M. Swanson, J. Appl. Phys. **73**, 1193 (1993).

12. R. A. Smith, *Semiconductors* (Cambridge University Press, Cambridge, 1959; Mir, Moscow, 1982).

13. B. Lax and T. Neustadter, J. Appl. Phys. **25**, 1148 (1954).

14. M. S. Tyagi and R. van Overstraeten, Solid-State Electron. **26**, 577 (1983).

15. V. S. Vavilov and É. L. Nolle, in *Excitons in Semiconductors* (Nauka, Moscow, 1971).

16. J. R. Haynes, M. Lax, and W. F. Flood, J. Phys. Chem. Solids **8**, 392 (1959).

17. M. S. Bresler, O. B. Gusev, B. P. Zakharchenya, and I. N. Yassievich, Fiz. Tverd. Tela (St. Petersburg) **46**, 10 (2004) [Phys. Solid State **46**, 5 (2004)].

18. M. S. Bresler, O. B. Gusev, E. I. Terukov, *et al.*, Fiz. Tverd. Tela (St. Petersburg) **46**, 18 (2004) [Phys. Solid State **46**, 13 (2004)].

19. A. V. Sachenko and Yu. V. Kruchenko, Semicond. Phys. Quantum Electron. Optoelectron. **3**, 150 (2000).

20. L. V. Keldysh, in *Excitons in Semiconductors* (Nauka, Moscow, 1971).

Translated by P. Pozdeev

Synthesis and Characterization
of *n*-ZnO:Al/CoPc/*p*-Si Structures

G. A. Il'chuk, S. E. Nikitin, Yu. A. Nikolaev,
V. Yu. Rud', Yu. V. Rud', and E. I. Terukov

Ioffe Physicotechnical Institute, Russian Academy of Sciences, St. Petersburg, 194021 Russia
"Lvivska Politekhnika" National University, 79013 Lviv, Ukraine
St. Petersburg State Technical University, St. Petersburg, 195251 Russia
Received June 1, 2004

Abstract—Photosensitive structures of the *n*-ZnO:Al/CoPc/*p*-Si type were synthesized for the first time using vacuum sublimation of cobalt phthalocyanine (CoPc) and magnetron sputtering of a ZnO:Al target. The maximum photoresponse is observed when the structure is illuminated from the side of the ZnO layer and amounts to $\cong 400$ V/W at $T = 300$ K. Mechanisms of current transfer and peculiarities of the photosensitivity spectrum are considered. It is suggested that the new photosensitive structures can be used in multiband photoconverters of natural radiation with a broad working spectral range. © *2004 MAIK "Nauka/Interperiodica".*

An important direction in the development of modern electronics is related to the synthesis of new organic and inorganic semiconductors and their implementation for the creation of a new generation of device structures [1–3]. Recently [4], we demonstrated the possibility of obtaining photosensitive structures based on the contact of an organic semiconductor with crystalline silicon. The organic component in these structures was copper phthalocyanine (CuPc), representing a broad class of organic semiconductors. The molecules of phthalocyanines of various metals possess a centrosymmetric planar structure [5, 6]. Since all interatomic bonds in the large Pc ring have the same length $(1.34 \pm 0.03$ Å$)$, such a molecule represents a resonance hybrid. This is confirmed by the presence of diamagnetic anisotropy and by the discrete spectrum of optical absorption [5].

Thus study continues our previous investigation [4] and is devoted to the photoelectric properties of the first structures based on cobalt phthalocyanine (CoPc). It can be expected that a change in the type of metal entering into the phthalocyanine structure may provide a means of effective control of the parameters of a new class of photosensitive materials.

Synthesis. The samples of new photosensitive structures were obtained on single crystal *p*-Si substrates representing commercial KDB-0.03 wafers with a chemically polished (111) surface. Thin layers (with a thickness of $d \cong 1$ μm) of cobalt phthalocyanine (an organic semiconductor) were deposited onto the *p*-Si(111) surface by thermal vacuum sublimation of a preliminarily synthesized CoPc powder. The CoPc films grown on the *p*-Si(111) surface had a mirror surface and were characterized by a strong adhesion to the surface of crystalline silicon. Then, the surface of the

CoPc layer was covered by a strongly doped *n*-ZnO:Al film with the density of free electrons $n \cong 10^{20}$ cm^{-3} $(T = 300$ K$)$. This film was formed by magnetron sputtering of a stoichiometric target made of ZnO with ~2.5 wt % Al additive. The *n*-ZnO:Al films were deposited during ~4 h in argon at a pressure of $\cong 0.5$ Pa and a substrate temperature not exceeding 50°C.

Electrical measurements. The results of measurements of the stationary current–voltage (*I*–*V*) characteristics of the first synthesized *n*-ZnO:Al/CoPc/*p*-Si structures showed that the samples exhibit a clear rectification effect. Figures 1a–1c show the typical *I*–*V* curves for one of the sample structures. The forward current direction corresponds to a bias voltage applied with minus on the *n*-ZnO:Al side. In the best samples, the dark current in the forward direction exceeded the reverse current by a factor of ~8×10^3 at $T = 300$ K.

In the forward branch of the *I*–*V* curve of the *n*-ZnO:Al/CoPc/*p*-Si structures for applied bias voltages of $U \leq 0.8$ V, the initial region obeys the well-known equation established for the structures with inorganic semiconductors [7],

$$I = I_0[\exp(eU/nkT) - 1], \qquad (1)$$

where the saturation current at $T = 300$ K is $I_0 \cong 10^{-9}$ A and the diode coefficient is within $n \cong 6.5$–7.1. The latter value suggests that the current transfer in the forward direction in *n*-ZnO:Al/CoPc/*p*-Si structures, as well as in the analogous CuPc-based structures [4], proceeds according to a tunneling-recombination mechanism.

According to Fig. 1a, the forward current in the *n*-ZnO:Al/CoPc/*p*-Si structure biased to $U > 5$ V is a
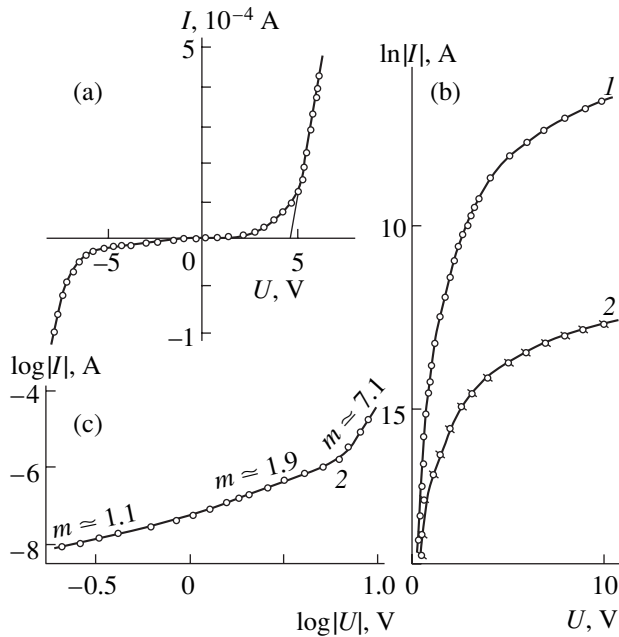
Fig. 1. Typical stationary current–voltage characteristic of an *n*-ZnO:Al/CoPc/*p*-Si structure at *T* = 300 K plotted in (a) usual, (b) semilogarithmic, and (c) logarithmic scale: (*1*) forward branch; (*2*) reverse branch.
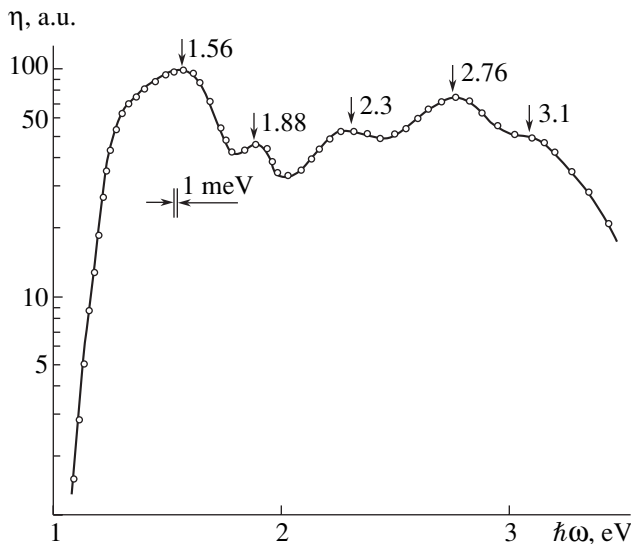

Fig. 2. The typical spectral dependence of the relative quantum efficiency of photoconversion in the *n*-ZnO:Al/CoPc/*p*-Si structure illuminated by nonpolarized radiation from the side of the *n*-ZnO:Al film (*T* = 300 K). Arrows indicate the energy positions of peaks in the $\eta(\hbar\omega)$ spectrum measured at *T* = 300 K.

linear function of the applied voltage,

$$I = \frac{U - U_0}{R_0}, \tag{2}$$

where the cutoff voltage is $U_0 \cong 4.5$ V and the residual resistance is $R_0 \cong 2 \times 10^4$ Ω at *T* = 300 K.

The reverse current in the *n*-ZnO:Al/CoPc/*p*-Si structures studied usually obeyed the power law $I \sim U^m$, where the exponent *m* increased with the voltage (Figs. 1a and 1c). In the interval of negative bias voltages below 1 V, this exponent is close to unity, which corresponds to the regime of tunneling or a current limited by the space charge in the regime of velocity saturation [8]. In the interval of negative voltages $U \cong$ 1–6 V, the exponent increases to $m \cong 2$, which may be evidence of a current limited by the space charge in the regime of mobility saturation [8]. A sharp growth in the reverse current observed for $U > 7$ V and the corresponding increase in the exponent up to $m \cong 7$ (Figs. 1a and 1c) are indicative of a "soft" breakdown.

Photoelectric measurements. Illumination of the *n*-ZnO:Al/CoPc/*p*-Si structures gives rise to a photovoltaic effect with a sign corresponding in all cases to minus on the exposed (frontal) *n*-ZnO:Al film side. The photovoltaic effect was always dominating in the case of structures illuminated from this side, and the indicated sign remained unchanged when a probing light beam (with a diameter of ≈0.5 mm) scanned over the sample surface and when the photon energy and/or the incident light intensity was varied. It should be also noted that the sign of photo emf corresponded to the direction of rectification in the same structure. The maximum photoresponse in the best structures illuminated from the ZnO side amounted to ≈400 V/W.

Figure 2 shows the typical spectral dependence $\eta(\hbar\omega)$ of the relative quantum efficiency of photoconversion in the *n*-ZnO:Al/CoPc/*p*-Si structure illuminated by nonpolarized radiation from the side of the wide-bandgap component (*n*-ZnO:Al). As can be seen, the structures based on CoPc, as well as the *n*-ZnO:Al/CuPc/*p*-Si structures studied in [4], are characterized by high photosensitivity in a broad range of incident photon energies bounded by the gap widths of the narrow- and wide-bandgap components. Indeed, the long-wavelength growth of photosensitivity in the *n*-ZnO:Al/CoPc/*p*-Si structures is observed at $\hbar\omega >$ 1 eV, in agreement with the onset of interband optical transitions in the *p*-Si substrate of these structures. The long-wavelength edge of the $\eta(\hbar\omega)$ spectrum is well described by a law characteristic of indirect interband transitions [7],

$$\eta = \frac{A}{\hbar\omega}(\hbar\omega - E_G^{in})^2, \tag{3}$$

where *A* is a constant factor and E_G^{in} is the width of the semiconductor bandgap; extrapolation $(\eta\hbar\omega)^{1/2} \longrightarrow 0$ gives E_G^{in} corresponding to that of crystalline silicon [9]. Therefore, both the energy position and the character of the $\eta(\hbar\omega)$ spectrum at the long-wavelength edge suggest that this edge is related to the photoabsorption in the crystalline silicon substrate.

The onset of the short-wavelength decay in photosensitivity of the *n*-ZnO:Al/CoPc/*p*-Si structures at

$\hbar\omega \geq 3.1$ eV (Fig. 2) satisfactorily agrees with the bandgap width of ZnO [9]. For this reason, the short-wavelength boundary of photosensitivity can be related to the onset of direct interband transitions in ZnO films. As a result, an increase in the optical absorption coefficient is accompanied by a decrease in the depth of absorption in the ZnO film and by the elimination of the corresponding layer of photogenerated charge carriers from the active region of the structure studied.

Therefore, the *n*-ZnO:Al/CoPc/*p*-Si structures exhibit maximum photosensitivity in the energy interval between bandgap widths of the component semiconductors (Si and ZnO), In this respect, the synthesized *n*-ZnO:Al/CoPc/*p*-Si structures are similar to the well-known heterojunctions, including the layers of inorganic diamondlike semiconductors [7, 10]. However, in contrast to these heterojunctions, the new structures are characterized by the appearance of several photoresponse peaks with well-reproduced positions ($\hbar\omega_1^m \cong 1.56$ eV; $\hbar\omega_2^m \cong 1.88$ eV; $\hbar\omega_3^m \cong 2.3$ eV; and $\hbar\omega_4^m \cong 2.76$ eV). We may suggest that these peaks reflect the discrete character of the optical absorption spectra of phthalocyanines, which is related to their specific structural features and determined by the type of the metal atom [5]. This probably accounts for the differences between the spectra of photosensitivity of the *n*-ZnO:Al/CoPc/*p*-Si and *n*-ZnO:Al/CuPc/*p*-Si [4] structures observed in the interval between the bandgap widths of Si and ZnO. Indeed, these structures differ only by the types of metal atoms entering into the molecule of the organic semiconductor. Therefore, similar to the case of heterojunctions based on diamondlike semiconductors [1, 10], by changing the type of metal atoms in the structure, it is possible to control the spectral features of $\eta(\hbar\omega)$ in the interval between the bandgap widths of semiconductor components. Using this approach, it is possible to create multiband photoconverters.

In conclusion, we have synthesized for the first time photosensitive structures of the *n*-ZnO:Al/CoPc/*p*-Si type based on heterojunctions between a thin layer of cobalt phthalocyanine (organic semiconductor) and diamondlike semiconductors (Si, ZnO). The obtained structures were characterized with respect to rectification properties and the photovoltaic effect. The new structures have good prospects for use in semiconductor electronics.

REFERENCES

1. Zh. I. Alferov, Fiz. Tekh. Poluprovodn. (St. Petersburg) **32**, 3 (1998) [Semiconductors **32**, 1 (1998)].

2. P. Peumans and S. P. Forrest, Appl. Phys. Lett. **79**, 126 (2001).

3. P. Peumans, S. Uchida, and S. R. Forrest, Nature **425**, 158 (2003).

4. G. A. Il'chuk, N. V. Klimova, O. I. Kon'kov, *et al.*, Fiz. Tekh. Poluprovodn. (St. Petersburg) **38**, 1056 (2004) [Semiconductors **38**, 1018 (2004)].

5. A. Vartanyan, Zh. Fiz. Khim. **22**, 769 (1948).

6. D. D. Eley, Nature **162**, 819 (1948).

7. S. M. Sze, *Physics of Semiconductor Devices* (Willey, New York, 1981).

8. M. Lampert and P. Mark, *Current Injection in Solids* (Academic Press, New York).

9. *Physicochemical Properties of Semiconductors: A Handbook*, Ed. by A. V. Novoselova (Nauka, Moscow, 1979) [in Russian].

10. B. L. Sharma and R. K. Purohit, *Semiconductor Heterojunctions* (Pergamon, Oxford, 1974).

Translated by P. Pozdeev

The Effect of Internal Electric Field on the High-Temperature Diffusion of Arsenic in Variable-Gap Epitaxial CdHgTe Layers

A. P. Vlasov, L. S. Monastyrskiĭ, B. S. Sokolovskiĭ*, and G. A. Il'chuk

Ivan Franko Lviv National University, Lviv, Ukraine
"Lvivska Politekhnika" National University, 79013 Lviv, Ukraine
* e-mail: sokol@franko.lviv.ua
Received July 8, 2004

Abstract—We have studied peculiarities of the high-temperature diffusion of arsenic implanted into variable-gap epitaxial CdHgTe layers. The nonmonotonic shape of the diffusion profiles can be explained by the presence of an inhomogeneous internal electric field related to the variable band structure of the epitaxial layers. © 2004 MAIK "Nauka/Interperiodica".

The spatial inhomogeneity of the band structure inherent in variable-gap semiconductors strongly influences the transport of free charge carriers in these materials, thus leading to some physical effects not manifested in energetically homogeneous semiconductors [1]. This inhomogeneity of the band structure, accounting for the existence of internal electric fields in variable-gap semiconductors [2–5], must also significantly influence the diffusion of charged impurities [6]. Despite the obvious importance of this problem, no systematic experimental investigations of the diffusion of impurities in variable-gap semiconductors have been performed so far.

This study was aimed at obtaining direct experimental evidence of the influence of a variable band structure on the diffusion of charged impurities. For this purpose, we studied the diffusion profiles of arsenic in variable-gap epitaxial layers of CdHgTe.

The experiments were performed with an intrinsic defect epitaxial CdHgTe layer of the *n* type grown by the evaporation–condensation–diffusion technique [7] with $(N_d - N_a|_{77\,K} = 2.1 \times 10^{16}$ cm^{-3}, $\mu_{77\,K} = 2.7 \times 10^4$ cm^2/(V s), and the initial relative content of Cd on the surface $x_{Cd} = 0.21$. The source of the impurity was provided by implanting arsenic ions at an energy of 100 keV to a total dose of $\Phi = 1 \times 10^{15}$ cm^{-2}. The variable band structure in the subsurface region of CdHgTe was formed in the course of heat treatment of the initial structure for 10 min at $T = 600$°C in saturated vapors of Hg ($P_{Hg} = 3.3 \times 10^5$ Pa) and Cd. This treatment leads [8, 9] to conversion of the surface composition of the CdHgTe layer (up to the formation of CdTe). The diffusion of the impurity in the variable-gap layer was caused by heat treatment in the same regime ($T = 600$°C, $t = 10$ min).

Figure 1 shows the typical distributions of arsenic in the samples studied by the method of secondary ion mass spectrometry (SIMS) profiling. As can be seen
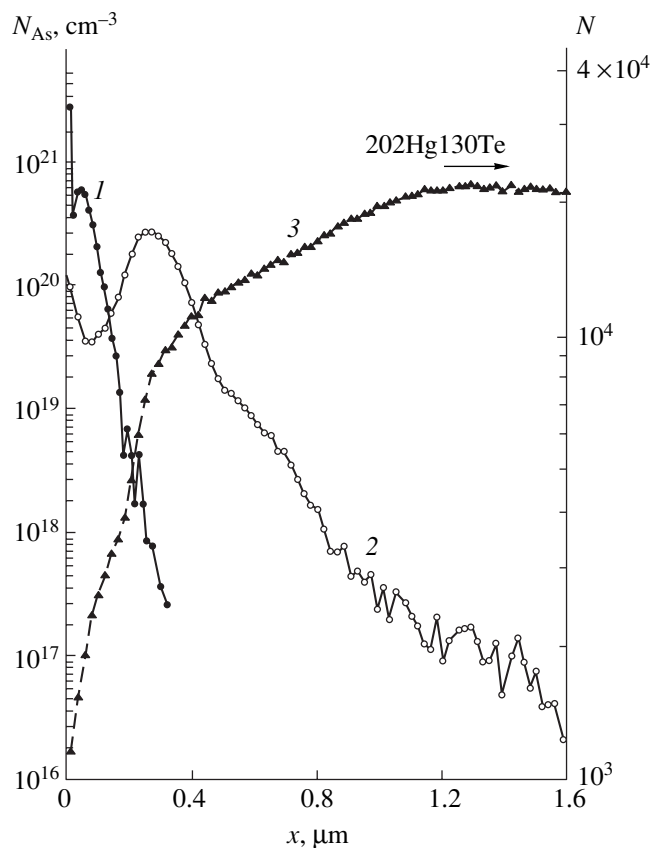

Fig. 1. SIMS profiles of arsenic impurity in a variable-gap epitaxial CdHgTe layer measured (*1*) after ion implantation and (*2*) after diffusion annealing in Hg and Cd vapors ($T = 600$°C, $t = 10$ min). Curve *3* is a plot of the intensity of the 202Hg130Te line versus depth.

from these data, the sample composition in the subsurface region exhibits variations that are most pronounced within a layer with a thickness of about 0.3 μm. The same region features a nonmonotonic profile of the diffusing impurity with a clearly pronounced maximum and minimum. We believe that this behavior of the impurity is explained by the influence of the internal electric field on the diffusion of arsenic. It should be noted that, since the areas under the curves of the initial and final arsenic profiles coincide to within 4%, the back diffusion of arsenic (escape of impurity from the sample) can be ignored.

Using results obtained previously [6], we obtain an expression for the strength of the internal electric field arising in the variable-gap CdHgTe structure due to the spatial inhomogeneity of the bandgap width E_g and the electron affinity χ:

$$E_{gr} = \frac{1}{2e}\frac{dE_g}{dx}\left(\frac{zN}{\sqrt{(zN)^2 + 4n_i^2}} - \frac{1}{3}\right), \qquad (1)$$

where N is the concentration of acceptors, z is the degree of ionization of the acceptor impurity, n_i is the intrinsic carrier density in CdHgTe [10], and e is the absolute value of the electron charge. In writing Eq. (1), we used the following relation, which is valid for the variable-gap layers of CdHgTe [11]:

$$\frac{d\chi}{dx} \cong -\frac{2}{3}\frac{dE_g}{dx}.$$

As can be seen from the inset in Fig. 2, the field strength profile E_{gr} exhibits a sharp variation in the interval $\sim 0.18\ \mu m < x < 0.26\ \mu m$, where E_g reaches a maximum value of ~ 10 kV/cm.

In addition to the electric field related to the variable band structure of the epitaxial CdHgTe layer, there also exists a field caused by an inhomogeneous distribution of the charged impurity. The strength of this field is given by the formula [12]

$$E_{im} = \frac{kT}{e}\frac{1}{\sqrt{(zN)^2 + 4n_i^2}}\frac{\partial N}{\partial x}. \qquad (2)$$

Taking into account the electric field components described by Eqs. (1) and (2), we have numerically solved the equation of electrodiffusion,

$$\frac{\partial N}{\partial t} = \frac{\partial}{\partial x}\left(D\left[\frac{\partial N}{\partial x} + \frac{ez}{kT}(E_{gr} + E_{im})N\right]\right), \qquad (3)$$

where D is the coefficient of diffusion for the impurity at a small concentration in the absence of an electric field. The initial condition for Eq. (3) corresponded to the impurity profile after ion implantation, while the boundary conditions reflected the absence of mass transfer through the epitaxial layer.

Figure 2 shows the results of modeling of the diffusion of arsenic in the variable-gap epitaxial CdHgTe
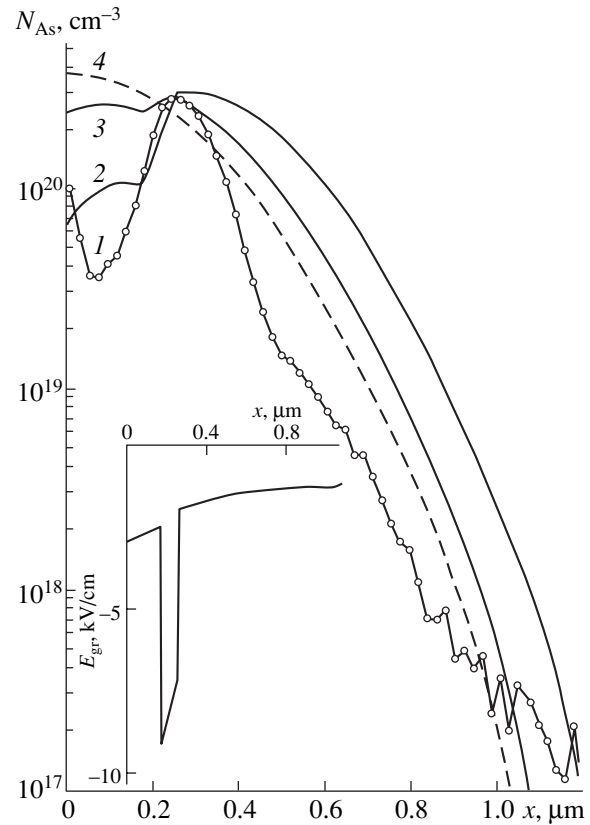

Fig. 2. Arsenic diffusion profiles in a variable-gap epitaxial CdHgTe layer: (*1*) experiment; (*2, 3*) calculation with the parameters $T = 600°C$; $t = 10$ min, $D = 1.4 \times 10^{-13}$ cm^2/s for triply and singly charged ions, respectively; (*4*) calculation in the absence of an internal electric field. The inset shows a profile of the internal electric field strength E_{gr} calculated using the experimental composition profile of the variable-gap epitaxial CdHgTe structure.

layer for $D = 1.4 \times 10^{-13}$ cm^2/s. This value provided the best fit to the experimental profile in the vicinity of the maximum. In the absence of the internal electric field related to the variable band structure, the concentration of the impurity monotonically decreases in depth (curve *4*). Making allowance for the variable-gap field component leads to the appearance of a maximum and minimum on the impurity diffusion profile (curves *2* and *3*). The position of this maximum virtually coincides with the region of sharp decrease in the electric field strength. The reason for the appearance of the maximum on the impurity profile is quite clear, since the drift component of the diffusion flow sharply drops and the impurity is accumulated in the region of minimum field strength.

The profiles of arsenic diffusion presented in Fig. 2 were calculated for the cases of singly (curve *3*) and triply (curve *2*) charged impurity ions [13]. In the latter case (curve *2*), the profile exhibits a deeper minimum and the entire curve in the subsurface region is closer to the experimental profile. In our opinion, this circum-

stance is additional evidence in favor of triply charged arsenic impurity ions in CdHgTe.

Thus, the observed peculiarities in the high-temperature diffusion of arsenic in a variable-gap sample of CdHgTe can be explained by the presence of an inhomogeneous internal electric field. This, in turn, can be considered as experimental confirmation of the model of diffusion of a charged impurity in variable-gap semiconductors [6]. However, it should be noted that coincidence of the experimental results and calculated data has a qualitative rather than quantitative character. For a more strict comparison of the experimental and theoretical diffusion profiles, it is necessary to take into account a number of factors, including the multicomponent character of arsenic diffusion, concentration dependence of the diffusion coefficient, near-surface bending of the energy bands, etc.

REFERENCES

1. Zh. I. Alferov, Usp. Fiz. Nauk **172**, 1072 (2002).
2. H. Kroemer, RCA Rev. **18**, 332 (1957).
3. T. D. Dzhafarov, Phys. Status Solidi A **42**, 11 (1977).
4. T. D. Dzhafarov, *Defects and Diffusion in Epitaxial Structures* (Nauka, Leningrad, 1978) [in Russian].
5. B. S. Sokolovskiǐ, Ukr. Fiz. Zh. **39**, 327 (1994).
6. L. S. Monastyrskiǐ and B. S. Sokolovskiǐ, Fiz. Tekh. Poluprovodn. (Leningrad) **26**, 2143 (1992) [Sov. Phys. Semicond. **26**, 1203 (1992)].
7. V. G. Savitsky and O. P. Storchun, Thin Solid Films **317**, 105 (1998).
8. S. Y. An, J. S. Kim, D. W. Seo, and S. H. Suh, J. Electron. Mater. **31**, 683 (2002).
9. S. B. Lee, D. Kim, and D. A. Stevenson, J. Vac. Sci. Technol. B **9**, 1639 (1991).
10. G. L. Hansen, J. L. Schmit, and T. N. Casselman, J. Appl. Phys. **53**, 7099 (1982).
11. D. Eich, K. Ortner, U. Groh, *et al.*, Phys. Status Solidi A **173**, 261 (1999).
12. F. L. Smith, Proc. IRE **46**, 1049 (1958).
13. A. Vlasov, V. Bogoboyashchyy, O. Bonchyk, and A. Barcz, Cryst. Res. Technol. **39**, 11 (2004).

Translated by P. Pozdeev